EX-DESY-Zeuthen-97-04
sw9741

A full Spin Analysis of the Process
$e^+e^- \rightarrow \tau^+\tau^-$ using the L3 Detector at LEP

Reinhold Völkert

Thesis-1997-Völkert

A full Spin Analysis of the Process $e^+e^- \rightarrow \tau^+\tau^-$ using the L3 Detector at LEP

D i s s e r t a t i o n

zur Erlangung des akademischen Grades

doctor rerum naturalium
(Dr. rer. nat.)

eingereicht an

der Mathematisch-Naturwissenschaftlichen Fakultät I
der Humboldt-Universität zu Berlin

von

Diplom-Physiker Reinhold Völkert,
geboren am 24. September 1966 in Münster

Präsident der Humboldt-Universität zu Berlin
Prof. Dr. H. Meyer

Dekanin der Mathematisch-Naturwissenschaftlichen Fakultät I
Prof. Dr. V. Bonacic-Koutecky

Gutachter: 1.   Prof. Dr. T. Hebbeker
                  2.   Priv. Doz. Dr. M. Pohl
                  3.   Prof. Dr. P. Söding

Tag der mündlichen Prüfung: 26.06.1997

Nur dadurch wird mein Gegenstand nicht alle befriedigen, weil sein Nutzen der Gedankenlosigkeit nicht einleuchtet. [...] Aber bitte, wird man mir sagen, was nützt einem hungrigen Magen die Kenntnis der Natur, was die ganze Astronomie? Nun, die verständigen Menschen hören nicht auf die Unbildung, die da schreit, man müsse deswegen jene Studien unterlassen. Man duldet die Maler, weil sie die Augen, die Musiker weil sie die Ohren ergötzen, obwohl sie uns sonst keinen Nutzen bringen. Ja, der Genuß, den wir aus ihren Werken schöpfen gilt nicht nur als angemessen für den Menschen, er gereicht ihm auch zur Ehre. Welche Unbildung, welche Dummheit daher, dem Geist eine ihm zukommende ehrbare Freude zu neiden, sie aber den Augen und Ohren zu gönnen! [...]

Unser Bildner hat zu den Sinnen den Geist gefügt, nicht bloß, damit sich der Mensch seinen Lebensunterhalt erwerbe – das können viele Arten von Lebewesen mit ihrer unvernünftigen Seele viel geschickter –, sondern auch dazu, daß wir vom Sein der Dinge, die wir mit Augen betrachten, zu den Ursachen ihres Seins und Werdens vordringen, wenn auch weiter kein Nutzen damit verbunden ist. Und wie die anderen Lebewesen sowie der Leib des Menschen durch Speise und Trank erhalten werden, so wird die Seele des Menschen, die etwas vom ganzen Menschen Verschiedenes ist, durch jene Nahrung in der Erkenntnis am Leben erhalten, bereichert, gewissermaßen im Wachstum gefördert. Wer darum nach diesen Dingen kein Verlangen in sich trägt, der gleicht mehr einem Toten als einem Lebenden.

Wie nun die Natur dafür sorgt, daß es den Lebewesen nie an Speise gebricht, so können wir mit gutem Grund sagen, die Mannigfaltigkeit in den Naturerscheinungen sei deswegen so groß, die im Himmelsgebäude verborgenen Schätze so reich, damit dem menschlichen Geist nie die frische Nahrung ausgehe, daß er nicht Überdruß empfinde am Alten, noch zur Ruhe komme, daß ihm vielmehr stets in dieser Welt eine Werkstätte zur Übung seines Geistes offenstehe.

J. Kepler, 1596 [1]

Abstract

This thesis reports on the full spin analysis of the process $e^+e^- \rightarrow \tau^+\tau^-$ using unpolarised electron and positron beams at LEP. Apart from the longitudinal τ polarisation, two additional observables – the transverse-transverse (A_{TT}) and transverse-normal (A_{TN}) spin correlations have been measured. The quantities $\mathcal{A}_\tau$, $\mathcal{A}_e$, A_{TT} and A_{TN} are functions of the vector and axial vector couplings of the neutral current.

The analysis has been performed using the data collected on the Z resonance in 1994 by the L3 detector at LEP corresponding to 50 pb^{-1} of integrated luminosity. The τ polarisation has been determined as a function of the production polar angle using the process $Z \rightarrow \tau\tau \rightarrow \pi X + n\nu$ where X is any one-prong τ decay product. From this measurement one obtains $\mathcal{A}_\tau$, $\mathcal{A}_e$ and $\mathcal{A}_{e-\tau}$ to:

$$\begin{aligned}
\mathcal{A}_\tau &= 0.110 \pm 0.063 \text{ (stat.) } \pm 0.015 \text{ (sys.)} \\
\mathcal{A}_e &= 0.149 \pm 0.095 \text{ (stat.) } \pm 0.011 \text{ (sys.)} \\
\mathcal{A}_{e-\tau} &= 0.122 \pm 0.053 \text{ (stat.) } \pm 0.010 \text{ (sys.)}
\end{aligned}$$

The spin correlations have been measured using the following channels:
$Z \rightarrow \tau\tau \rightarrow e\mu$, $e\pi$, $e\rho$, $\mu\pi$, $\mu\rho$, $\pi\pi$, $\pi\rho$, $\rho\rho$ $+n\nu$. The average values for A_{TT} and A_{TN} are then derived:

$$\begin{aligned}
A_{TT} &= 1.04 \pm 0.26 \text{ (stat.) } \pm 0.06 \text{ (sys.)} \\
A_{TN} &= 0.36 \pm 0.26 \text{ (stat.) } \pm 0.05 \text{ (sys.)}
\end{aligned}$$

The results are in agreement with a value of

$$\sin^2 \bar{\theta}_{\mathrm{W}} = 0.235 \pm 0.007$$

as determined from the τ polarisation measurement.

The observable A_{TT} breaks the symmetry between the vector and axial vector coupling which is present in the τ polarisation measurement. Therefore the positive value alone indicates that the absolute value of the axial vector coupling of the $Z\tau\tau$ vertex is larger than the vector coupling. The phase difference between the neutral current couplings of the τ to the Z has been obtained from a combination of the $\mathcal{A}_{e-\tau}$ and A_{TN} results:

$$\tan(\Phi_{v_\tau} - \Phi_{a_\tau}) = -3.0 \pm 2.5$$

The measurement of the spin correlations provides an independent test of the coupling structure of the Standard Model. Furthermore this analysis completes the measurement of observables related to the spin configuration in $Z \rightarrow \tau\tau$ processes. All results are in agreement with the Standard Model predictions.

Contents

Introduction

A common aim of all science is to explain as many observations as possible with a few simple principles. The discovery of these principles and the verification of their predictions is the goal of a huge number of investigations. To get a deeper understanding it is obvious to classify the natural phenomena in several categories. In the past this attempt led, for example, to the development of the Periodic Table of Elements and to the unification of different types of fundamental interactions in physics, which had previously been considered as independent.

Nowadays physicists have a consistent model to describe various phenomena in particle physics. Within this model matter consists of fermions. The interactions between them are described by boson exchange where the coupling constants determine the strength of the interaction. The free parameters which are not fixed by the model itself can be determined from specific experiments. After the measurement of a minimum set of parameters other observables can be predicted allowing verification or falsification of the theory by comparison with the corresponding experimental results.

Within this context the aim of this thesis is the measurement of correlations between the spin components of a fermion-antifermion pair. The analysis provides essential information on fundamental parameters and the structure of the underlying theory.

The theoretical framework – the electroweak Standard Model – is described in chapter 1. Within this chapter the coupling constants and related observables are defined. The most important properties of the τ lepton are summarised in chapter 2. The experimental setup of the L3 experiment is presented in chapter 3. A detailed description of the performance of the tracking system, which is crucial for this analysis, is given in chapter 4. Chapter 5 explains the experimental methods which are used to determine the neutral current couplings and the spin correlations. The selection of the event sample is discussed in chapter 6. The measurement of the τ polarisation is presented in chapter 7. Chapter 8 shows the results obtained for the spin correlations. Finally, the results are summarised and discussed in chapter 9.

Chapter 1

The Electroweak Standard Model

The Standard Model describes the interactions between elementary particles. The scattering process $e^+e^- \to f\bar{f}$ where f is any fermion is used to perform high precision measurements of the free parameters of the model. The observables related to the spin components are obtained experimentally from the analysis of the τ decay products in the process $e^+e^- \to \tau^+\tau^-$ at centre of mass energies around the Z resonance.

The Standard Model has been described in an accurate and detailed way in many publications. Hence, in this chapter the basic concepts of the electroweak Standard Model are reviewed and the parameters which are relevant for the spin analysis are introduced. The strong interaction which is described by QCD (Quantum Chromo Dynamics) is not considered here.

1.1 The Lagrangian of the Electroweak Standard Model

A basic concept for the construction of a fundamental theory is the analysis of symmetries. The consequence of the requirement of invariance of the Lagrangian under local gauge transformations is the appearance of interaction terms. Therefore the symmetry of the Lagrangian determines the dynamics of the interaction.

The electroweak Standard Model [2, 3, 4] is a non-Abelian local gauge theory based on the group $SU(2)_L \times U(1)_Y$. The generators of the group are the three components of the weak isospin $\vec{T}$ and the hypercharge Y. The Gell-Mann-Nishijima equation $Q = T_3 + Y$ combines the conserved quantities with the electromagnetic charge Q. The left-handed fermions are arranged in the weak isospin doublet with $T_3 = \pm 1/2$. The right-handed fermions remain in singlets with $T=0$. The particle content of the Standard Model is given in table 1.1. The index L and R refers to the left-handed and right-handed particle fields ψ:

$$\psi_L = \frac{1}{2}(1 - \gamma_5)\psi \qquad (1.1)$$

$$\psi_R = \frac{1}{2}(1 + \gamma_5)\psi \qquad (1.2)$$

$$\psi = \psi_L + \psi_R \tag{1.3}$$

The Lagrangian $\mathcal{L}$ of the electroweak interaction can be expressed as the sum of four independent terms:

$$\mathcal{L} = \mathcal{L}_{fermion} + \mathcal{L}_{gauge} + \mathcal{L}_{Higgs} + \mathcal{L}_{Yukawa} \tag{1.4}$$

with:

$$\mathcal{L}_{fermion} = i\bar{\psi}\gamma^\mu D_\mu \psi \tag{1.5}$$

$$\mathcal{L}_{gauge} = -\frac{1}{4}\vec{W}_{\mu\nu}\vec{W}^{\mu\nu} - \frac{1}{4}B_{\mu\nu}B^{\mu\nu} \tag{1.6}$$

$$\mathcal{L}_{Higgs} = D^\mu \phi^\dagger D_\mu \phi - V(\phi) \tag{1.7}$$

$$\mathcal{L}_{Yukawa} = -c_f \left[\bar{R}_f(\phi^\dagger L_f) + (\bar{L}_f \phi)R_f \right] \tag{1.8}$$

where B and $\vec{W}$ are massless gauge fields:

$$\vec{W}_{\mu\nu} = \partial_\mu \vec{W}_\nu - \partial_\nu \vec{W}_\mu + g_2 \vec{W}_\mu \times \vec{W}_\nu \tag{1.9}$$

$$B_{\mu\nu} = \partial_\mu B_\nu - \partial_\nu B_\mu \tag{1.10}$$

The first Lagrangian describes the free propagation of fermions in space and time and their interaction with gauge bosons where the strength of the couplings (g_1 for $U(1)_Y$ and g_2 for $SU(2)_L$) enters in the covariant derivative:

$$D_\mu = \partial_\mu + ig_1 Y B_\mu + ig_2 \frac{\vec{\tau}}{2}\vec{W}_\mu \tag{1.11}$$

The matrix representation of the generators $\vec{\tau} \equiv 2\,\vec{T}$ is known as Pauli spin matrices. The second Lagrangian contains the kinetic term of the massless gauge fields B and $\vec{W}$ and due to the non-Abelian character of the theory the self interactions of the $\vec{W}$ fields. The strengths of these interactions are given by the same coupling g_2 which appears in the fermion Lagrangian. The Higgs and Yukawa Lagrangians are described in the next section.

1.2 Spontaneous Symmetry Breaking

Explicit mass terms for fermions and bosons in the Lagrangian $\mathcal{L}$ would destroy the invariance requirement for $SU(2)_L$ and $U(1)_Y$ transformations. But apart from the photon the observed particles are not massless. The Higgs mechanism solves this theoretical problem and generates the particle masses due to the introduction of an additional complex scalar field [5]:

$$\phi(x) = \left(\begin{array}{c} \phi^{(+)}(x) \\ \phi^{(0)}(x) \end{array} \right) \tag{1.12}$$

Particle	Generations			Q	Y	T_3
Leptons	$\begin{pmatrix} \nu_e \\ e^- \end{pmatrix}_L$	$\begin{pmatrix} \nu_\mu \\ \mu^- \end{pmatrix}_L$	$\begin{pmatrix} \nu_\tau \\ \tau^- \end{pmatrix}_L$	$\begin{matrix} 0 \\ -1 \end{matrix}$	$\begin{matrix} -1/2 \\ -1/2 \end{matrix}$	$\begin{matrix} +1/2 \\ -1/2 \end{matrix}$
	e^-_R	μ^-_R	τ^-_R	-1	-1	0
Quarks	$\begin{pmatrix} u \\ d' \end{pmatrix}_L$	$\begin{pmatrix} c \\ s' \end{pmatrix}_L$	$\begin{pmatrix} t \\ b' \end{pmatrix}_L$	$\begin{matrix} +2/3 \\ -1/3 \end{matrix}$	$\begin{matrix} +1/6 \\ +1/6 \end{matrix}$	$\begin{matrix} +1/2 \\ -1/2 \end{matrix}$
	$\begin{matrix} u_R \\ d'_R \end{matrix}$	$\begin{matrix} c_R \\ s'_R \end{matrix}$	$\begin{matrix} t_R \\ b'_R \end{matrix}$	$\begin{matrix} +2/3 \\ -1/3 \end{matrix}$	$\begin{matrix} +2/3 \\ -1/3 \end{matrix}$	$\begin{matrix} 0 \\ 0 \end{matrix}$
Gauge Bosons	γ			0	0	0
	Z			0	0	0
	W^+			$+1$	0	$+1$
	W^-			-1	0	-1
Higgs	$\phi = \begin{pmatrix} \phi^{(+)} \\ \phi^{(0)} \end{pmatrix}$			$\begin{matrix} 1 \\ 0 \end{matrix}$	$\begin{matrix} +1/2 \\ +1/2 \end{matrix}$	$\begin{matrix} +1/2 \\ -1/2 \end{matrix}$

Table 1.1: The electrical charge, hypercharge and weak isospin assignments for fermions and bosons. The prime indicates that the weak eigenstates of down- or up-type quarks are not their mass eigenstates. The mixing between the quark flavours is described by the CKM-matrix.

The potential of the Higgs Lagrangian $\mathcal{L}_{Higgs}$ is given by:

$$V(\phi) = \mu^2 \phi^\dagger \phi + \lambda (\phi^\dagger \phi)^2 \quad , \quad \lambda > 0 \quad , \quad \mu^2 < 0 \qquad (1.13)$$

The vacuum, defined as a state with minimal energy, is obtained when the potential $V(\phi)$ is minimal. The field configurations satisfying

$$\phi_{min} = \frac{1}{\sqrt{2}} \begin{pmatrix} 0 \\ v \end{pmatrix} \quad , \quad v = \sqrt{-\mu^2/\lambda} \qquad (1.14)$$

constitute an infinite number of solutions. By choosing a particular ground state the symmetry gets spontaneously broken. The excitations around the ground state are parametrised by the new field $\tilde{\phi}$

$$\phi(x) \rightarrow \tilde{\phi}(x) = \frac{1}{\sqrt{2}} \begin{pmatrix} 0 \\ v + H(x) \end{pmatrix} \qquad (1.15)$$

with the Higgs field H and the vacuum expectation value v. The Higgs field corresponds to a new particle. The mass of the scalar boson is $m_H = \sqrt{2\lambda}v$. After an effective replacement of ϕ by $\tilde{\phi}$ the covariant derivative couples the scalar doublet $\phi(x)$ to the $SU(2)_L \times U(1)_Y$ gauge bosons, leading to explicit mass terms for the neutral and charged bosons. In addition, terms describing the Higgs-Gauge-Boson and Higgs self-interactions appear.

The two neutral gauge fields are mixed to form the field Z_μ for the massive neutral vector boson Z and A_μ for the massless photon γ. The observed particles W^+, W^-, Z and γ are associated with the following field combinations:

$$W_\mu^+ = \frac{1}{\sqrt{2}}(W_\mu^1 - iW_\mu^2) \tag{1.16}$$

$$W_\mu^- = \frac{1}{\sqrt{2}}(W_\mu^1 + iW_\mu^2) \tag{1.17}$$

$$A_\mu = B_\mu \cos\theta_W + W_\mu^3 \sin\theta_W \tag{1.18}$$

$$Z_\mu = W_\mu^3 \cos\theta_W - B_\mu \sin\theta_W \tag{1.19}$$

The weak mixing angle, θ_W, is defined by the couplings g_1 and g_2:

$$\sin\theta_W \equiv \frac{g_1}{\sqrt{g_1^2 + g_2^2}} \quad \cos\theta_W \equiv \frac{g_2}{\sqrt{g_1^2 + g_2^2}} \tag{1.20}$$

The ratio of the $W^\pm$ and the Z mass is also determined by the weak mixing angle:

$$\cos\theta_W = \frac{M_W}{M_Z} \tag{1.21}$$

Furthermore the masses of the fermions are generated due to the interaction between the Higgs field and the fermions, which can be described by a Yukawa coupling

$$\mathcal{L}_{Yukawa} = -c_f \left[\bar{R}_f(\phi^\dagger L_f) + (\bar{L}_f \phi)R_f \right] \tag{1.22}$$

where R_f (L_f) is the right(left)-handed fermion representation as shown in table 1.1. The fermion masses are proportional to the vacuum expectation value v and an unknown coupling c:

$$m_f = -\frac{c_f}{\sqrt{2}} v \tag{1.23}$$

Since neutrinos are left-handed only they remain massless.

1.3 Current Representation

The gauge group $SU(2)_L$ contains the charged current interaction between weak left-handed isospin doublets while the third component of the weak isospin and the weak

hypercharge of the $U(1)_Y$ group mix to give the electromagnetic and weak neutral current interactions. The currents corresponding to the gauge groups are:

$$J_i^\mu = \bar{\psi}_L \, \gamma^\mu \, \frac{1}{2} \, \tau^i \, \psi_L \tag{1.24}$$

$$J_Y^\mu = \bar{\psi} \, \gamma^\mu \, Y \, \psi \tag{1.25}$$

The weak hypercharge couples to right and left-handed fermions. The electromagnetic current is given by the combination

$$J_{em}^\mu = J_3^\mu + J_Y^\mu \ , \tag{1.26}$$

following the Gell-Mann-Nishijima relation. Before spontaneous symmetry breaking, the term in the Lagrangian which describes the interaction between fermion and boson fields can be written in terms of currents:

$$\mathcal{L}_{int} = g_1 B_\mu \, J_Y^\mu + g_2 W_\mu^i \, J_i^\mu \tag{1.27}$$

The interaction Lagrangian in terms of physical fields $A_\mu, W_\mu^\pm, Z_\mu$ becomes [1]

$$\begin{aligned} \mathcal{L}_{int} &= \frac{g_1 \, g_2}{\sqrt{g_1^2 + g_2^2}} \, A_\mu \, J_{em}^\mu \\ &+ \sqrt{g_1^2 + g_2^2} \, Z_\mu \, J_{NC}^\mu \\ &+ \frac{g_2}{\sqrt{2}} \, (W_\mu^+ \, J^{+\mu} + W_\mu^- \, J^{-\mu}) \end{aligned} \tag{1.28}$$

where the electromagnetic, neutral and charged currents are introduced as:

$$J_{em}^\mu = J_3^\mu + J_Y^\mu \qquad\qquad = Q \, \bar{\psi} \, \gamma^\mu \, \psi \tag{1.29}$$

$$J_{NC}^\mu = J_3^\mu - \sin^2 \theta_{\rm W} \, J_{em}^\mu \quad = \frac{1}{2} \, \bar{\psi} \, \gamma^\mu \, (v_f - a_f \gamma_5) \, \psi \tag{1.30}$$

$$J^{\pm \, \mu} = \frac{1}{2} \, \bar{\psi} \, \gamma^\mu \, (1 - \gamma_5) \, \tau^\pm \, \psi \tag{1.31}$$

The identification of A_μ with the photon field leads to a relation between the couplings e, g_1 and g_2 and the weak mixing angle $\theta_{\rm W}$,

$$e = \frac{g_1 g_2}{\sqrt{g_1^2 + g_2^2}} = g_1 \cos \theta_{\rm W} = g_2 \sin \theta_{\rm W} \tag{1.32}$$

The currents are commonly written in terms of vector and axial vector coupling constants. The neutral current couplings are given by

$$v_f = T_f^3 - 2 \, Q_f \sin^2 \theta_{\rm W} \tag{1.33}$$

$$a_f = T_f^3 \tag{1.34}$$

---

[1] using the identity $\vec{\tau} \, \vec{W} = \sqrt{2} \, (\tau^+ \, W^+ + \tau^- \, W^-) + \tau^3 \, W^3$ and the definition $\tau^\pm = \frac{1}{2} \, (\tau^1 \pm i\tau^2)$.
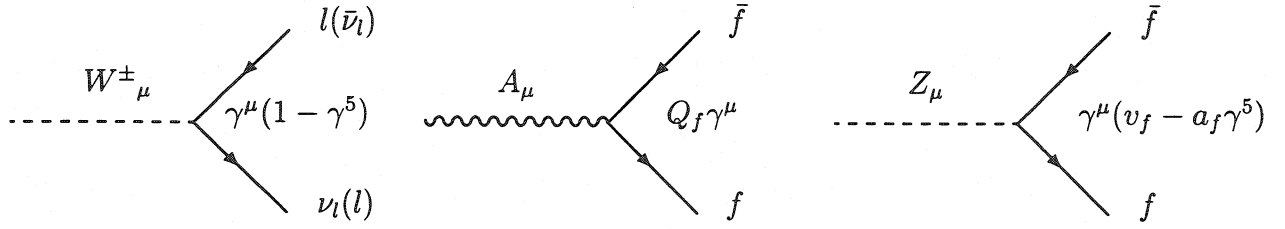
Figure 1.1: The Feynman diagrams for: the weak charged current (left); the electromagnetic current (centre); the neutral current (right) between a fermion anti-fermion pair.

where f labels the fermion type. The assumption of lepton universality leads to $v_e = v_\mu = v_\tau$ and $a_e = a_\mu = a_\tau$. The $(1 - \gamma_5)$ term in equation (1.31) is the reason to talk about the (V-A) structure of the charged current. The neutral current contains both vector and axial vector couplings. The fermion-boson interactions are illustrated by the Feynman diagrams in figure 1.1.

1.4 Helicity Formalism

In order to introduce the fermion helicity the Dirac equation is considered in the Weyl representation

$$\begin{pmatrix} -\vec{\sigma} \cdot \vec{p} & m \\ m & \vec{\sigma} \cdot \vec{p} \end{pmatrix} \psi = E\psi \tag{1.35}$$

where $\vec{\sigma}$ is the vector of Pauli matrices, m is the mass and $\vec{p}$ the momentum of the particle. The four component spinor ψ can be written in terms of two-component spinors:

$$\psi = \begin{pmatrix} \chi \\ \varphi \end{pmatrix} \tag{1.36}$$

In the Weyl representation,

$$\gamma_5 = \begin{pmatrix} -1 & 0 \\ 0 & 1 \end{pmatrix} \tag{1.37}$$

and the left and right handed components are:

$$\psi_L = \frac{1}{2}(1 - \gamma_5)\psi = \begin{pmatrix} \chi \\ 0 \end{pmatrix} \tag{1.38}$$

$$\psi_R = \frac{1}{2}(1 + \gamma_5)\psi = \begin{pmatrix} 0 \\ \varphi \end{pmatrix} \tag{1.39}$$

The introduction of the two-component spinors in the Dirac equation yields:

$$\frac{\vec{\sigma} \cdot \vec{p}}{|\vec{p}|}\chi = \frac{-E}{|\vec{p}|}\chi + \frac{m}{|\vec{p}|}\varphi \tag{1.40}$$

$$\frac{\vec{\sigma} \cdot \vec{p}}{|\vec{p}|}\varphi = \frac{E}{|\vec{p}|}\varphi - \frac{m}{|\vec{p}|}\chi \tag{1.41}$$
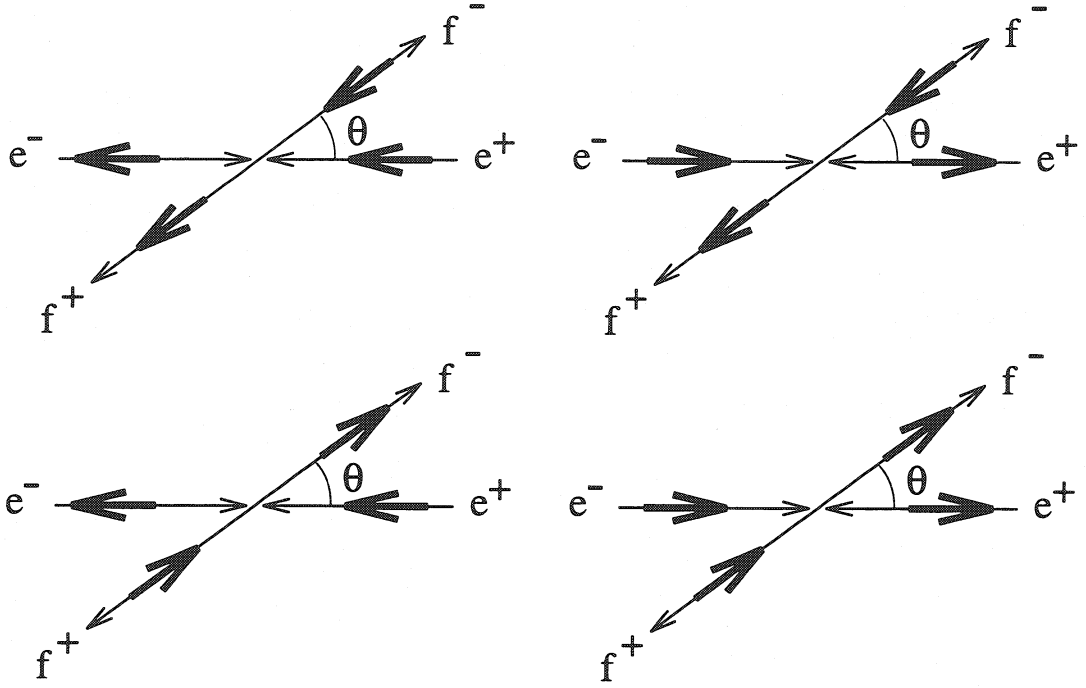
Figure 1.2: Initial and final state fermion spin configurations allowed by helicity conservation. The thin arrows show the particle momenta and the thick arrows indicate the spin.

In the high energy limit $E \gg m$ these equations decouple with χ and φ as eigenstates of the helicity operator $\hat{H} = \vec{\sigma} \cdot \hat{p}$ with $\hat{p} = \vec{p}/|\vec{p}|$.

$$\hat{H}\chi = -\chi \tag{1.42}$$
$$\hat{H}\varphi = \varphi \tag{1.43}$$

As can be seen from the helicity operator, helicity is the projection of the spin along the direction of motion. In the massless limit the left and right handed fields $\psi_{L,R}$ are identical to the helicity eigenstates. ψ_L represents a fermion with spin in the direction opposite to its momentum, or a fermion with negative helicity. For $m \neq 0$ there is a contribution from the opposite helicity state which is suppressed by a factor $1/\gamma$.

The vertex factor for the neutral current contains a linear combination of $\frac{1}{2}(1 - \gamma_5)$ and $\frac{1}{2}(1 + \gamma_5)$, so that in general the Z couples to left and right handed fermions.

If the weak neutral current contains only vector and axial vector couplings, helicity is conserved in the relativistic limit which implies that the initial state e^+e^- and the final state f^+f^- can only involve fermions of opposite helicity. The four possible helicity configurations are shown in figure 1.2.

1.5 Status of the Standard Model

The free parameters of the electroweak Standard Model are the coupling constants g_1 and g_2, the vacuum expectation value v, the fermion masses m_f, the mass of the Higgs boson m_H and three angles and one phase of the quark mass mixing (CKM) matrix [6]. Since the theory does not predict the number of free parameters their large number is no strong hint for physics beyond the Standard Model.

Three generations of fermions are discovered. The existence of the τ neutrino is inferred from the study of weak τ decays. Since no τ lepton production in ν_μ and ν_e interactions was observed the lepton flavour of the third generation has to be different from the first and second generation. In addition the number of light neutrino species has been measured at LEP to be three [7]. No ν_τ induced charged or neutral current reaction has been detected so far. The upper mass limit for the τ neutrino mass is $m_{\nu_\tau} < 18$ MeV [8].

Furthermore the Higgs particle has not been observed at existing colliders. The lower mass limit is $m_H > 66$ GeV [9].

Only the electromagnetic and the weak interactions are unified in the electroweak Standard Model. The strong interaction was formulated as a quantum field theory, but is not unified with any other interaction. The introduction of spontaneous symmetry breaking to create the masses of the particles is not regarded to be based on a fundamental principle. Any other mechanism could be used to generate masses. The parameters of the CKM-matrix are purely phenomenological to describe the weak decays of quarks. Within this context CP violation is described by the complex phase in the CKM-matrix. The (V-A) structure of the charged current was implemented to describe the experimental results. There is no physical reason why neutrinos should be massless and left-handed only. The origin of the masses and the existence of more than one generation is not understood.

To summarise the status of the Standard Model one has to mention that many phenomenological constants enter the model without any understanding of possible underlying physical principles. There are many questions which remain unanswered. On the other hand all experimental results are in excellent agreement with the Standard Model predictions. Nevertheless not all predictions are investigated so far. Especially the terms representing the spin correlations are not analysed.
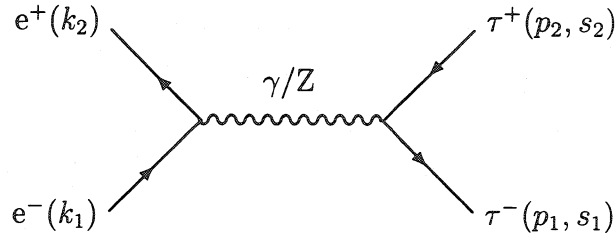
Figure 1.3: Tree level Feynman diagram of the process $e^+e^- \to \tau^+\tau^-$.

1.6   The Process $e^+e^- \to \tau^+\tau^-$

The full spin analysis in $e^+e^- \to f\bar{f}$ processes is based on observables related to the particle spin components. The $\tau^+\tau^-$ final state gives the unique possibility to get information of the spin configuration of the event by exploiting the spin information carried by the τ decay products. Hence only the $\tau^+\tau^-$ final state is considered here although the following calculations are valid for any fermion pair. The basic properties of the τ lepton are given in chapter 2.

To lowest order in perturbation theory, the amplitude for the process

$$e^-(k_1)\, e^+(k_2) \to \tau^-(p_1, s_1)\, \tau^+(p_2, s_2)$$

is given by the sum of the contributions associated with γ and Z exchange as illustrated in figure 1.3. The momenta of the particles are k and p as indicated and s_1 (s_2) are the spin vectors of the τ^- (τ^+). Assuming chirality conserving interactions the calculation of the matrix element M_0 yields the equation [10, 11]:

$$M_0 = M_0^\gamma + M_0^Z \tag{1.44}$$

$$M_0^\gamma = ie^2 \frac{Q_e Q_\tau}{s} \overline{v}(k_2)\gamma_\mu u(k_1)\overline{u}(p_1)\gamma^\mu v(p_2) \tag{1.45}$$

$$M_0^Z = i\frac{e^2}{4\sin^2\theta_W \cos^2\theta_W}\chi_0(s)$$

$$\times \quad \overline{v}(k_2)\gamma_\mu(v_e - a_e\gamma_5)u(k_1)\overline{u}(p_1)\gamma^\mu(v_\tau - a_\tau\gamma_5)v(p_2) \tag{1.46}$$

where $M_0^\gamma (M_0^Z)$ describes the pure photon (Z boson) exchange, u and v are Dirac spinors and $s = (k_1 + k_2)^2$ is the squared centre of mass energy. The Z propagator

$$\chi_0(s) = \frac{1}{s - M_Z^2 + iM_Z\Gamma_Z} \tag{1.47}$$

	γ	$\gamma - Z$	Z
$F_0(s)$	α^2	$2\alpha v_e v_\tau \mathrm{Re}P(s)$	$C_0\,|P(s)|^2$
$F_1(s)$		$2\alpha a_e a_\tau \mathrm{Re}P(s)$	$C_1\,|P(s)|^2$
$F_2(s)$	$-\alpha^2$	$-2\alpha v_e v_\tau \mathrm{Re}P(s)$	$C_2\,|P(s)|^2$
$G_0(s)$		$2\alpha v_e a_\tau \mathrm{Re}P(s)$	$D_0\,|P(s)|^2$
$G_1(s)$		$2\alpha a_e v_\tau \mathrm{Re}P(s)$	$D_1\,|P(s)|^2$
$G_2(s)$		$2\alpha v_e a_\tau \mathrm{Im}P(s)$	$D_2\,|P(s)|^2$

Table 1.2: The functions F_i and G_i are given by the sum of the contributions from γ and Z exchange and their interference.

is given in the Breit Wigner approximation with the mass(width) $M_Z(\Gamma_Z)$ of the Z boson. To include the spin contributions explicitly the cross section will be computed for the spin directions s_1^* and s_2^* which are unit vectors in the τ^- and τ^+ rest frames. In the laboratory frame the z-axis points in the direction of the τ^- momentum $(\vec{p}_1)$. The y-axis is defined by the vector product $\vec{p}_1 \times \vec{k}_1$ where $\vec{k}_1$ is the direction of the incident electron beam. Using the matrix element and averaging over the initial helicity states, the differential cross-section for τ pair production with spin vectors s_1^* and s_2^* has the following form [12, 13]:

$$\frac{d\sigma}{d\Omega}(s_1^*, s_2^*) = \frac{1}{16s}\{(1 + s_{1z}^* s_{2z}^*)[F_0(s)(1 + \cos^2\theta) + F_1(s)2\cos\theta]$$
$$- (s_{1z}^* + s_{2z}^*)[G_0(s)(1 + \cos^2\theta) + G_1(s)2\cos\theta]$$
$$+ [(s_{1y}^* s_{2y}^* - s_{1x}^* s_{2x}^*)F_2(s) + (s_{1y}^* s_{2x}^* + s_{1x}^* s_{2y}^*)G_2(s)]\sin^2\theta\} \quad (1.48)$$

The scattering angle θ is the τ^- polar angle with respect to the electron direction. The functions $F_i(s)$ and $G_i(s)$ (i=0,1,2) are given in table 1.2 where the contributions from γ exchange, Z exchange and their interference are shown separately. The $F_i(s)$ are associated with parity-conserving terms whereas $G_i(s)$ correspond to parity-violating observables. The following constants are defined in the improved Born approximation which will be described in section 1.9:

$$C_0 = (|v_e|^2 + |a_e|^2)(|v_\tau|^2 + |a_\tau|^2)$$
$$C_1 = 4\,\mathrm{Re}(v_e a_e^*)\,\mathrm{Re}(v_\tau a_\tau^*)$$
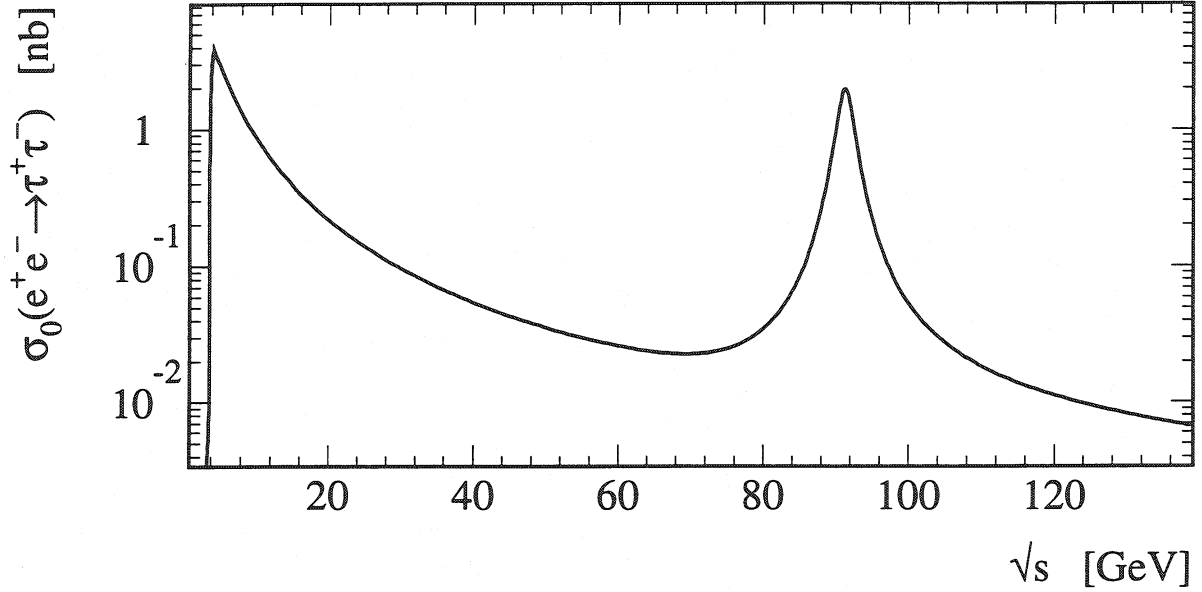$$C_2 = (|v_e|^2 + |a_e|^2)(|a_\tau|^2 - |v_\tau|^2) \quad (1.49)$$

Figure 1.4: The figure shows the Born cross section σ_0 for τ pair production as a function of the centre of mass energy. In the low energy range the $1/s$ dependence of the photon exchange dominates. The cross section shows resonant behaviour around 90 GeV due to Z boson exchange.

$$
\begin{aligned}
D_0 &= 2\,\mathrm{Re}(v_\tau a_\tau^*)\left(|v_e|^2 + |a_e|^2\right) \\
D_1 &= 2\,\mathrm{Re}(v_e a_e^*)\left(|v_\tau|^2 + |a_\tau|^2\right) \\
D_2 &= -2\,\mathrm{Im}(v_\tau a_\tau^*)\left(|v_e|^2 + |a_e|^2\right)
\end{aligned}
\tag{1.50}
$$

The neutral current couplings are real at Born level and complex in the improved Born approximation. The imaginary parts of the couplings are at the 10^{-3} level. The Z propagator is contained in $P(s)$ using the following notation:

$$
P(s) = \frac{\alpha(M_Z)\, s\, \chi_0(s)}{4\sin^2\bar\theta_W \cos^2\bar\theta_W}
\tag{1.51}
$$

where α is the running fine structure constant. All functions except $G_2(s)$ have an interference term proportional to $\mathrm{Re}P(s)$, which vanishes on the Z resonance. Due to the resonance structure $|P(s)|^2$ becomes large around centre of mass energies $\sqrt{s} \approx M_Z$ and as a consequence the Z exchange dominates over all other contributions to the cross section. The cross section is shown in figure 1.4.

1.7 Asymmetries in the Process $e^+e^- \to \tau^+\tau^-$

Since the Lorentz structure of the electroweak theory involves different left and right handed couplings to the Z, parity is violated in Z production and Z decay. As a consequence the production cross section depends on the helicity state of the τ. Choosing the τ^- momentum as the z-axis, the helicity of the τ^- becomes in the high energy limit $h_\tau = s_{1z}^*$. The degree of polarisation depends on the vector and axial vector couplings as well as on the scattering angle. In order to get experimental access to the coupling constants the following asymmetries are defined:

1. forward-backward asymmetry, A_{fb}:

$$
\begin{aligned}
A_{fb} &= \frac{\sigma(\cos\theta < 0) - \sigma(\cos\theta > 0)}{\sigma(\cos\theta < 0) + \sigma(\cos\theta > 0)} \\
&= \frac{3}{4}\frac{F_1(s)}{F_0(s)}
\end{aligned}
\tag{1.52}
$$

2. polarisation asymmetry, A_{pol}:

$$
\begin{aligned}
A_{pol} &= \frac{\sigma(h_\tau = +1) - \sigma(h_\tau = -1)}{\sigma(h_\tau = +1) + \sigma(h_\tau = -1)} \\
&= -\frac{G_0(s)(1 + \cos^2\theta) + G_1(s)2\cos\theta}{F_0(s)(1 + \cos^2\theta) + F_1(s)2\cos\theta}
\end{aligned}
\tag{1.53}
$$

3. forward-backward polarisation asymmetry, A_{pol}^{fb}:

$$
\begin{aligned}
A_{fb}^{pol} &= \frac{\sigma(h_\tau\cos\theta > 0) - \sigma(h_\tau\cos\theta < 0)}{\sigma(h_\tau\cos\theta > 0) + \sigma(h_\tau\cos\theta < 0)} \\
&= \frac{3}{4}\frac{G_1(s)}{F_0(s)}
\end{aligned}
\tag{1.54}
$$

Neglecting the small γ exchange contribution, the asymmetries on the Z resonance can be written as:

$$
A_{fb} = \frac{3}{4}\frac{C_1}{C_0} = \frac{3}{4}\mathcal{A}_e\mathcal{A}_\tau
\tag{1.55}
$$

$$
A_{fb}^{pol} = \frac{3}{4}\frac{D_1}{C_0} = \frac{3}{4}\mathcal{A}_e
\tag{1.56}
$$

$$
\mathcal{P}_\tau = -\frac{D_0}{C_0} = -\mathcal{A}_\tau
\tag{1.57}
$$

$$
A_{pol} = -\frac{\mathcal{A}_\tau(1 + \cos^2\theta) + 2\mathcal{A}_e\cos\theta}{(1 + \cos^2\theta) + 2\mathcal{A}_e\mathcal{A}_\tau\cos\theta}
\tag{1.58}
$$

with:

$$\mathcal{A}_f = \frac{2 v_f \, a_f}{|a_f|^2 + |v_f|^2} \quad f = e, \tau \tag{1.59}$$

$\mathcal{P}_\tau$ denotes the τ polarisation averaged over the τ production angles. Note that the polarisation asymmetries are linear in $\mathcal{A}_f$ and that A_{fb}^{pol} depends only on the electron couplings. Therefore the analysis of τ pair final states provides the unique possibility to measure the neutral current couplings of the electron and τ lepton simultaneously. The asymmetries are only sensitive to the relative sign of the couplings, because they are symmetric in a_f and v_f. The constant C_0 can be derived from the total cross section measurement.

The quantity $\mathcal{A}_e$ can also be measured using longitudinally polarised electron beams. The left right asymmetry A_{LR} between the cross section of left-handed (σ_L) and right-handed (σ_R) electrons is:

$$A_{LR} = \frac{\sigma_L - \sigma_R}{\sigma_L + \sigma_R} = \mathcal{A}_e \tag{1.60}$$

In order to illustrate the asymmetries the cross section may be written in terms of helicity amplitudes [14]. The basic scattering processes are shown in figure 1.2.

$$\sigma_1 = \sigma \left(e_L^- e_R^+ \to \tau_R^- \tau_L^+ \right) \tag{1.61}$$

$$\sigma_2 = \sigma \left(e_L^- e_R^+ \to \tau_L^- \tau_R^+ \right) \tag{1.62}$$

$$\sigma_3 = \sigma \left(e_R^- e_L^+ \to \tau_R^- \tau_L^+ \right) \tag{1.63}$$

$$\sigma_4 = \sigma \left(e_R^- e_L^+ \to \tau_L^- \tau_R^+ \right) \tag{1.64}$$

The observables described above are obtained by linearly independent combinations of the σ_i ($i = 1, ..., 4$):

$$\begin{bmatrix} \sigma_{tot} \\ \sigma_{pol} \\ \sigma_{fb} \\ \sigma_{LR} \end{bmatrix} = \begin{bmatrix} 1 & 1 & 1 & 1 \\ -1 & 1 & -1 & 1 \\ -1 & 1 & 1 & -1 \\ 1 & 1 & -1 & -1 \end{bmatrix} \cdot \begin{bmatrix} \sigma_1 \\ \sigma_2 \\ \sigma_3 \\ \sigma_4 \end{bmatrix} \tag{1.65}$$

The normalisation of the cross sections leads to the asymmetries defined above.

1.8 Spin Correlations

The asymmetries (1.52) – (1.54) have been intensively studied by all LEP experiments since the data taking started in 1989.

However, not all observables have been investigated so far. As can be seen from equation (1.48), the coefficients C_2 and D_2 are associated with the x and y-spin components of both τ's. Using the notation of transverse and normal polarisations P_T and P_N, which are related to the x, y-components of the τ^- spin vector and illustrated in figure 1.5, the expectation value of the spin correlations is defined as

$$
\begin{aligned}
< P_T \bar{P}_T > \ &\equiv\ \frac{\sigma(s^*_{1x}s^*_{2x} = -1) - \sigma(s^*_{1x}s^*_{2x} = +1)}{\sigma(s^*_{1x}s^*_{2x} = -1) + \sigma(s^*_{1x}s^*_{2x} = +1)} \\[2mm]
&=\ \frac{F_2(s)\sin^2\theta}{F_0(s)(1+\cos^2\theta) + F_1(s)2\cos\theta}
\end{aligned}
\tag{1.66}
$$

$$
\begin{aligned}
< P_T \bar{P}_N > \ &\equiv\ \frac{\sigma(s^*_{1y}s^*_{2x} = -1) - \sigma(s^*_{1y}s^*_{2x} = +1)}{\sigma(s^*_{1y}s^*_{2x} = -1) + \sigma(s^*_{1y}s^*_{2x} = +1)} \\[2mm]
&=\ \frac{-G_2(s)\sin^2\theta}{F_0(s)(1+\cos^2\theta) + F_1(s)2\cos\theta}
\end{aligned}
\tag{1.67}
$$

where $\bar{P}_{T,N}$ is assigned to the τ^+. On the Z peak this can be expressed as

$$
< P_T \bar{P}_T > = \frac{-A_{TT}\sin^2\theta}{(1+\cos^2\theta) + 2\mathcal{A}_e\mathcal{A}_\tau\cos\theta}
\tag{1.68}
$$

$$
< P_T \bar{P}_N > = \frac{A_{TN}\sin^2\theta}{(1+\cos^2\theta) + 2\mathcal{A}_e\mathcal{A}_\tau\cos\theta}
\tag{1.69}
$$

with the introduction of the normalised spin correlations:

$$
A_{TT} \equiv \frac{C_2}{C_0} = \frac{|a_\tau|^2 - |v_\tau|^2}{|a_\tau|^2 + |v_\tau|^2}
\qquad
A_{TN} \equiv \frac{D_2}{C_0} = -\frac{2\,\text{Im}(v_\tau a^*_\tau)}{|a_\tau|^2 + |v_\tau|^2}
\tag{1.70}
$$

From equation (1.48) the following relations hold:

$$
< P_T \bar{P}_T > = - < P_N \bar{P}_N >
\qquad
< P_T \bar{P}_N > = < P_N \bar{P}_T >
\tag{1.71}
$$

The normal-normal spin correlations coincide with the transverse-transverse ones except for the sign. The transverse-normal and normal-transverse spin correlations are identical. For this reason, one speaks only about transverse-transverse and transverse-normal spin correlations in τ pair production. The expectation values (1.68) and (1.69) depend on the neutral current couplings and the scattering angle θ, where the structure of the equations is similar to these for the polarisation asymmetry A_{pol} (equation (1.58)). In addition, A_{TT} is not symmetric in the absolute values of the vector and axial vector couplings. Therefore its value alone will indicate which of these two couplings is larger.
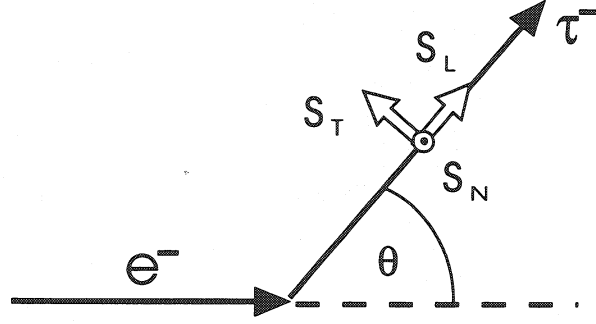
Figure 1.5: The spin configuration for the τ^-. A collision plane is defined by the electron beam and the τ^-. The longitudinal spin component, S_L, points in the direction of the τ^-. The transverse component, S_T, is normal to the τ^- direction within the collision plane and the normal component, S_N, is normal to the τ^- direction perpendicular to the collision plane.

Using $\sin^2 \theta_W = 0.23$ the Standard Model predicts:

$$A_{TT} = 0.99 \tag{1.72}$$

The transverse-normal spin correlation A_{TN} is both a parity-odd and time reversal-odd observable. In the Standard Model a small non-vanishing value for A_{TN} exists due to electroweak radiative corrections to the Z decay amplitudes [15, 16]. If the γ-Z interference is included, A_{TN} is modified:

$$A_{TN} = -\frac{2\,\mathrm{Im}(v_\tau a_\tau^*)}{|a_\tau|^2 + |v_\tau|^2} - \frac{2\sin^2\theta_W \cos^2\theta_W 4\mathrm{Re}(v_e a_\tau^*)\Gamma_Z}{\left(|v_e|^2 + |a_e|^2\right)\left(|v_\tau|^2 + |a_\tau|^2\right)M_Z} \tag{1.73}$$

The Standard Model predicts

$$A_{TN} \approx 0.025 - 0.012 \tag{1.74}$$

where the first contribution comes from the imaginary couplings and the second one contains the γ-Z interference. A hypothetical unknown particle which interferes with the photon and Z boson, e.g. Z', would give a further contribution to A_{TN} [17].

Neglecting the γ-Z interference A_{TN} can be used in combination with $\mathcal{P}_\tau$ to determine the phase difference between vector and axial vector couplings:

$$A_{TN} = \frac{D_2}{C_0} = -\frac{2\,\mathrm{Im}(v_\tau a_\tau^*)}{|a_\tau|^2 + |v_\tau|^2}$$

$$= -\frac{2\,|v_\tau||a_\tau|}{|a_\tau|^2 + |v_\tau|^2}\sin(\Phi_{v_\tau} - \Phi_{a_\tau}) \tag{1.75}$$

$$\mathcal{P}_\tau = -\frac{D_0}{C_0} = -\frac{2\,\mathrm{Re}(v_\tau a_\tau^*)}{|a_\tau|^2 + |v_\tau|^2}$$

$$= -\frac{2\,|v_\tau||a_\tau|}{|a_\tau|^2 + |v_\tau|^2}\cos(\Phi_{v_\tau} - \Phi_{a_\tau}) \tag{1.76}$$
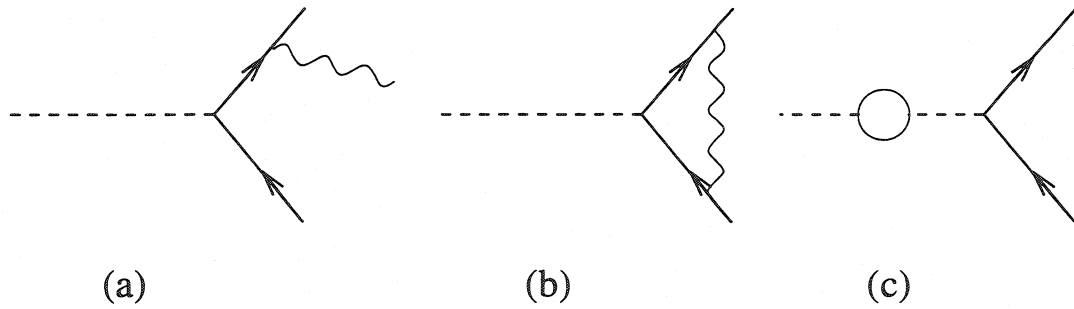
(a)   (b)   (c)

Figure 1.6: Radiative corrections from real photon emission (a), vertex corrections (b) and propagator corrections (c).

so:

$$\tan(\Phi_{v_\tau} - \Phi_{a_\tau}) = \frac{A_{TN}}{\mathcal{P}_\tau} \tag{1.77}$$

where the phases are defined by:

$$a_\tau = |a_\tau|\, e^{i\Phi_{a_\tau}} \qquad v_\tau = |v_\tau|\, e^{i\Phi_{v_\tau}} \tag{1.78}$$

In order to complete the measurement of the constants C_i, D_i (i=0,1,2) which appear in the differential cross section the spin correlations have to be analysed. Their measurement provides an independent test of the coupling structure of the theory.

The measurement of the τ polarisation and the spin correlations is based on the analysis of the angular distributions of the τ decay products. The experimental methods are described in chapter 5.

1.9 Radiative Corrections

To compare the experimental measurements of physical observables with the theoretical predictions the precision of the Born level calculations is not always sufficient. To get a more accurate prediction the most important radiative corrections have to be taken into account. The radiative corrections are usually divided into two subclasses [11]:

- The QED (or photonic) corrections involve in first order one extra photon which is added to the Born diagrams, either in the form of a real bremsstrahlung photon (Figure 1.6a) or as a virtual photon loop (Figure 1.6b). The dominant contribution is due to initial state radiation and is treated convoluting the Born cross section using a radiator function.

- The weak (or non-photonic) corrections involve all other one-loop diagrams like the vector boson propagator corrections (Figure 1.6c) and weak vertex corrections.

These corrections can be absorbed in the lowest order Born term formulae by the introduction of s-dependent coupling constants. The self energy contribution to the photon propagator leads to a running, i.e. s-dependent, electromagnetic fine structure constant $\alpha \rightarrow \alpha(s)$. The corrections to the Z boson propagator are taken into account by a s-dependent Z width $\Gamma_Z \rightarrow \Gamma_Z(s)$. The neutral current couplings are replaced by:

$$v_f \quad \rightarrow \quad v_f(s) = \sqrt{\rho_f(s)}\,(T_f^3 - 2\kappa_f(s)Q_f \sin^2\theta_W) \qquad (1.79)$$

$$a_f \quad \rightarrow \quad a_f(s) = \sqrt{\rho_f(s)}\,T_f^3 \qquad\qquad\qquad\qquad (1.80)$$

These modifications lead to the *improved Born approximation* [18]. For energies around the Z resonance the s-dependent factors ρ and κ are approximated by s-independent effective factors $\bar{\rho}(s = M_Z^2)$ and $\bar{\kappa}(s = M_Z^2)$ leading to *effective* vector and axial vector couplings of the weak neutral current. The *effective* weak mixing angle is then defined by:

$$\sin^2\bar{\theta}_W \equiv \bar{\kappa}\sin^2\theta_W \qquad\qquad (1.81)$$

Although the factors ρ and κ have to be calculated for all fermion species separately, they turn out to be equal to each other except for b-quarks. Typical values are $\bar{\kappa} = 1.037$ and $\bar{\rho} = 1.003$.

Chapter 2

The τ Lepton

The Discovery of the τ Lepton

The existence of the second particle generation was already well established in the early seventies. The possibility of a third sequential heavy lepton was first discussed by Y.S. Tsai. In a publication of 1971 the main particle properties, e.g. decay modes, branching fractions and lifetime, were predicted in dependence of the mass of the hypothetical heavy lepton [13].

In 1973 a new search for heavy leptons started with the operation of the SPEAR (Stanford Positron Electron Asymmetric Rings) e^+e^- collider at SLAC (Stanford Linear Accelerator Center). A pair of unknown heavy leptons produced in e^+e^--annihilation should decay for example with the following signature.

$$e^+e^- \rightarrow e^\pm \mu^\mp + \text{missing energy}$$

One year later the first events of this type were observed in the MARK-I detector. The first international presentation was given at the *1975 Summer School of the Canadian Institute for Particle Physics* [19]. In 1975 – four years after the theoretical considerations – the discovery of a new pair of particles with a mass between 1.6 and 2.0 GeV/c^2 was published by M.L Perl *et al.* [20]. The results were confirmed by several experiments and the new lepton was called Tau from the Greek word $\tau\rho\iota\rho\phi\nu$ for third [21]. The discovery of the first fermion of the third generation was honoured with the Nobel prize for physics in 1995.

The Properties of the τ Lepton

The mass of the τ lepton has been most precisely measured by the BES collaboration [22]. The world average is [23]:

$$m_\tau = 1777.00 \, {}^{+0.30}_{-0.27} \, \text{MeV} \tag{2.1}$$

The τ lifetime has been measured to be [23]:

$$\tau_\tau = 291.0 \pm 1.5 \, \text{fs} \tag{2.2}$$

Decay mode	Branching Ratio [%]
$\tau \to e\,\nu\,\nu$	17.83 ± 0.08
$\tau \to \mu\,\nu\,\nu$	17.35 ± 0.10
$\tau \to \pi\,\nu$	11.31 ± 0.15
$\tau \to \pi\,\pi^0\,\nu$	25.24 ± 0.16
$\tau \to \pi\,\pi^0\,\pi^0\,\nu$	9.50 ± 0.14

Table 2.1: The one-prong branching ratios of the τ lepton [23].

The average τ decay length at LEP energies is 2.3 mm. Since the τ lepton is heavier than many hadrons, semi-hadronic decays are kinematically allowed. This fact is used to determine, apart from the τ lifetime and branching fractions, the strong coupling constant α_s at $q^2 = m_\tau^2$ [25, 26]. The decay into strange hadrons is suppressed by the Cabibbo angle θ_C [24]. The branching fractions of the one-prong τ decay modes are given in table 2.1.

The τ pairs are produced in neutral current processes, as shown in figure 1.3. At LEP energies the Z exchange is dominant. The analysis of the total cross section, the forward-backward asymmetry, the polarisation asymmetry and the forward-backward polarisation asymmetry allows measurements of the neutral current couplings v_f, a_f (f = e,τ) to be made with high accuracy. These provide a test of lepton universality in the neutral current sector.

Furthermore the Lorentz structure of weak decays and the lepton universality of the charged current have been investigated [27, 28]. The ν_τ helicity has been determined to be in agreement with $h_{\nu_\tau} = -1$ [29]. The properties of the τ lepton are summarised in [30, 31].

Chapter 3

The L3 Experiment at LEP

3.1   The Large Electron Positron Collider

The Large Electron Positron collider (LEP) [32] at CERN is situated in a tunnel of 26.7 km circumference between the Jura mountains and the Lake Geneva. The e^+e^- collider was taken into operation in 1989 in order to study e^+e^--annihilation at centre of mass energies around the Z resonance. The production of large numbers of Z bosons allows the following investigations to be made:

1. measurement of the mass and width of the Z boson

2. determination of the number of light neutrino species

3. measurement of the neutral current couplings of leptons and quarks

4. search for new particles, new interactions and new phenomena

5. study of strong interactions and/or weak charged current processes of fermions produced in Z decays

Due to the installation of further cavities the energy range was extended to $\sqrt{s} = 172$ GeV in 1996. This new energy domain allows the investigation of $W^\pm$ pair production and makes it possible to search for new heavy particles.

The LEP storage ring is the last accelerator in a chain of five. In a first step electrons are accelerated in a linear accelerator up to 200 MeV. A fraction of these electrons is used to create positrons by scattering the electron beam on a fixed tungsten target. Both electrons and positrons are accelerated up to 600 MeV using the LEP Injector Linacs. In the following Electron Positron Accumulator (EPA), the bunch structure is made. After bringing the bunches into the Proton Synchrotron (PS) the energy increases to 3.5 GeV. The PS then injects into the Super Proton Synchrotron (SPS) which operates as a 20 GeV injector for LEP. Finally the particles are accelerated to the nominal centre of mass energy within the LEP ring itself. The electron-positron interactions are produced by 4×4 (or 8×8) bunches of 10^{11} particles each. The LEP complex is shown in figure 3.1.

21
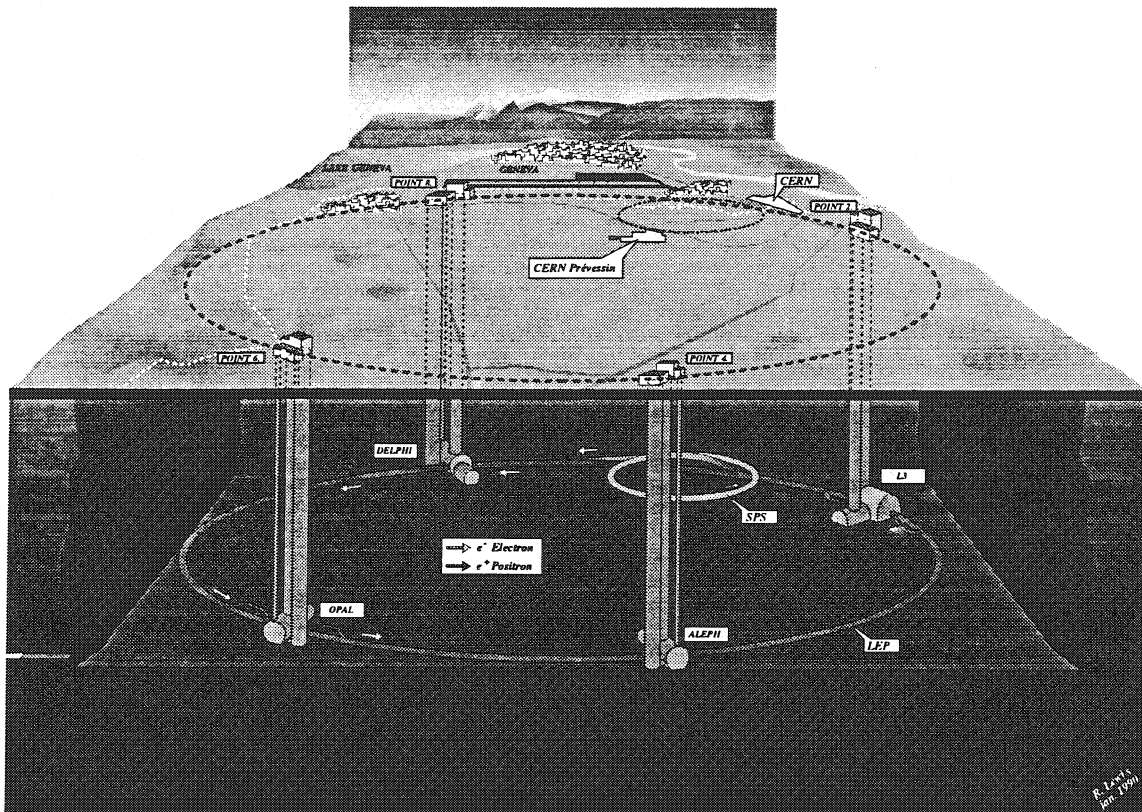
Figure 3.1: The CERN accelerator complex. The experiments ALEPH, DELPHI, L3 and OPAL are located in the four underground areas.

The LEP ring consists of eight bending sections each 2840 m in length, connected by eight 490 m long straight sections. The LEP experiments ALEPH, DELPHI, L3 and OPAL are located in four of the straight sections. Two of the straight sections contain the radio-frequency cavities which accelerate the beam to the nominal energy and compensate for the energy lost due to synchrotron radiation in the curved sections.

3.2   The L3 Detector

The L3 detector [33] shown in figure 3.2 was designed to study e^+e^- collisions up to an energy of 200 GeV, with emphasis on precision energy measurements of electrons, photons, muons and jets. The detector consists of several subdetectors, installed within a 0.5 T magnetic field, covering symmetrically the interaction point, which are described in subsequent sections. The major parts are:

- Silicon Microvertex Detector (SMD, since 1993)
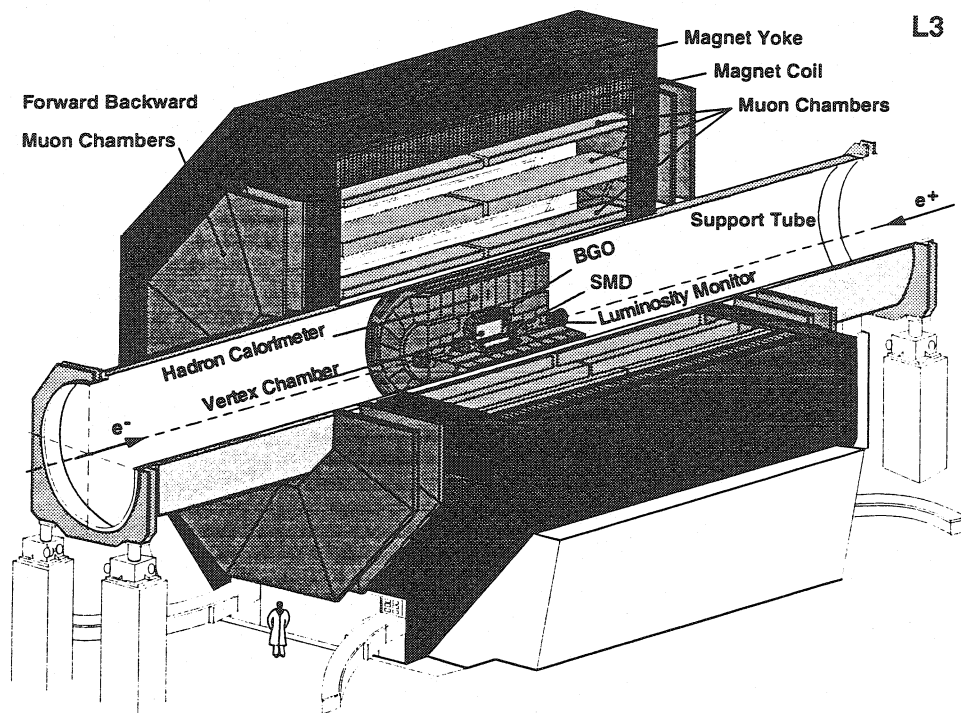
Figure 3.2: A perspective view of the L3 detector. The SMD is installed since 1993. The forward-backward muon chambers were mounted in 1994.

- Time Expansion Chamber (TEC)

- Z-Chamber (ZCH)

- electromagnetic calorimeter (BGO)

- scintillation counters

- hadron calorimeter (HCAL)

- muon filter

- muon detector (forward - backward muon chambers since 1995)

- luminosity monitor

The inner detectors are installed in a 32 m long, 4.45 m diameter steel tube. The tube is aligned concentrically with the beam pipe. The muon spectrometer is mounted on the outside of the tube. The central section of the inner detectors are arranged as 'barrel' elements around the beam pipe and as 'endcap' modules in the forward-backward regions.

3.2.1   The Coordinate System

The origin of the L3 coordinate system is defined by the nominal interaction point. The z-axis points in the direction of the e⁻ beam, the y-axis vertically upwards and the x-axis to the centre of the LEP ring. Due to the constant magnetic field a charged particle forms a helicoidal track in the L3 detector. The trajectory is described by a circle in the (x, y) plane. The projection of the helix in the (s, z) plane is a straight line. The variable s at a point (x, y, z) is given by the arc length of the track in the (x, y) plane. The angle ϕ is defined in the (x, y) plane with respect to the x-axis, where the distance to the origin is given by the radius r. The polar angle θ is defined in the (s, z) plane with respect to the z-axis [34].

3.2.2   The Magnet

The magnet is an octagonal aluminium coil, inside an iron return yoke. The inner diameter and length of the magnet are 12 m. Within this volume, the conventional magnet provides a uniform 0.5 T field parallel to the beam axis. The magnetic field is mapped inside the steel tube with hall probes and outside the tube with magneto-resistors mounted on the muon spectrometer. In addition five NMR (Nuclear Magnetic Resonance) probes monitor the absolute value of the field.

3.2.3   The Central Tracking System

The Central Tracking System consists of SMD, TEC and ZCH. Due to the low magnetic field and the limited space inside the BGO a high spatial resolution is necessary to reconstruct tracks from charged particles with sufficient resolution. The central track detector was designed and constructed to:

- measure the polar and azimuthal angle of tracks

- measure the transverse momentum (P_T) and the charge of particles

- predict the impact points of charged particles in the BGO

- reconstruct the interaction point and secondary vertices

As part of the L3 upgrade the Silicon Microvertex Detector was constructed and installed in the experiment with the aim of improving the momentum and the impact parameter resolutions and the polar angle measurement.

The Silicon Microvertex Detector (SMD)

The SMD [35] consists of two layers of double sided silicon strip detectors providing both r-ϕ and z measurement from the outer and inner sides of each silicon sensor. The mean radial distance of the two layers to the beam axis is 62 mm and 78 mm respectively. The length of 30 cm yields a polar angle coverage of $22° \leq \theta \leq 158°$. Each layer consists of 12

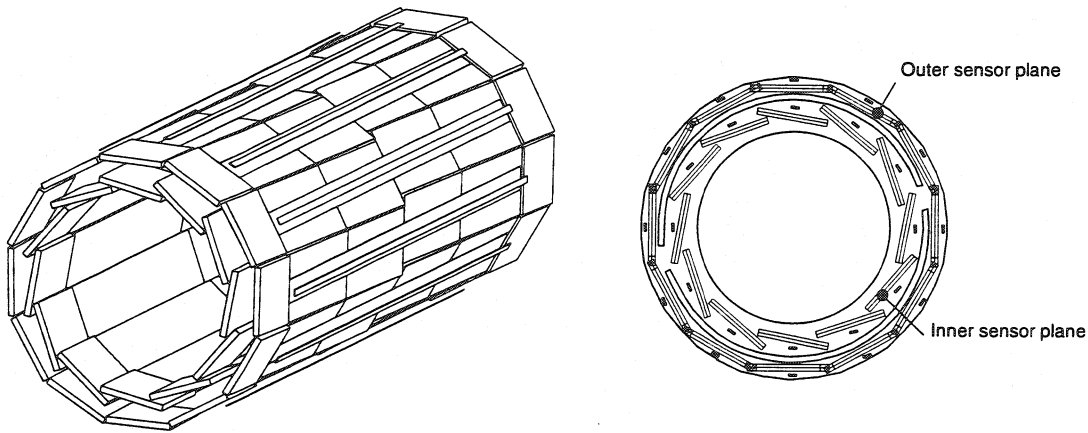Figure 3.3: A perspective view of the SMD (left) and a r-ϕ section (right). The inner sensors overlap region amounts to 10%. The outer layer is tilted.

modules. One module is subdivided into 4 silicon wafers. Adjacent inner layers have an overlap of 10%. The readout strips of the external modules are tilted by 2° with respect to the inner ones. Figure 3.3 illustrates the geometry of the SMD. The SMD provides additional high precision track points close to the primary vertex. A spatial resolution of 7.5 μm and 14.3 μm for the r-ϕ and z coordinates is obtained [36]. This improves the angular resolution of the tracking system as discussed in section 4.2.

The Time Expansion Chamber (TEC)

The total lever arm available for coordinate measurements in the central tracking detector is 31.7 cm radially. The charge identification of particles with a momentum of 45 GeV/c with 95% confidence level requires 50 coordinate measurements with 50 μm resolution. This basic requirement is fulfilled by a drift chamber operating in time expansion mode. The TEC [37] is split by grids into drift regions with homogeneous low electric field and amplification regions with high electric field. The electrons generated by an ionising particle drift with a constant velocity of approximately 6 μm/ns towards the amplification region, where gas amplification leads to avalanches at the anode wires. The wires are strung parallel to the z-axis, forming 12 inner and 24 outer sectors. The layout of one inner and two outer TEC sectors is illustrated in figure 3.4. The inner sectors contain 8 anodes while the outer sectors contain 54 anode wires. The TEC transverse momentum resolution is $\sigma_{P_T}/P_T = 0.0018 P_T$ (GeV/c).

The Z-Chamber (ZCH)

The Z-chamber [38, 39] supplements the measurements from TEC and SMD with a z-coordinate measurement in the angular range of $42° \leq \theta \leq 138°$ at r=50 cm. It consists of two cylindrical proportional wire chambers with cathode strip readout. Each wire
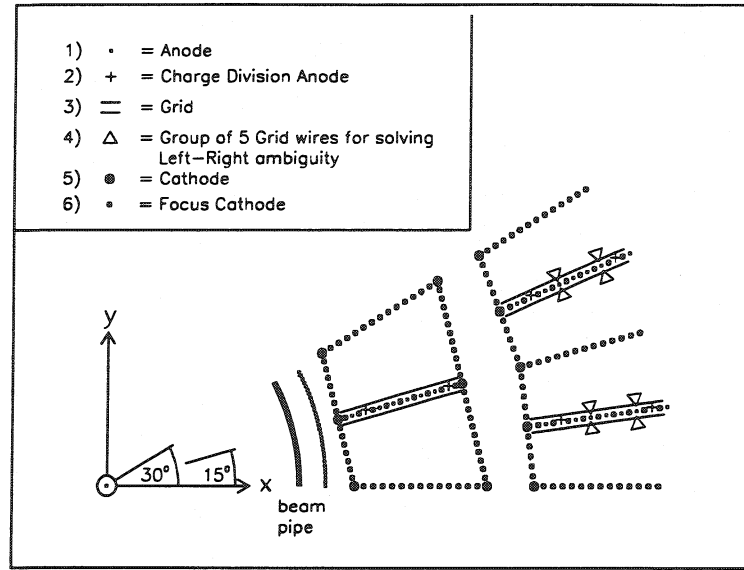
Figure 3.4: The Time Expansion Chamber. The structure of the inner and outer sectors is illustrated.

chamber contains two cathode layers. The 240 readout strips of one cathode layer in each chamber are oriented perpendicular to the chamber axis whereas the strips of the remaining layers form a helix with an angle of $\pm$ 69° to the axis (stereo layer). The 576 anode wires per chamber are strung in the axial direction. A particle traversing the Z-chamber generates an avalanche of electrons close to the wire. The avalanche induces image charges on both cathode layers. The measurement of the charge distribution allows to localise the avalanche position along the wire. The ϕ-component of the stereo layer measurement is used to match the z-information with the tracks measured in the TEC.

The single hit efficiency of each chamber is approximately 96%. The resolution varies between 200 μm and 800 μm going from the centre to the edges of the chamber.

3.2.4   The Electromagnetic Calorimeter

The electromagnetic calorimeter, shown in figure 3.5, was designed to measure the energies and positions of photons and electrons with high precision. The calorimeter surrounds the central tracking system and consists of 10734 bismuth germanate (BGO) crystals. The central part of the detector is made of two half barrels covering a polar angle range of 42° $\leq \theta \leq$ 138° containing in total 7680 crystals. This region is called the 'barrel region'. The polar angle coverage of the two endcaps each consisting of 1527 crystals is 11.6° $\leq \theta \leq$ 38° in the forward and 142° $\leq \theta \leq$ 168.4° in the backward direction. The inner radius at $\theta = 90°$ is 520 mm.

Each crystal of the calorimeter has the form of a truncated pyramid with a front face of 2 × 2 cm^2 and a rear face of 3 × 3 cm^2. Their length of about 24 cm corresponds
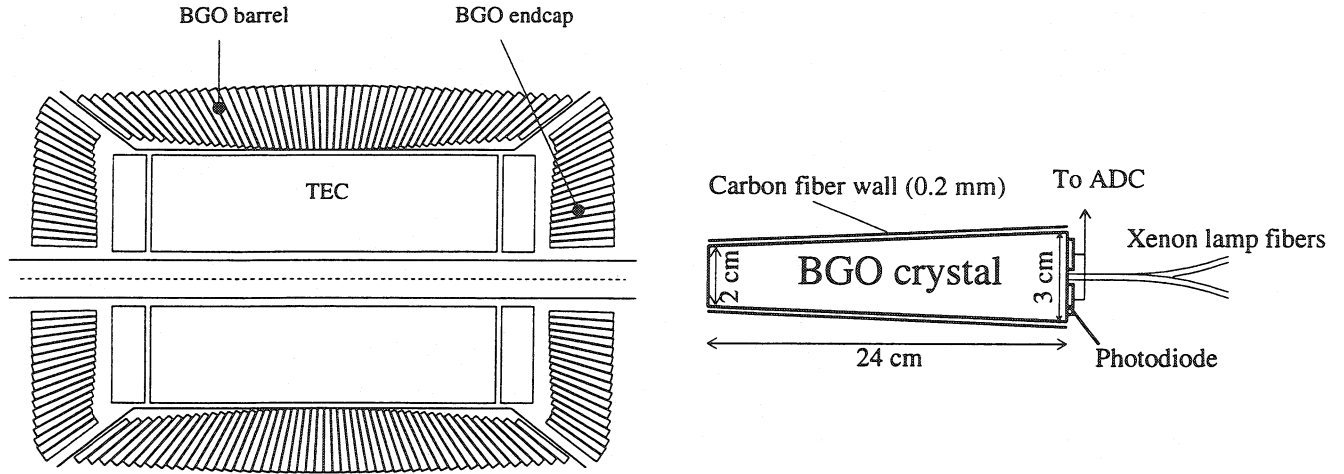
Figure 3.5: The electromagnetic calorimeter. All crystals are pointing to the nominal interaction vertex. The right picture illustrates the geometry of one crystal.

to approximately 22 radiation lengths and one nuclear interaction length. The BGO scintillation light is collected using 2 photodiodes glued on the rear face of each crystal. An angular offset of the order of 10 mrad of the crystals in ϕ with respect to the nominal interaction point is made to reduce energy leakage. The crystal acts both as the showering and the detection medium with an excellent energy resolution.

Three independent calibration methods ensure, independent of the test beam calibration, a continuous calibration and monitoring of the calorimeter. A Xenon flasher monitoring system measures the transparency of the crystals by the comparison of the detector response with a generated reference light pulse. In addition Bhabha scattering is used to calibrate the BGO to the precisely known beam energy. For the calibration at low energies data of minimum ionising cosmic muons are available.

The energy resolution is measured to be 5% at 100 MeV and less than 2% for energies larger than 1 GeV [40].

3.2.5 The Scintillation Counters

The scintillation counter system consists of 30 single plastic counters installed between the electromagnetic and hadronic calorimeters. The scintillators provide a trigger for hadronic events based on the hit multiplicity and serve to reject cosmic muons based on timing. For cosmic muons which pass near the interaction region the time-of-flight results in approximately 6 ns difference in time of opposite scintillator hits. For muons coming from $e^+e^- \rightarrow \mu^+\mu^-$ events there is no time difference. The scintillator timing resolution was measured to be better than 0.5 ns using $e^+e^- \rightarrow \mu^+\mu^-$ events.
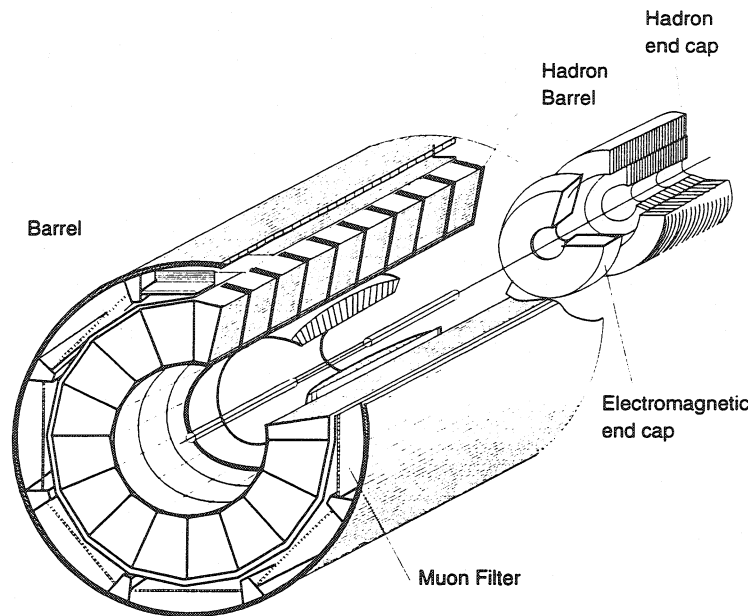
Figure 3.6: The hadron calorimeter.

3.2.6   The Hadron Calorimeter

The energy of hadrons emerging from e^+e^- collisions is determined by the total absorption technique with an electromagnetic and a hadron calorimeter. The hadron calorimeter is mechanically divided in three parts, the barrel covering the central region of $35° \leq \theta \leq 145°$, and the endcaps covering the polar angle range of $5.5° \leq \theta \leq 35°$ and $145° \leq \theta \leq 174.5°$ respectively. The calorimeter is made of depleted uranium absorber plates interspersed with proportional wire chambers. The amount of material traversed by a particle depends on the polar angle and varies between 6 and 7 nuclear absorption lengths. The barrel has a modular structure consisting of 9 rings of 16 modules each as shown in figure 3.6.

In addition a muon filter is mounted on the inside wall of the steel tube and adds one more absorption length to the HCAL. This combination ensures that only minimum ionising particles reach the muon spectrometer and suppresses the flow from secondary particles produced in the HCAL into the muon chambers.

The energy resolution of the HCAL for single pions was determined to be $(55/\sqrt{E} + 8)$ %. The fine segmentation of the calorimeters allows a measurement of the jet axis with a precision of approximately $2.5°$.

3.2.7   The Muon Spectrometer

The muon spectrometer was constructed to measure the momenta of muons with high resolution of $\sigma_p/p \approx 2.5\%$ at $p = 45$ GeV/c. As may be seen in figure 3.2, the spectrometer consists of two halves with a gap at $z = 0$. Each of this halves is subdivided
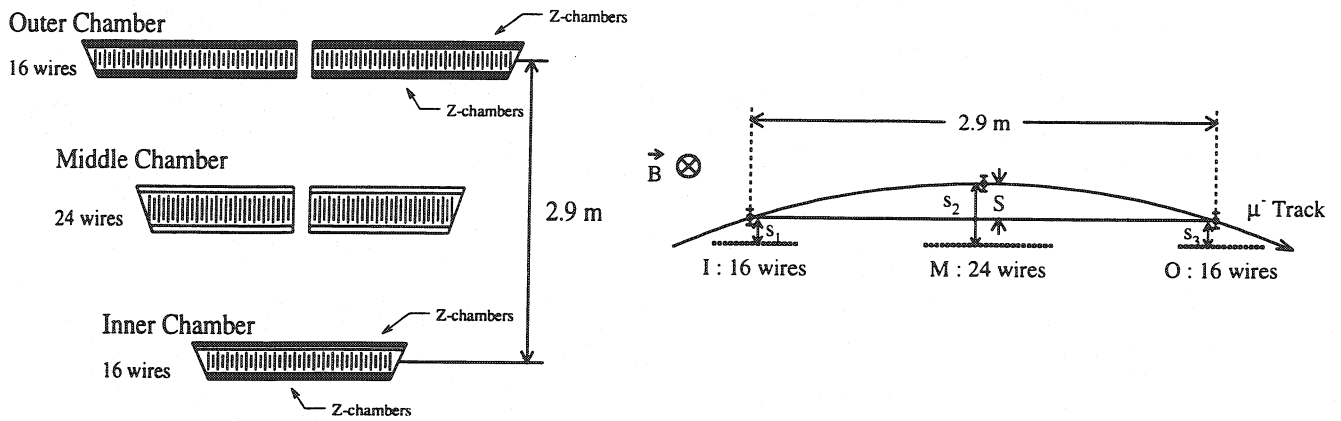
Figure 3.7: The left picture shows one muon spectrometer octant. The right figure illustrates the sagitta measurement using the P-chambers of the muon spectrometer. The lever arm inside the magnetic field is 2.9 m.

into octants. The muon spectrometer covers the polar angle range $35° \leq \theta \leq 145°$. As illustrated in figure 3.7 one octant contains five precision drift chambers (P-chambers) arranged in three layers. There are two chambers in the outer layer each with 16 signal wires, two chambers in the middle layer each with 24 signal wires, and one inner chamber containing 16 wires. A set of Z-chambers is mounted on the top and the bottom of the P-chambers of the inner and outer layer. The P and Z-chambers together yield a measurement of the momentum of the track.

The sagitta, which is typically 3.4 mm for particle momenta of 45 GeV, has to be measured with a precision of 70 μm to obtain the design resolution. The uncertainty of the sagitta measurement is dominated by three contributions:

- The uncertainty of the single wire resolution which is 54 μm.

- The contribution from Coulomb scattering which leads to a sagitta error of 30 μm at 45 GeV.

- The internal alignment between the chambers of one octant which is determined to be better than 30 μm.

Muons with an energy greater than 3 GeV are confined to a single octant. Therefore alignment is critical only between chambers of one octant.

3.2.8 The Luminosity Monitor

Bhabha scattering at low angles is used to determine the luminosity by comparing the measured rate with a precise theoretical calculation [41].

The luminosity monitor consists of two electromagnetic calorimeters and two sets of silicon trackers (SLUM). The calorimeters are segmented into 304 BGO crystals covering

the polar angle range of 24.93 mrad $\leq \theta \leq$ 69.94 mrad on each side of the interaction region. The energy resolution at 45 GeV is 1.3%, the angular resolution is 0.4 mrad in θ and 8.7 mrad in ϕ. Each crystal is read out by a photodiode. In addition, the crystals are equipped with a LED (Light Emitting Diode) to monitor the stability of the energy measurement.

3.2.9   The L3 Trigger System

An efficient trigger is needed to start the readout of the L3 subdetectors and to maximise the number of physically relevant events written to tape. In order to accomplish this goal, the L3 trigger has three levels. The first, the level-1, performs a logical OR of triggers from individual subdetectors. The level-2 coordinates information from more than one subdetector, while the level-3 does the same in more detail.

Level-1 Trigger   The level-1 trigger is based on five separate triggers. Each trigger starts operation at the beam crossing. If any of them has a positive decision the event is digitised and stored until the level-2 decision is available. The typical trigger rate of a level-1 trigger is 8 Hz. The five subdetector triggers are:

- **TEC trigger**: The TEC trigger selects events with two or more charged tracks.

- **energy trigger**: The energy trigger is designed to select events with a minimum energy deposition in the electromagnetic or hadronic calorimeter.

- **scintillator trigger**: The signals of scintillation counters are used to select high multiplicity events.

- **luminosity trigger**: The luminosity trigger requires energy in the luminosity monitor and selects Bhabha events.

- **muon trigger**: The muon trigger detects events with at least one reconstructed track in the muon spectrometer.

Level-2 Trigger   The level-2 trigger decision is based on the level-1 trigger informations. The coarse signals of the different subdetectors are combined and analysed. The main task is the rejection of background events, such as calorimetric noise, beam-gas events, beam-wall interactions and synchrotron radiation. Each event with more than one positive level-1 trigger is passed to the level-3 trigger. The level-2 trigger rate is typically 6 Hz.

Level-3 Trigger   The level-3 trigger decision is based on the full detector information for the event. The digitised data is used to define thresholds more precisely, perform a simplified pattern recognition for tracks, reconstruct energetic clusters and match energetic bumps in the calorimeters with tracks determined by the TEC. This leads to a further background suppression. Events with more than one positive level-1 trigger

result are always accepted as well as all luminosity triggers. The level-3 trigger does not introduce any additional dead time and enables the reduction of the event writing rate to 2-3 Hz.

3.3   Simulation and Reconstruction

Since high energy physics experiments are very complex, a detailed understanding of the detector response is necessary to translate measured quantities into physical results. The Monte Carlo technique is used to simulate the detector effects. First the physical process of interest is simulated by an event generator which creates the particle four momenta. In a second step the detector response for these events is modelled.

The generated particles are propagated through a detailed representation of the L3 detector taking into account the magnetic field and the interactions of each particle with the detector elements, e.g. multiple scattering, energy loss or shower development in the calorimeter. Within this step the signals of the subdetectors are simulated. Furthermore the imperfections are introduced, e.g. inefficiencies, energy resolutions, gaps, electronic noise or broken read out components, where the detector performance for a certain data taking period is taken into account.

The simulation software is based on the program GEANT [42]. The response, along with additional information from the generator, is stored in the same format as data.

The Monte Carlo generators KORALB [43] and KORALZ [44] are used to generate events of the process $e^+e^- \rightarrow \tau^+\tau^-$ including radiative corrections. The subsequent decay of the τ is simulated by the TAUOLA program [45].

The generator KORALB was developed to generate τ pairs in the energy range up to 30 GeV. An updated version contains the Z exchange and the full spin correlations [46], but at centre of mass energies in the Z mass range only the Born level matrix element can be used.

The generator KORALZ was developed to generate τ pairs around the Z resonance. It contains higher order radiative corrections but treats only the longitudinal spin components.

The event reconstruction is identical for Monte Carlo and data. The information is read and decoded. A pattern recognition is applied in order to extract measured quantities, such as tracks or energy depositions in the calorimeters. Finally associations are made between the reconstructed objects to produce the kinematic variables that characterise the event.

Chapter 4

Tracking within L3

Since the spin analysis is based on the angular measurements of the final state particles the performance of the L3 tracking has been studied. The algorithm to assign SMD hits to tracks measured by the TEC, the angular resolution and the SMD efficiency are presented in detail. The tracking system is shown in figure 4.1.

4.1 Track Reconstruction

All tracks are reconstructed in two steps. First only the information of the TEC is used to define a track in the r-ϕ plane where the hits in the TEC are defined by the space points, which are computed from the position of the anode wires and the measured drift times. Then the hits of the SMD and the ZCH are assigned to the TEC tracks. A new fit is performed to determine the tracking parameter in the r-ϕ and the s-z plane with higher accuracy.

The hits associated to a track are fitted by a circle in order to extract the following track parameters in the r-ϕ plane.

- the curvature $\mathcal{C}$ of the track, which is proportional to $1/P_T$

- the distance of closest approach to the reference point (DCA)

- the azimuthal angle ϕ within the bending plane

These parameters are illustrated in figure 4.2. The reference point is the centre of the beam spot and is defined with respect to the L3 coordinate system analysing a sample of Bhabha events. The beam widths in x and y are:

$$\sigma_x \approx 120 \ \mu\text{m} \qquad \sigma_y \approx 15 \ \mu\text{m} \tag{4.1}$$

The charge of the particle is given by the sign of the track curvature. The ϕ prediction of the track together with the curvature is used to match the clusters in the ZCH to the TEC tracks. For this procedure the ϕ component of the stereo layers of the ZCH is needed. Without SMD the polar angle was determined by fitting a straight line assuming the
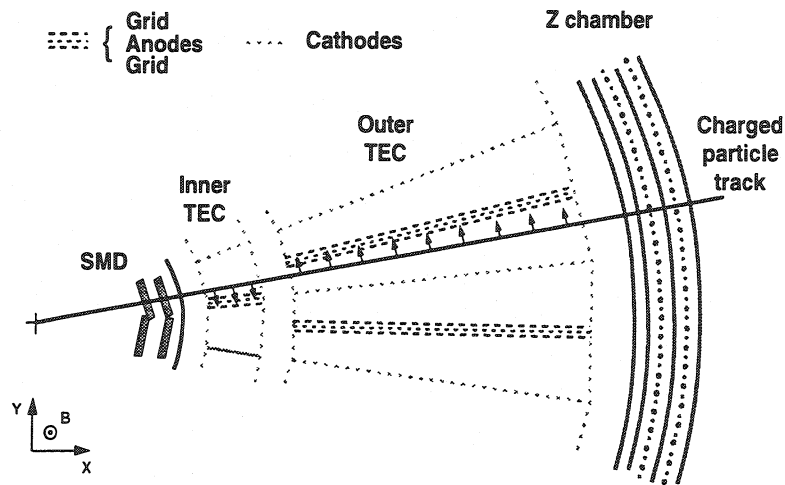
Figure 4.1: The L3 tracking system.

particle came from the fill vertex in z [47]. The polar angular resolution was dominated by the beam width in z which is typically of the order of 1 cm. The installation of the SMD in 1993, which became fully operational in 1994, provides each track with up to 6 additional space points. Since hits close to the event vertex are available, a two parameter fit is performed in order to extract the slope and the intercept of the track in the s-z plane.

The algorithm to select hit candidates out of all charged clusters in the SMD works as follows.

1. The TEC track is extrapolated to the SMD in the r-ϕ plane. All clusters within 3.5 σ are kept as matched hit candidates.

2. The readout strips of the inner r-ϕ layer are parallel to the TEC wires. The accuracy for the prediction for the inner r-ϕ layer is better than 100 μm. The closest cluster is assigned to the track. An refit including the closest cluster is performed in order to improve the tracking parameters.

3. These tracks are extrapolated to the outer r-ϕ layer in order to match outer r-ϕ *and* z clusters. The prediction for an outer r-ϕ cluster has an accuracy of 30 μm if an inner r-ϕ cluster was assigned to the track and the refit performed or 70 μm if not. Due to the tilt of 2° of the outer SMD layer the hits contain information about the r-ϕ and z coordinate. Using the tilt the prediction for the outer r-ϕ layer is extrapolated to the outer z layer with an precision of 1 mm if an refit was performed or 2 mm if not. This procedure is called stereo matching. All clusters which are located more than 3.5 σ from the prediction are rejected.

4. Once the SMD z-hit candidates are found a vertex constraint is applied in order to
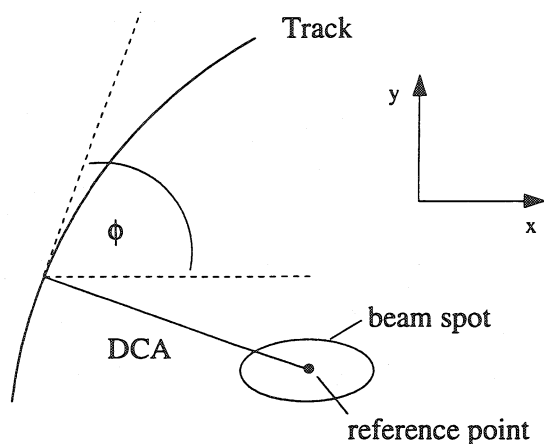
Figure 4.2: The tracking parameter in the r-ϕ plane.
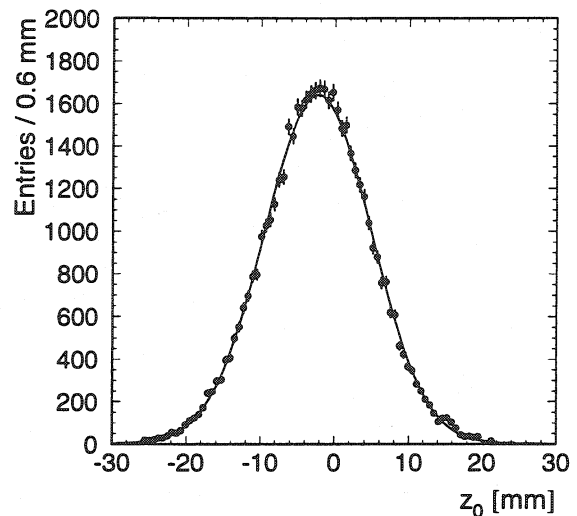
Figure 4.3: The intercept distribution for selected Bhabha events in 1994. The distribution is fitted with a Gaussian. The average fill vertex in 1994 is displaced with respect to the L3 coordinate system by -2.3 mm. The beam width is 7.2 mm.

assign a SMD z-hit to the track. The requirement that all tracks of the event should come from the same vertex within a window of 5 mm suppresses the assignment of noisy clusters.

Finally a fit based on all assigned hits defines the track parameters. The s-z fit provides the θ value and the intercept z_0 of the track with the beam axis. The intercept distribution is shown in figure 4.3.

4.2   The Angular Resolution

The angular resolution of the L3 tracking system was measured using a data sample of 23766 $e^+e^- \rightarrow \mu^+\mu^-$ and 29091 $e^+e^- \rightarrow e^+e^-$ events. The results for both data samples are consistent, hence the combined results are presented.

The physical feature that $e^+e^- \rightarrow \mu^+\mu^-$ and $e^+e^- \rightarrow e^+e^-$ events have almost ideal back-to-back topology is used to determine the resolution of the tracking system. The deviation from the back-to-back topology provides a good measure for the resolution. There are not only detector effects which causes a deviation from an exact back-to-back topology. One has also to take in consideration initial and final state radiation. The following cuts are applied to suppress events containing radiative photons. For $e^+e^- \rightarrow \mu^+\mu^-$ events an energy greater than 84 GeV measured in the muon chambers is required. For the $e^+e^- \rightarrow e^+e^-$ channel the energy in the BGO assigned to the tracks has to be

greater than 84 GeV. It is required that exactly two tracks are observed in the detector. Furthermore uncertainties in the TEC calibration, alignment and the matching algorithm will affect the track reconstruction and are contained in this resolution study.

The resolution in the azimuthal angle ϕ

Given the periodical structure of the TEC it is appropriate to consider the ϕ resolution as a function of ϕ_{loc} which is defined as $\phi_{loc} = mod\ (\phi, 2\pi/12)$. With respect to one inner sector of the TEC ϕ_{loc} covers the range from $0 \leq \phi_{loc} \leq 0.52$ rad. Therefore the results presented here are an average over the local features of 12 inner TEC sectors. The difference of the ϕ angles of both tracks was calculated for 30 bins in ϕ_{loc} and fitted with a Gaussian. The resolution for the ϕ angle as a function of ϕ_{loc} is presented in figure 4.4. The periodic structure in the distribution reflect the internal structure of the TEC sectors. The centred peak corresponds to the inner anode plane, whereas the other peaks are related to the outer anode planes. The average resolution in the central region is approximately 0.4 mrad.

The resolution in the polar angle θ

The resolution is studied in the region which covers an angular range of $|\cos\theta| < 0.74$. The difference of the θ angles of the two tracks was calculated for 10 bins in θ. The distribution was fitted by a Gaussian. The resolution as a function of θ is presented in figure 4.4. The average resolution is 1.7 mrad and can be considered as constant in the central region. Due to the usage of the SMD the resolution is improved with respect to data from earlier years by one order of magnitude. Since the Monte Carlo resolution is not in agreement with data a correction was applied.

The Correction

The deviations between Monte Carlo and data are at the 0.1 mrad level for the ϕ resolution while the resolution for the polar angle differs by a factor of 2.5. The single hit resolution which is used to simulate the SMD clusters has been taken from test beam data. These values differ from those in the current experimental setup. Furthermore the resolution parameters of the z-chamber which are implemented in the Monte Carlo are overestimated and responsible for the disagreement. In order to correct the resolution the following correction factor was calculated bin by bin:

$$\sigma_{cor} = \sqrt{\sigma_{Data}^2 - \sigma_{MC}^2} \qquad (4.2)$$

where $\sigma_{Data,MC}$ corresponds to the width of the Gaussian distributions in data and Monte Carlo. The precision of the angular measurement depends also on the number of SMD hits which are associated to the tracks (up to three for the circle and the s-z fit). Therefore the resolution study was performed for all possible SMD hit assignments independently. Finally, the correction factors have been applied corresponding to the SMD hit assignment.
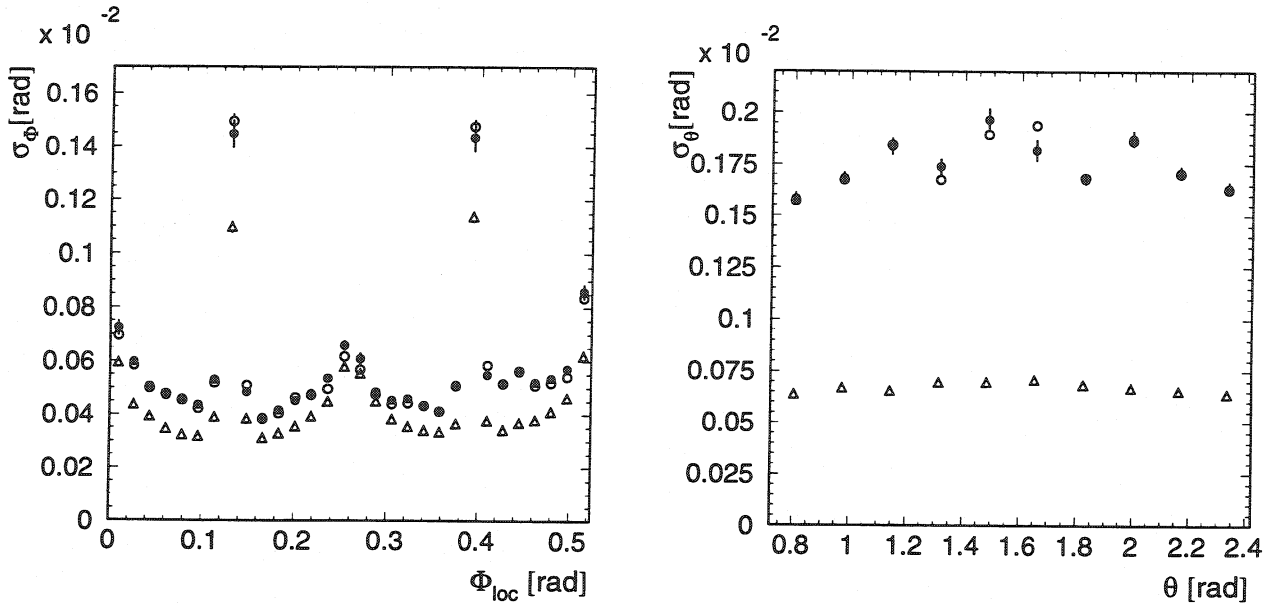
Figure 4.4: The angular resolution of the L3 tracking system. The solid dots are data. The triangles correspond to the Monte Carlo when no correction is applied. The open dots represent the Monte Carlo after the correction as described in the text. The left figure shows the ϕ resolution. The right picture shows the θ resolution when at least one SMD z-hit is assigned to each track. The open dots are sometimes hidden by the solid ones. The resolution given here is an average over all possible SMD hit assignments.

4.3 The SMD Efficiency

To study the SMD efficiency the number of tracks with an associated SMD hit is compared to the number of tracks measured by the TEC.

$$\epsilon = \frac{\text{Number of tracks with SMD hit}}{\text{Number of TEC tracks}} \tag{4.3}$$

A dilepton sample was used to determine the efficiency. The low track multiplicity of such events avoids problems with ambiguous hit assignments and corresponds to the $\tau\tau$ final state topology. Since the efficiency is calculated by the ratio after the hit finding and matching algorithm, correlations between the physical independent SMD layers occur. The efficiencies of all four SMD layers as a function of the angles θ and ϕ are shown in figures 4.5 and 4.6. As can be seen the efficiency is angular dependent. The Monte Carlo describes these dependencies, because broken or inefficient readout channels are taken into account in the simulation. The observed deviations are of the order of 2%. The requirement that each track has at least one assigned SMD z-hit reduces the number of events to 74% of the total data sample.
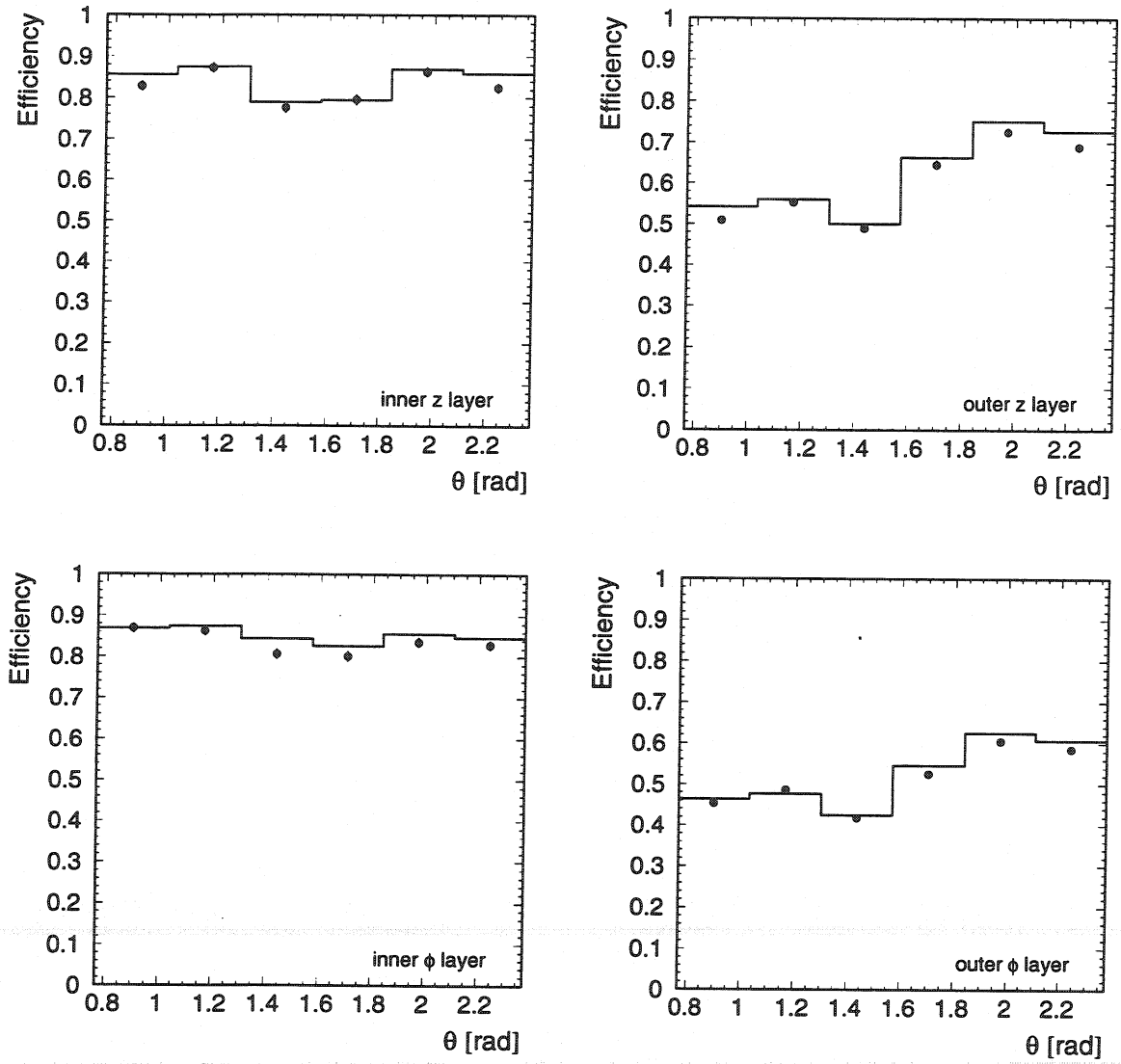
Figure 4.5: The SMD efficiency as a function of θ. The dots correspond to data and the histograms to the Monte Carlo distributions.
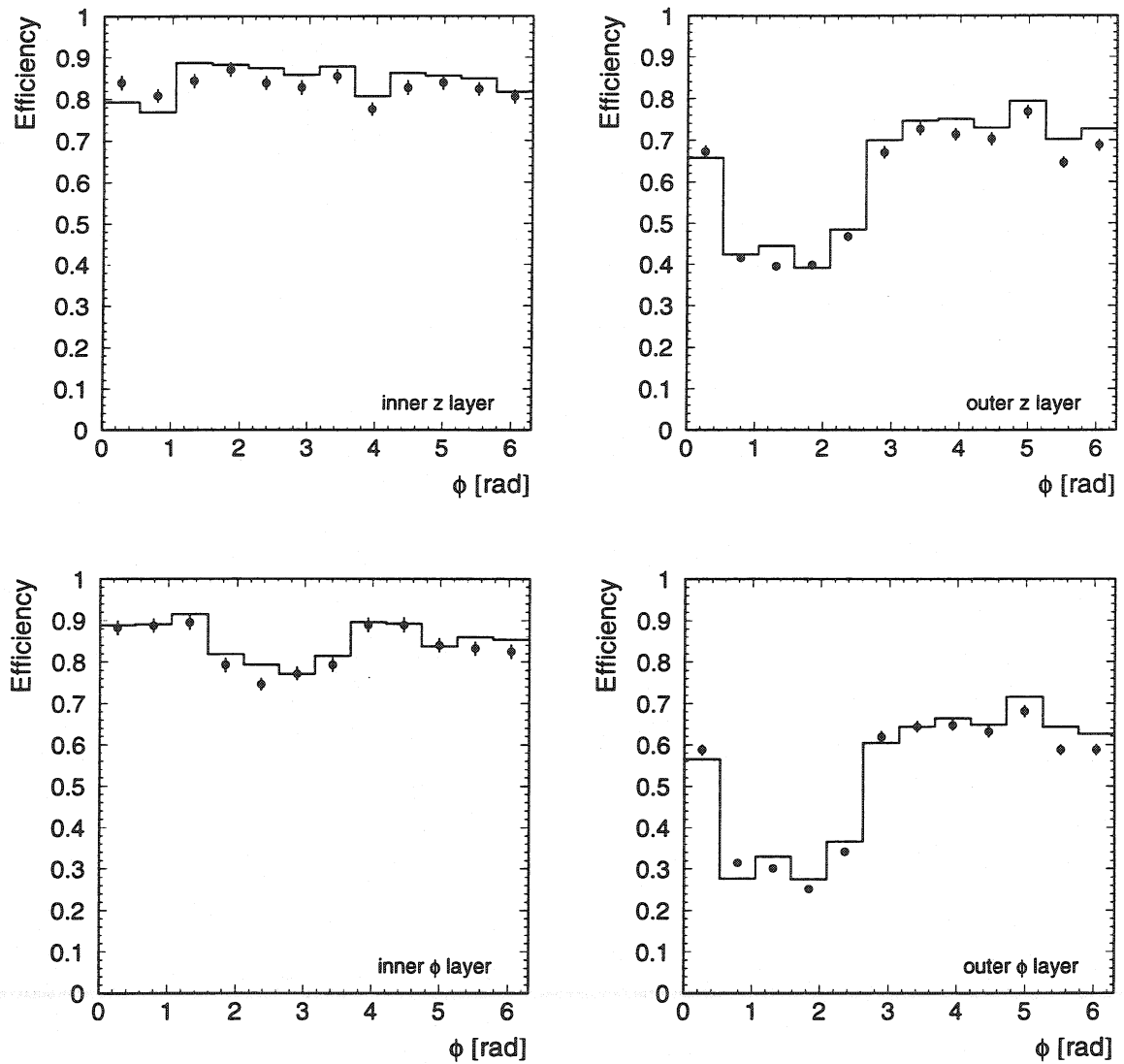
Figure 4.6: The SMD efficiency as a function of ϕ. The dots correspond to data and the histograms to the Monte Carlo distributions. The reduced efficiency of the outer ϕ layer in some particular bins is due to two disconnected silicon wafers. The step (3) of the matching algorithm produces a similar efficiency gap for the outer z layer although this layer is fully operational.

Chapter 5

The Experimental Methods

In this chapter the experimental methods used to measure the τ polarisation and the spin correlations are described.

5.1 The Method to Measure $\mathcal{A}_e$ and $\mathcal{A}_\tau$

The determination of the τ polarisation requires experimental access to the helicity state of the τ. Due to its short lifetime the τ is not directly observed and its neutrino remains undetected. The τ decay products can be used to measure the polarisation. Assuming pure (V-A) structure of the charged current, figure 5.1 shows the $\tau \to \pi\nu$ decay for the two different helicity states in the τ restframe. The ν_τ is left-handed and the charged pion has spin 0. Due to angular momentum conservation the charged pion is predominantly emitted in the direction of the spin of the τ. The observed pions in the laboratory system tend to have lower energy in the case of a left-handed τ decay and higher energy in case of a right-handed one. Thus the energy distributions of τ decay products carry information about the τ helicity states.

It is important to keep in mind that $\mathcal{P}_\tau$ is defined in terms of the neutral current couplings. However, since the τ decay spectra are analysed, the polarisation measurement depends also on the charged current couplings of the τ to the W. Therefore one measures in fact $\xi \mathcal{P}_\tau$ where ξ is the average ν_τ helicity:

$$\xi = -\frac{2\,g_v\,g_a}{g_v^2 + g_a^2} \tag{5.1}$$

In this analysis the pure V-A structure ($g_v = g_a = 1$) of the charged current is assumed, consistent with current experimental results $g_v = 1.00 \pm 0.09$ and $g_a = 1.00 \pm 0.09$ [48]. The average neutrino helicity becomes $\xi = -1$ and the quantity measured by the analysis of the τ decay spectra is $\mathcal{P}_\tau$.

The energy spectra of the τ decay products are polarisation sensitive. It is convenient to introduce the normalised energy x of the charged decay product p, $x_p = E_p/E_\tau$. The parametrisation of the energy distribution, $h(x)$, depends on the decay channel [11, 49].
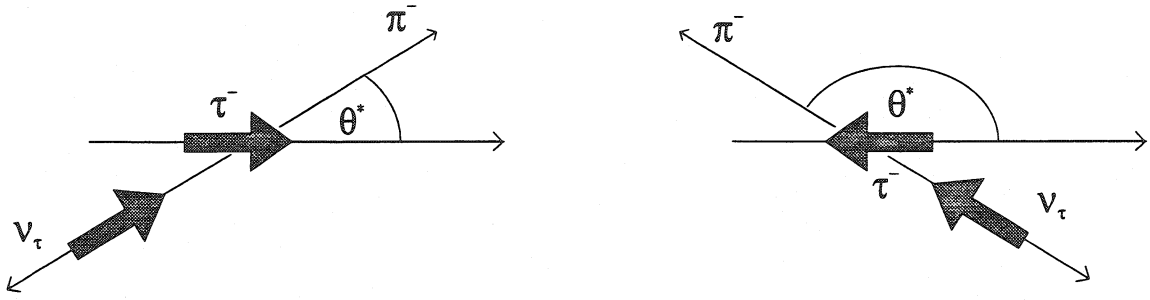
Figure 5.1: The helicity configurations for the $\tau \to \pi\nu$ decay. The thick arrow indicates the longitudinal spin component of the particle. The thin line defines the direction of flight. The angle θ^* in the τ restframe is related to the pion energy in the laboratory frame $\cos\theta^* \approx (2x - 1)$.

1. purely leptonic decays $\tau \to l\nu\bar{\nu}$ with $l = e, \mu$

$$h(x) = 1/3 \left[(5 - 9x^2 + 4x^3) + \mathcal{P}_\tau \left(1 - 9x^2 + 8x^3 \right) \right] \tag{5.2}$$

2. two body semileptonic decays $\tau \to h\nu$ with $h = \pi, K, \rho, K^*, a_1$

$$h(x) = 1 + \mathcal{P}_\tau \, \alpha_h \, (2x - 1) \tag{5.3}$$

where α_h is the polarisation analyser which depends on the mass and spin of the hadronic decay product h. In the case of spin 0 particles α_h is equal to 1, whereas for spin 1 particles the sensitivity of the energy spectra to the polarisation is reduced by:

$$\alpha_h = \frac{m_\tau^2 - 2m_h^2}{m_\tau^2 + 2m_h^2} \tag{5.4}$$

The factor α_h reflects the fact that in the spin 1 hadronic final state two different spin states of the hadron are allowed. One finds $\alpha_\rho \approx 0.46$ and $\alpha_{a_1} \approx 0.12$. As can be seen from (5.2) and (5.3) the structure of the decay spectra has the form $h(x) = f(x) + \mathcal{P}_\tau g(x)$. In order to recover the sensitivity loss due to α_h it was proposed to analyse also the angular distribution of the decay of the spin 1 particle [50] or to introduce an optimal polarisation sensitive variable [51], which coincides with the normalised particle energy for the purely leptonic decay and the spin 0 hadronic decay mode. The reduction in sensitivity due to the two neutrinos in the purely leptonic decays cannot be recovered.

In addition to the energy spectra the acolinearity of the decay products is polarisation sensitive [10]. The acolinearity, ϵ, between two tracks with angles (ϕ_1, θ_1) and (ϕ_2, θ_2) is defined as

$$\epsilon = \pi - \theta_{12} \tag{5.5}$$
$$\cos\theta_{12} = \sin\theta_1 \sin\theta_2 \cos(\phi_1 - \phi_2) + \cos\theta_1 \cos\theta_2 \tag{5.6}$$
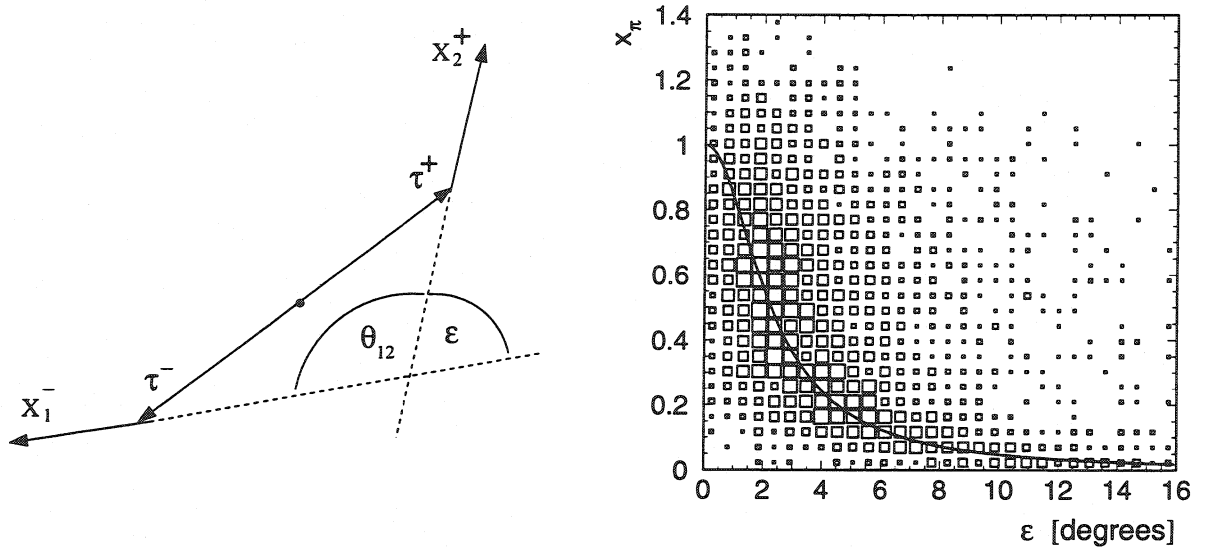
Figure 5.2: The left figure illustrates the definition of the acolinearity angle. The right picture shows the correlation between the normalised pion energy and the acolinearity angle for all selected final states πX using 1994 data. The selection criteria are described in section 6.1.3. The solid line represents the analytical relation between the two variables as mentioned in the text. The analytical function is not corrected for detector and radiative effects. The correlation was calculated to $\rho = -0.64$.

where θ_{12} is the opening angle between the decay products as shown in figure 5.2. The acolinearity angle is a measure of the deviation from the back-to-back topology. The correlation between the pion energy and the acolinearity for all selected πX final states is shown in figure 5.2. The selection criteria are described in section 6.1.3.

From the following consideration the acolinearity can be interpreted as the average angle between the τ and its decay product:

- assuming a back-to-back τ pair with the decay $\tau^- \tau^+ \to X_1^- X_2^+ \nu\,'s$

- the angles of the decay products $\tilde{\theta}_1$ and $\tilde{\theta}_2$ are defined with respect to the τ direction of flight

- taking the average about all possible angles $\tilde{\theta}_2$ for a fixed angle $\tilde{\theta}_1$ yields $< \tilde{\theta}_2 > = 0$. The average direction of the track (X_2^+) coincides with the τ^+ direction.

- under the assumption of the back-to-back topology one finds $< \epsilon > = \tilde{\theta}_1$

The relation between the angle and the energy of the particle can be expressed by:

$$< \epsilon\,(x) > = \arctan\left[\frac{(\,1 - (2x-1)^2\,)^{1/2}}{\gamma\,(\,(2x-1) + \beta\,)} \right] \tag{5.7}$$
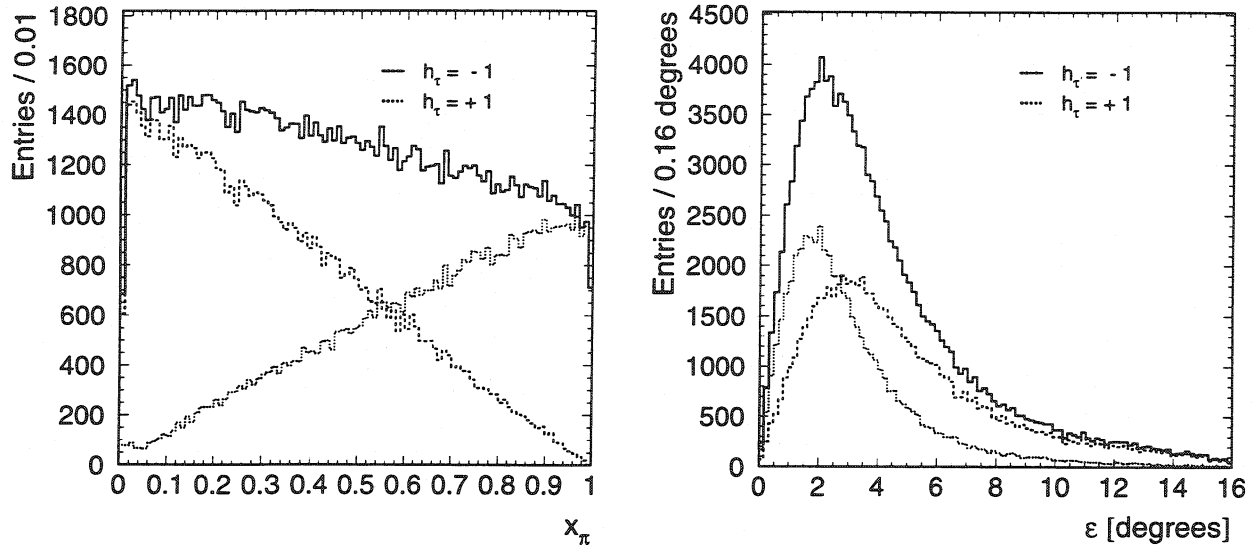
Figure 5.3: The left figure shows the energy spectra for the $\tau \rightarrow \pi\nu$ decay. In addition the contributions of the different helicity states are presented. The right picture shows the acolinearity distributions for the same Monte Carlo sample. The Monte Carlo distributions are not corrected for resolution and acceptance effects.

with the factors $\gamma = E_{beam}/m_\tau$ and $\beta = \sqrt{1 - 1/\gamma^2}$. This analytical function is shown in figure 5.2.

The following procedure is applied to measure the τ polarisation:

1. A data sample of $\tau\tau \rightarrow \pi X$ final states is selected where X is any one-prong τ decay.

2. The same selection is applied to a Monte Carlo sample where all detector effects are included. On Monte Carlo level the helicity state of each τ is known, so the distribution is divided in two samples, one with $h_\tau = +1$ and the other with $h_\tau = -1$.

3. Finally the data distribution is fitted with a linear combination of the Monte Carlo distributions. The relative weight of the fitted spectra corresponds to the polarisation realised in data.

The sensitivity to determine the τ polarisation depends on the τ decay channel and the polarisation sensitive variable in which the fit is performed. As can be seen from figure 5.3, the shape of the energy spectrum is more sensitive to the polarisation than the shape of the acolinearity spectrum. But the determination of the acolinearity relies on the measurement of the angles of the τ decay products and hence has different sources of systematic errors than the energy method.
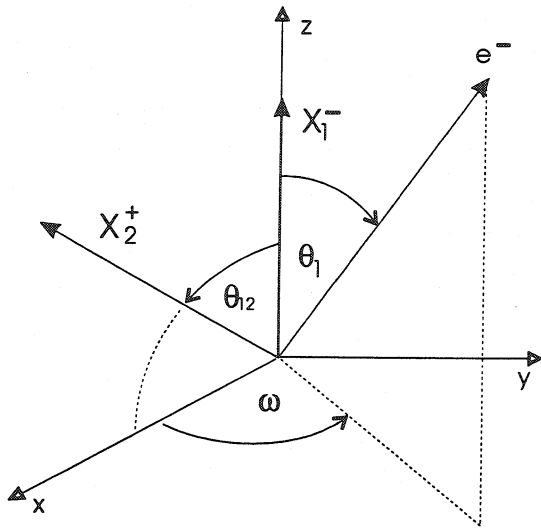
Figure 5.4: The coordinate system used in order to describe spin correlations in terms of experimentally measured quantities. To analyse the spin correlations it is not necessary to reconstruct the τ direction.
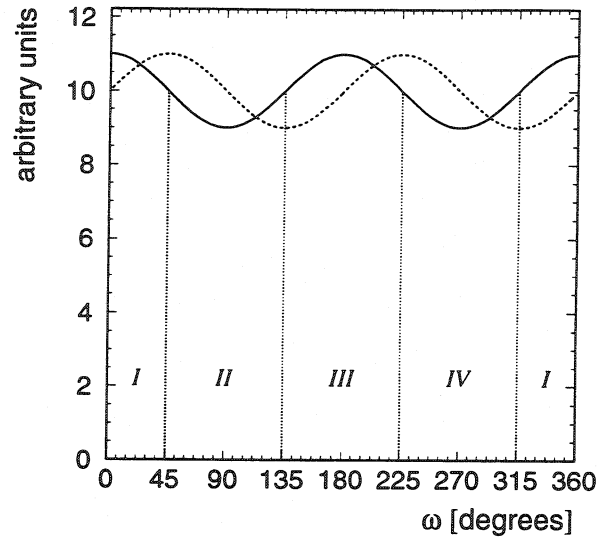
Figure 5.5: The cross section (arbitrary units) as a function of ω for two different scenarios. The solid line represents the Standard Model prediction ($D_2 = 0$) and the dashed line the orthogonal case ($C_2 = 0$). The sectors indicated by Roman numbers are used to define A_c.

5.2   The Method to Measure Spin Correlations

The large luminosity delivered to LEP experiments, the low background rates in τ pair production and the high resolution tracking devices, allow to measure the spin correlations at LEP. A first feasibility study was performed in [52]. Within this section the experimental method is described following the idea of [53].

In order to measure the spin correlations one has to define an observable which is sensitive to the constants C_2, D_2 or equivalent to the normalised correlations A_{TT} and A_{TN} as defined in equation (1.70). As already known from the measurement of the τ polarisation the spin vectors of the τ are not directly measurable, but the τ decay products carry information about the spin of the τ. This fact can be used as well if transverse and normal spin components are considered. The spin correlations are translated into angular correlations of the charged τ decay products X_1^- and X_2^+. For further discussions it is convenient to define the coordinate system as shown in figure 5.4. The momentum of the charged decay product X_1^- defines the z-axis. The z-axis together with the momentum of the second decay product X_2^+ defines the x-z half plane. The y-axis is perpendicular to the x-z plane. Within this coordinate system the electron beam e$^-$ has the polar angle θ_1 and the azimuthal angle ω. The coordinate system is well defined if an acolinearity different from zero is required.
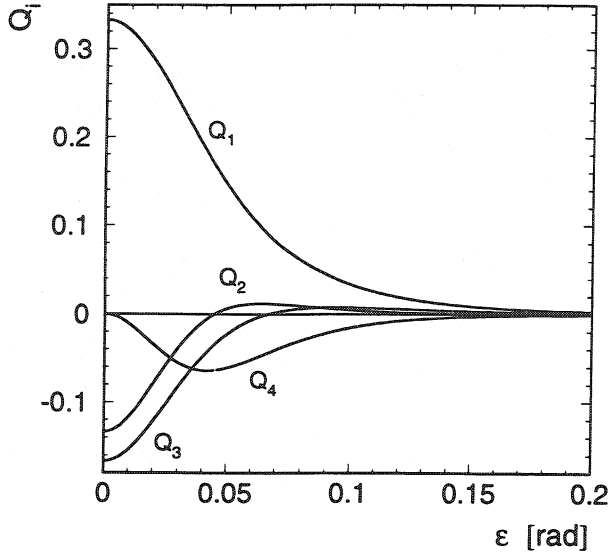
Figure 5.6: The figure shows the Q_i-functions as a function of the acolinearity from the analytical calculation in [53]. The masses of the τ decay products are neglected with respect to the τ mass. The introduction of the final state masses will change the shape of the Q_i-functions.
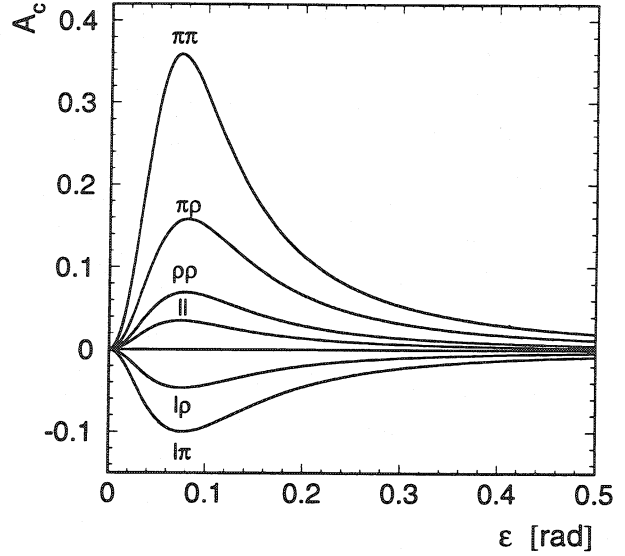
Figure 5.7: The asymmetry $A_c(\pi/2, \epsilon)$ as a function of the acolinearity in the vanishing mass approximation. The Q_i-functions from Appendix A, equation (5.12) and the Standard Model couplings are used to calculate A_c.

Considering the τ decays into a single charged particle plus missing neutrinos, the cross section for the process $e^+e^- \rightarrow \tau^+\tau^- \rightarrow X_1^- X_2^+ \nu's$ can be written as a function of the polar angle θ_1, the acolinearity ϵ and the aplanarity angle ω where the index i, j specify the τ decay channels [12].

$$\frac{d\sigma^{ij}}{d\epsilon \, d\cos\theta_1 \, d\omega} = K^{ij}(s)\left(R_0^{ij}(\epsilon)(1 + \cos^2\theta_1) + R_1^{ij}(\epsilon)2\cos\theta_1 + R_2^{ij}(\epsilon,\omega)\sin^2\theta_1\right) \quad (5.8)$$

with:

$$K^{ij}(s) = \frac{|P(s)|^2}{4s}Br(\tau \rightarrow X_i...)Br(\tau \rightarrow X_j...) \quad (5.9)$$

$$R_n^{ij}(\epsilon) = C_n\left(Q_1(\epsilon) + \alpha_i\alpha_j Q_2(\epsilon)\right) + D_n(\alpha_i - \alpha_j)Q_3(\epsilon) \quad n = 0,1 \quad (5.10)$$

$$R_2^{ij}(\epsilon,\omega) = \alpha_i\alpha_j(C_2\cos(2\omega) + D_2\sin(2\omega))Q_4(\epsilon) \quad (5.11)$$

From a comparison with equation (1.48) it can be seen that the angular dependence in the angle θ_1 has the same structure as in the angle θ which was defined as the τ^- scattering angle with respect to the electron beam.

The cross section consists essentially of two parts if the dependence on the polar angle θ_1 and the acolinearity ϵ is integrated out. There is a constant term independent of ω (equation (5.10)) and one contribution with the trigonometric functions $\sin(2\omega)$ and $\cos(2\omega)$ (equation (5.11)). The amplitudes contain the combined neutral current couplings C_2 and D_2. These terms define the shape of the cross section as a function of ω as illustrated in figure 5.5.

The spin correlations associated with C_2 and D_2 are accessible using two planar asymmetries A_c and A_s. The asymmetries are constructed in the angle ω, which is enclosed by the planes (X_1^-, X_2^+) and (X_1^-, e^-).

$$A_c(\theta_1, \epsilon) \equiv \frac{\int_{\cos 2\omega > 0} d\sigma - \int_{\cos 2\omega < 0} d\sigma}{\int_{\cos 2\omega > 0} d\sigma + \int_{\cos 2\omega < 0} d\sigma}$$

$$= \frac{2\,\alpha_i \alpha_j\, Q_4(\epsilon) \sin^2 \theta_1\, C_2}{\pi\, [R_0(\epsilon)\,(1 + \cos^2 \theta_1) + R_1(\epsilon)\, 2\cos\theta_1]} \qquad (5.12)$$

$$A_s(\theta_1, \epsilon) \equiv \frac{\int_{\sin 2\omega > 0} d\sigma - \int_{\sin 2\omega < 0} d\sigma}{\int_{\sin 2\omega > 0} d\sigma + \int_{\sin 2\omega < 0} d\sigma}$$

$$= \frac{2\,\alpha_i \alpha_j\, Q_4(\epsilon) \sin^2 \theta_1\, D_2}{\pi\, [R_0(\epsilon)\,(1 + \cos^2 \theta_1) + R_1(\epsilon)\, 2\cos\theta_1]} \qquad (5.13)$$

The observables A_c and A_s are proportional to C_2 and D_2 respectively. In addition they depend on the polarisation analyser α_i and the functions $Q_i(\epsilon)$. The functions $Q_i(\epsilon)$ are shown in figure 5.6. The explicit representation can be found in Appendix A. The factors α_i are given by:

- $\alpha_{l\pm} = \pm\, 1/3$

- $\alpha_{\pi\pm} = \mp\, 1.0$

- $\alpha_{\rho\pm} = \mp\, 0.46$

The sensitivity to spin correlations in (5.12) and (5.13) is reduced by the product $\alpha_i \alpha_j Q_4$. The values are listed in table 5.1. The fact that the sign of the polarisation analyser for leptonic τ decays is opposite to the sign for semileptonic decays leads to negative values for the observable A_c in the case of lepton–hadron final states. The asymmetry A_c has to be measured for all exclusive final states independently in order to avoid cancellations due to the different signs. The asymmetry A_c is shown in figure 5.7. The values for the asymmetry A_s are at the 10^{-3} to 10^{-4} level.

To summarise: Apart from the asymmetries (1.52) – (1.54) two more observables exist which depend on the spin correlations. A coordinate system was defined, where the angle ω can be computed from the measured particle momenta. Within this coordinate system the electron beam has a preferred direction leading to two planar asymmetries. The calculation of the angle ω is independent of the τ direction. The coordinate system is only defined if a minimal acolinearity is required.

Channel	$\alpha_i \alpha_j \ \text{sign}(Q_4)$
$l^{\pm} \ l^{\mp}$	0.11
$l^{\pm} \pi^{\mp}$	-0.33
$l^{\pm} \rho^{\mp}$	-0.15
$\pi^{\pm} \pi^{\mp}$	1.00
$\pi^{\pm} \rho^{\mp}$	0.46
$\rho^{\pm} \rho^{\mp}$	0.21

Table 5.1: The sensitivity to transverse spin correlations for several τ pair decay channels.

The effect of the masses of the τ decay products

The observables A_c and A_s so far were constructed in the vanishing final mass approximation, i.e. the masses of the τ decay products are neglected with respect to the mass of the τ lepton. The equations (5.12) and (5.13) contain the function $Q_4(\epsilon)$ which is in this approximation independent of the τ decay modes. The different decay modes are taken into account due to different factors α_i.

Since the ratio of the masses is not small, e.g. $m_\rho/m_\tau = 0.4$, the influence of the finite particle masses to the spin correlations was studied [54]. It was shown that the effect is not negligible and will modify the results. The functional expression of equation (5.8) can be kept, because the mass affects only the acolinearity angle. The mass dependent Q_i-functions were computed using the TAUOLA Monte Carlo [45] and are shown in Appendix B. To simplify it is convenient to redefine the Q_i-functions as follows:

$$
\begin{aligned}
\hat{Q}_1 &= Q_1 + \alpha_k \alpha_l \ Q_2 \\
\hat{Q}_2 &= (\ \alpha_k - \alpha_l \ ) \ Q_3 \\
\hat{Q}_3 &= \alpha_k \alpha_l \ Q_4
\end{aligned}
$$

In fact the cross section depends only on these linear combinations where the masses and the polarisation analysers are included. These functions are used for all following considerations.
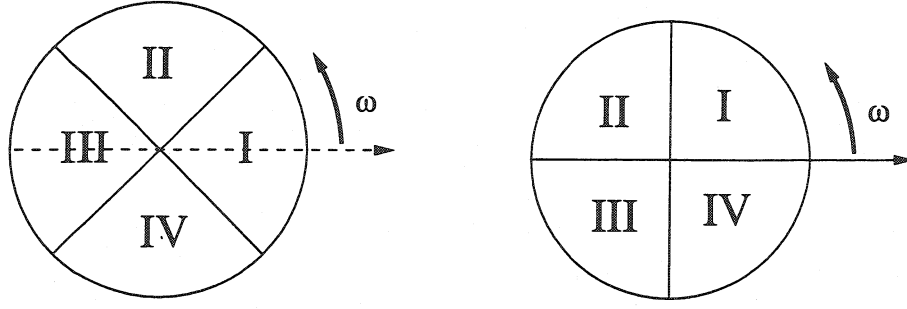
Figure 5.8: The division of the angular range in four sectors to calculate the asymmetries A_c (left figure) and A_s (right figure) is shown. The number of events in the sector I and III (II and IV) are counted positive (negative) as defined by the equations (5.12) and (5.13).

To calculate the asymmetries A_c and A_s the angular range is divided into four sectors each subtending 90° as shown in figure 5.8. The introduction of the notation

$$N_+ = \int_{\cos 2\omega > 0} d\sigma = N_I + N_{III} \tag{5.14}$$

$$N_- = \int_{\cos 2\omega < 0} d\sigma = N_{II} + N_{IV} \tag{5.15}$$

for A_c leads to the expression:

$$\begin{aligned} N_+ = \pi \{ &[C_0\hat{Q}_1(\epsilon) + D_0\hat{Q}_2(\epsilon)] (1 + \cos^2\theta_1) \\ + &[C_1\hat{Q}_1(\epsilon) + D_1\hat{Q}_2(\epsilon)] 2\cos\theta_1 \} \\ - &2C_2\hat{Q}_3(\epsilon) \sin^2\theta_1 \end{aligned} \tag{5.16}$$

$$\begin{aligned} N_- = \pi \{ &[C_0\hat{Q}_1(\epsilon) + D_0\hat{Q}_2(\epsilon)] (1 + \cos^2\theta_1) \\ + &[C_1\hat{Q}_1(\epsilon) + D_1\hat{Q}_2(\epsilon)] 2\cos\theta_1 \} \\ + &2C_2\hat{Q}_3(\epsilon) \sin^2\theta_1 \end{aligned} \tag{5.17}$$

If only a certain fiducial volume is considered, e.g $|\cos\theta_1^{max}| < c$, it follows:

$$\begin{aligned} N_+ = &\pi [C_0\hat{Q}_1(\epsilon) + D_0\hat{Q}_2(\epsilon)] (2c + \frac{2}{3}c^3) \\ - &2C_2\hat{Q}_3(\epsilon) (2c - \frac{2}{3}c^3) \end{aligned} \tag{5.18}$$

$$\begin{aligned} N_- = &\pi [C_0\hat{Q}_1(\epsilon) + D_0\hat{Q}_2(\epsilon)] (2c + \frac{2}{3}c^3) \\ + &2C_2\hat{Q}_3(\epsilon) (2c - \frac{2}{3}c^3) \end{aligned} \tag{5.19}$$

Channel	$\tilde{Q}_1$	$\tilde{Q}_2$	$\tilde{Q}_3$
e μ	0.945	0.020	0.038
e π	0.850	0.020	-0.107
e ρ	0.960	0.010	-0.049
μ π	0.951	-0.019	-0.112
μ ρ	0.968	0.006	-0.050
π π	0.937	-0.040	0.331
π ρ	0.961	-0.008	0.147
ρ ρ	0.967	0.006	0.077

Table 5.2: The table gives the values of the integrated $\hat{Q}_i$-functions. The integration limits correspond to the acolinearity cut which was applied in the selection. The integration was performed numerically using the convoluted functions given in Appendix B.

After an integration over the acolinearity angle one ends up with:

$$
\begin{aligned}
N_+ &= \pi \left[C_0\tilde{Q}_1 + D_0\tilde{Q}_2 \right] \left(2c + \frac{2}{3}c^3 \right) \\
&\quad - \ 2C_2\tilde{Q}_3 \left(2c - \frac{2}{3}c^3 \right)
\end{aligned} \tag{5.20}
$$

$$
\begin{aligned}
N_- &= \pi \left[C_0\tilde{Q}_1 + D_0\tilde{Q}_2 \right] \left(2c + \frac{2}{3}c^3 \right) \\
&\quad + \ 2C_2\tilde{Q}_3 \left(2c - \frac{2}{3}c^3 \right)
\end{aligned} \tag{5.21}
$$

$$
\tilde{Q}_i = \int_{\epsilon_1}^{\epsilon_2} \hat{Q}_i(\epsilon)d\epsilon \quad i = 1, 2, 3
$$

Finally the normalised spin correlation A_{TT} can be expressed in terms of measurable quantities:

$$
A_c = \frac{2C_2\tilde{Q}_3}{\pi C_0(\tilde{Q}_1 + \frac{D_0}{C_0}\tilde{Q}_2)}G \qquad A_{TT} = \frac{A_c\pi}{2G\tilde{Q}_3}(\tilde{Q}_1 - \mathcal{P}_\tau\tilde{Q}_2) \tag{5.22}
$$

An analogous consideration for A_s leads to

$$
A_s = \frac{2D_2\tilde{Q}_3}{\pi C_0(\tilde{Q}_1 + \frac{D_0}{C_0}\tilde{Q}_2)}G \qquad A_{TN} = \frac{A_s\pi}{2G\tilde{Q}_3}(\tilde{Q}_1 - \mathcal{P}_\tau\tilde{Q}_2) \tag{5.23}
$$

where the geometrical factor is:

$$
G = \frac{(3 - c^2)}{(3 + c^2)} \tag{5.24}
$$

The normalised spin correlations show a τ polarisation dependence which is suppressed by the small value of $\tilde{Q}_2$. The integration of the $\hat{Q}_i$-functions is performed numerically.

Channel	e μ	e π	e ρ	μ π	μ ρ	π π	π ρ	ρ ρ
δA_c^{rad}	0.010	0.013	0.012	0.010	0.014	0.013	0.013	0.027
δA_s^{rad}	0.006	0.002	-0.001	0.006	0.003	0.001	0.001	-0.007

Table 5.3: The radiative corrections for A_c and A_s. The errors on the corrections are five times smaller. The values are calculated taking into account cuts on the fiducial volume. The electroweak and vacuum polarisation corrections are not included.

The integrals of the $\hat{Q}_i$-functions which are used to calculate A_{TT} and A_{TN} are shown in table 5.2. The ratios and the sign of the integrals $\tilde{Q}_3$ are in agreement with the sensitivity as shown in table 5.1. Small deviations occur due to the different integration limits. The following procedure is applied to measure the spin correlations A_{TT} and A_{TN}.

1. The exclusive final states eμ, eπ, eρ, $\mu\pi$, $\mu\rho$, $\pi\pi$, $\pi\rho$ and $\rho\rho$ are selected and the ω distribution is measured.

2. The expected background is subtracted. In addition a bin by bin efficiency correction is applied.

3. The asymmetries A_c and A_s are calculated for each channel. The values are translated into the normalised spin correlations using equation (5.22) and (5.23).

4. The results for the eight exclusive final states are averaged.

5.3 Radiative Corrections to A_c and A_s

In order to determine A_c and A_s, the influence of the QED radiative corrections on the observables was investigated. Since no single Monte Carlo generator exists which contains the full spin implementation and higher order radiative corrections, the results of the KORALZ and KORALB generators are combined [52]. The Standard Model expectation on the Z peak is then expressed by the sum of different contributions:

$$
\begin{aligned}
A_c^{SM} &= A_c \, {}^{KORALB}_{Born,fullspin} \\
&+ A_c \, {}^{KORALZ}_{\mathcal{O}(\alpha^2),long.spin} - A_c \, {}^{KORALZ}_{Born,long.spin}
\end{aligned}
\tag{5.25}
$$

The first term contains the asymmetry due to transverse-transverse spin correlations at Born level. The following difference, calculated using KORALZ with and without QED higher order corrections, gives an estimate of the contribution from QED radiative corrections to A_c:

$$
\delta A_c^{rad} = A_c \, {}^{KORALZ}_{\mathcal{O}(\alpha^2),long.spin} - A_c \, {}^{KORALZ}_{Born,long.spin}
\tag{5.26}
$$

The contributions to the observable from higher order processes are at the 1% level. The correction δA_c^{rad} has to be applied to a measured asymmetry A_c^{meas} in order to get the

Born level asymmetry A_c^{Born}.

$$A_c^{Born} \quad = \quad A_c^{meas} - \delta A_c^{rad} \tag{5.27}$$

A_{TT} as defined in equation (5.22) can be calculated only from the quantaty A_c^{Born}. An analogous consideration leads to the radiative corrections for A_s. The values are given in table 5.3. Since the electroweak and the vacuum polarisation corrections are not removed the couplings derived from the spin correlation measurement are considered as effective coupling constants in the improved Born approximation.

Chapter 6

Data Analysis

6.1 Selection

The data of this analysis were collected in 1994 and consist of approximately 64 000 $Z \to \tau\tau$ decays. The selection of τ decay candidates proceeds in three steps. First a dilepton sample is preselected from the total data sample recorded with L3 which includes e^+e^-, $\mu^+\mu^-$ and $\tau^+\tau^-$ final states. The preselection process rejects mainly hadronic Z decays and beam-gas interactions. The preselected dilepton events are divided into two hemispheres defined by a plane perpendicular to the event thrust axis. The thrust axis $\hat{T}$ is a vector that minimises the expression $|\sum \vec{P_i}\hat{T}|$ where $\vec{P_i}$ is the momentum of the i'th particle. In a second step the particle identification algorithm is applied in each hemisphere independently in order to select one of the following τ decay modes: $\tau \to e\bar{\nu}\nu$, $\tau \to \mu\bar{\nu}\nu$, $\tau \to \pi\nu$, $\tau \to \rho\nu$. Finally the events are classified as one of the following channels: $\tau\tau \to e\mu$, $e\pi$, $e\rho$, $\mu\pi$, $\mu\rho$, $\pi\pi$, $\pi\rho$, $\rho\rho$ or πX where X is any one-prong τ decay. The measurement of $\mathcal{A}_e$ and $\mathcal{A}_\tau$ is based on the πX sample. The exclusive final states are used to measure the spin correlations. The selection criteria are described in the subsequent sections. The identification of the τ decay modes is constrained to the fiducial volume $|\cos\theta| < 0.71$.

6.1.1 Preselection

$Z \to \tau\tau$ events are characterised by low track multiplicity. The number of tracks depends on the τ decay mode and is typically less than 6. Most of the hadronic Z decays are rejected due to the cuts

- the number of BGO clusters must be less than 26.

- the number of TEC tracks in any hemisphere has to be less than 6.

Events containing cosmic muons are rejected by the requirements

- the $|DCA|$ of all tracks has to be less than 15 mm and at least one track has a $|DCA|$ of less than 10 mm.

51

- there has to be at least one hit in the scintillation counters within 5 ns after the beam crossing.

The preselection also reduces background from two photon interactions $e^+e^- \rightarrow e^+e^- f\bar{f}$. These events are characterised by a low scattering angle of the incoming electron and positron which carry a large fraction of the beam energy and remain undetected. The $f\bar{f}$ pair tend to have low energy, a small transverse momentum and may have large acolinearity. Background from two photon interactions is suppressed demanding

- at least one TEC track with a transverse momentum greater than 1 GeV.

- the transverse energy imbalance to be larger than 3 GeV if the acolinearity of two tracks is larger than 25°.

The final preselection efficiency over 4π obtained from a τ Monte Carlo sample is 93%.

6.1.2   Particle Identification

The particle identification of one-prong τ decays is based on the topological properties of the energy deposition in the calorimeters. This technique is found to be relatively independent of the energy of the τ decay products [55, 56]. The signature of an electron consists of a narrow, symmetric electromagnetic shower in the BGO matching a TEC track. The energy leakage into the HCAL is small and restricted to the first 3 layers. The observed shower profile in a 3 × 3 BGO crystal matrix around the shower maximum is fitted with a reference profile. The reference profile was determined by the average shower shape obtained from Bhabha events. The shower shape is independent of the particle energy for energies greater than 1 GeV [57]. The χ^2_{em} of the fit defines the compatibility that the shower was produced by an electromagnetic interacting particle.

The characteristic of a muon is a minimum ionising signature in the calorimeters and a track in the muon spectrometer matching a TEC track. The measured energy deposits in the HCAL lying along a straight line are fitted with the expectation for minimum ionising particles. The χ^2_{mip} of the fit defines the compatibility of the energy deposit in the HCAL with that produced by a minimum ionising particle. In contrast to muons with a $\chi^2_{mip} \approx 1$ hadronic showers have a $\chi^2_{mip} \gg 1$. Apart from the energy deposits, the number of measured (N_{meas}) and expected (N_{exp}) hits along the line are used to distinguish muons from hadrons in the HCAL. Since muons follow a straight trajectory a large fraction of HCAL cells register hits. Hadrons on the other hand interact in the absorber plates with an energy deposition over a wide area, but the number of hits along the line is small.

Pions and Rhos are distinguished from one another whether or not a neutral pion accompanies the charged pion. Due to the boost of the τ's their decay products generate overlapping energy clusters in the BGO. In order to discriminate between the hadronic τ decay modes and to assign the energy to the particles in a proper way it is necessary to separate the contributions to the BGO energy deposit from charged hadrons and from photons produced by π^0 decays. The algorithm to reconstruct overlapping energy clusters
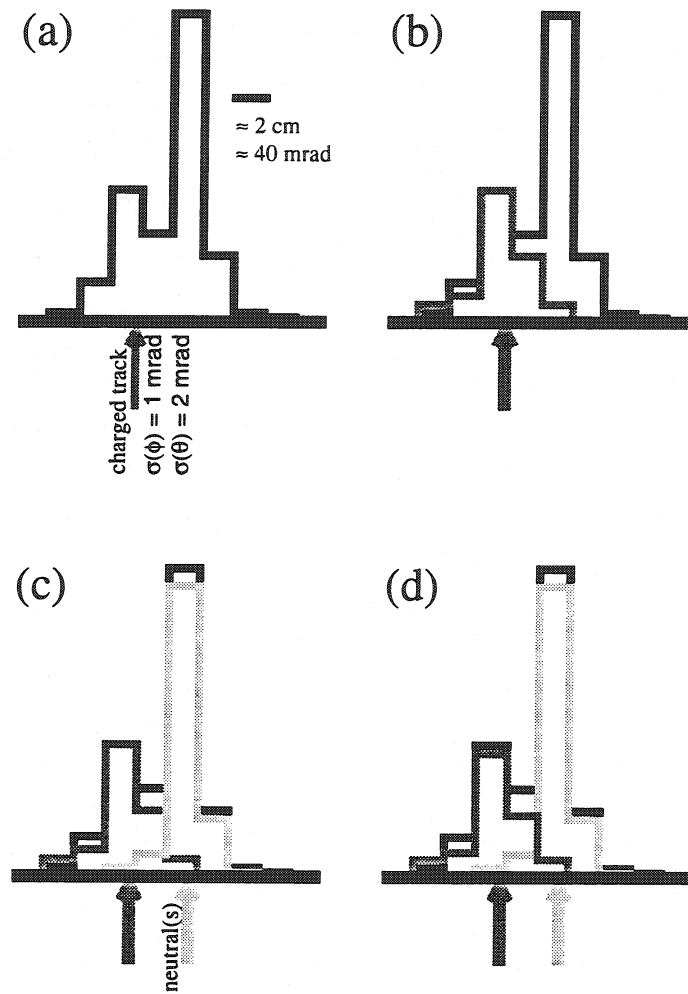
Figure 6.1: The iterative procedure used to separate clusters of charged and neutral particles in the BGO.

in the BGO originating from one charged hadron and several photons, is based on the fact that the shower shapes in the BGO are different. The procedure to reconstruct neutral electromagnetic clusters in the vicinity of hadronic energy deposits in the BGO is illustrated in figure 6.1.

1. The extrapolation of the TEC track to the BGO predicts the charged hadron impact point (Figure 6.1a).

2. The expected energy deposition of the charged hadron whose shape is assumed to be energy independent is subtracted from the complete energy deposit for each crystal separately (Figure 6.1b).

3. The remaining energy distributions are fitted with electromagnetic shower profiles

in order to determine the energy and position of the neutral clusters. Clusters that fit better with the sum of two profiles are split in order to take into account the possibility of two merged photons (Figure 6.1c).

4. The subtraction of the electromagnetic energy contribution leads to a new estimation of the charged hadron energy deposit. The steps 2 and 3 are iterated until stable energies are obtained for each particle (Figure 6.1d).

After the neutral clusters are identified the following possibilities are considered to reconstruct neutral pions:

* There are two neutral clusters where the most energetic cluster has an energy greater than 400 MeV. The invariant mass of the two clusters is equal to the π^0 mass within a mass window between 30 MeV to 60 MeV.

* There is only one neutral cluster with an energy greater than 1 GeV. The invariant mass $M_{\gamma\gamma}$ obtained by fitting the cluster with two electromagnetic profiles fulfil $100 \text{ MeV} \leq M_{\gamma\gamma} \leq 200 \text{ MeV}$ or the χ^2_{em} of the fit is less than 50.

Selection of $\tau \to e\bar{\nu}\nu$

The typical electron signature is shown in figure 6.2. The following requirements define an electron candidate.

1. The hemisphere contains only one track. The angle between the shower centre and the extrapolation of the track is required to be within 5 σ of the resolution.

2. The electromagnetic shower consists of at least 4 BGO crystals.

3. The χ^2_{em} must be less than 30.

4. The probability that the momentum measured by the TEC and the energy deposit in the BGO are consistent has to be greater than 0.00005.

5. The energy deposit in the HCAL has to be less than 3 GeV and is consistent with the tail of an electromagnetic shower.

The electron selection efficiency is 86.1% in the fiducial volume. The background contribution due to other τ decays is 1.5%.

Selection of $\tau \to \mu\bar{\nu}\nu$

The detector response for a muon is shown in figure 6.3. The following cuts are applied to select muon candidates.

1. The hemisphere contains only one track.

2. The energy deposit in the BGO is less than 3 GeV.
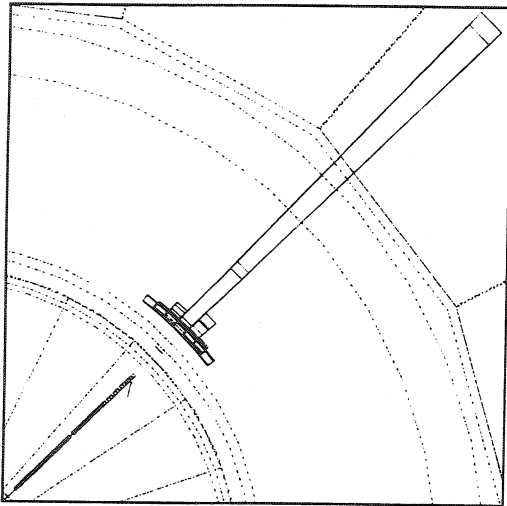
Figure 6.2: The electron signature consists of a narrow shower in the BGO matching a TEC track.
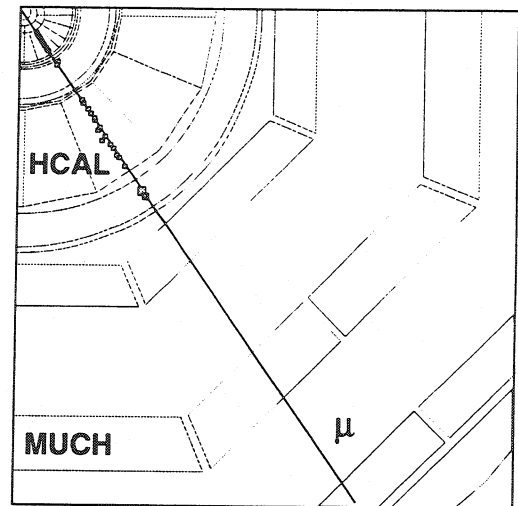
Figure 6.3: The typical muon response in L3 consists of a minimum ionising particle in HCAL matching a TEC track and hits in the muon spectrometer.

3. The energy deposit in the HCAL is less than 10 GeV.

4. The χ^2_{mip} is less than 500.

5. The ratio N_{meas}/N_{exp} is larger than 0.45.

6. There have to be at least two P-chambers hits and one Z-chamber hit in the muon spectrometer.

7. The back-tracking from the muon chamber matches a TEC track.

The muon selection efficiency in the fiducial volume is 78.9%. The background contribution from other τ decays is estimated to be 0.9%.

Selection of $\tau \to \pi\nu$

The $\tau \to \pi\nu$ signature is shown in figure 6.4. Events which fulfil the following criteria are considered as pion candidates.

1. The BGO energy in a cone of 30° around the track is larger than 200 MeV or the HCAL energy exceeds 600 MeV.

2. The BGO energy in the cone is less than 35 GeV.

3. The energy of a reconstructed track in the muon chambers has to be less than 30 GeV.
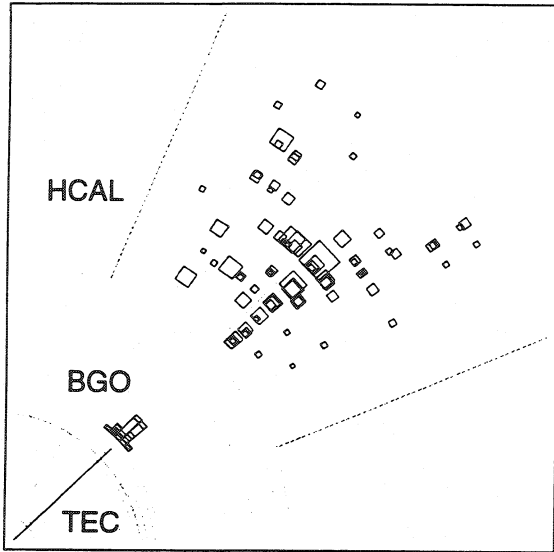
Figure 6.4: The characteristic signature of a charged pion is a wide shower in the BGO matching a TEC track and energy deposit in the HCAL.

4. There is no π^0 candidate in the same hemisphere.

5. The probability that the observed track momentum and calorimetric energy originate from a single hadron is required to exceed 0.003.

If the shower shape is consistent with an electron the candidate is rejected. In addition the energies measured in the calorimeter do not result from a minimum ionising particle. The selection efficiency of $\tau \to \pi\nu$ decays is 71.5% in the fiducial volume. The background from other τ decays, mainly $\tau \to \rho\nu$, has been found to be 9.5%.

Selection of $\tau \to \rho\nu$

A $\tau \to \rho\nu$ candidate is presented in figure 6.5. In order to identify a $\tau \to \rho\nu$ decay the ρ decay products are selected. The following cuts are applied:

1. There has to be one track consistent with a charged pion.

2. There has to be exactly one π^0 candidate.

3. The BGO energy in a cone of 30° around the track is greater than 200 MeV and less than 44 GeV.

4. The energy of a reconstructed muon chamber track is less than 30 GeV.

5. The reconstructed energy of the ρ is larger than 5 GeV.

6. The probability that the observed track momentum and calorimetric energy originate from a single hadron is required to exceed 0.001.

7. The invariant mass $M_{\pi^\pm \pi^0}$ is between 450 MeV and 1200 MeV.
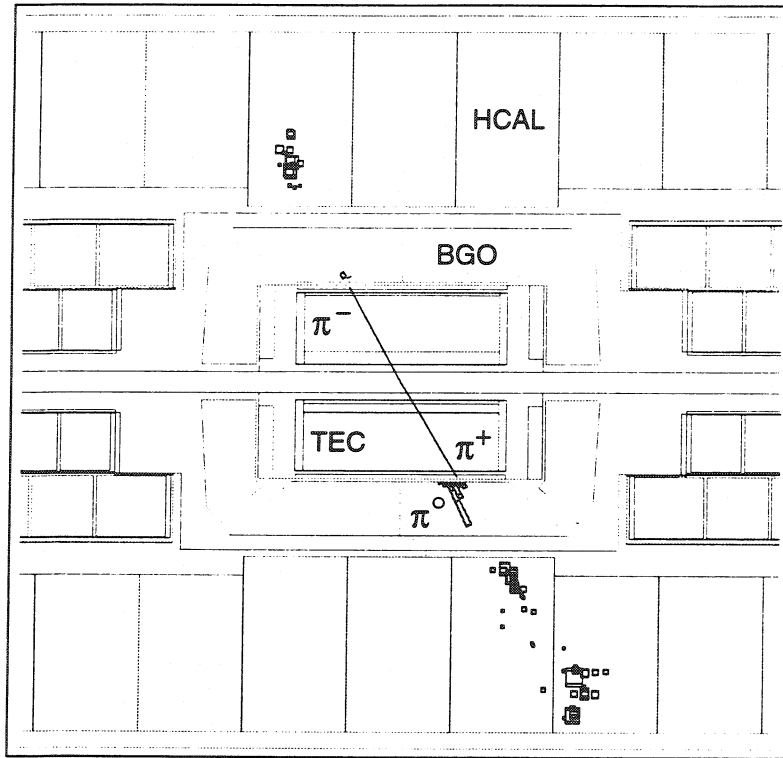
Figure 6.5: The event picture shows a $\tau \to \pi\nu$ candidate in the upper hemisphere and a $\tau \to \rho\nu$ candidate in the lower hemisphere. As can be seen the TEC track doesn't match with the electromagnetic cluster of the ρ decay.

In the fiducial volume the selection efficiency is 65.9%. The background from other τ decays was found to be 12.4%. The invariant masses $M_{\gamma\gamma}$ and $M_{\pi^{\pm}\pi^0}$ are shown in figure 6.6.

6.1.3 Event Selection

After the selection of one-prong τ decays in the hemispheres the event selection is performed. Only one-prong τ decays are considered where each track has to be reconstructed with at least one assigned SMD z-hit. As mentioned in chapter 4.3 this reduces the total amount of selected events to 74%. The BGO energy must be reliably measured, i.e. the number of dead crystals around the impact point of the track has to be less than 2. The following criteria are applied to suppress remaining non-τ background for the different decay channels:
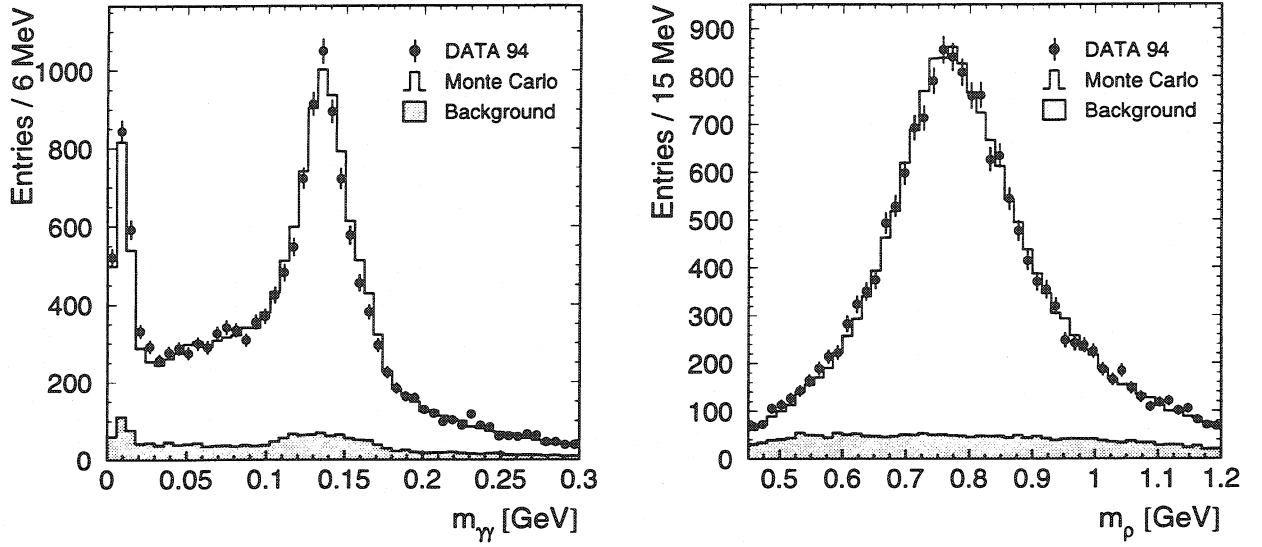
Figure 6.6: The left(right) figure shows the reconstructed π^0 (ρ) mass for all selected $\tau \to \rho\nu$ candidates in 1994. Data and Monte Carlo are in very good agreement.

$\tau\tau \to \pi X$

All events with at least one identified pion are considered for the πX selection. To suppress the non-τ background contributions events which fulfil any one of the following criteria are rejected.

- The energy of an electron or muon in the opposite hemisphere exceeds 40 GeV.

- The total BGO energy is greater than 68% of the centre of mass energy.

- The total energy in the BGO and in the HCAL is less than 2 GeV.

- The acolinearity is greater than 16°.

- The total calorimetric energy is less than 15 GeV and the transverse momentum difference of both tracks has to be $|P_T^1| - |P_T^2| < 1$ GeV.

- The $|DCA|$ of one track is greater than 2 mm.

To take into account the gap in the muon spectrometer around $\theta = 90°$ events are rejected if the $|\cos\theta| < 0.1$ together with a minimum ionising signature in both hemispheres. This set of cuts reject $e^+e^- \to e^+e^-$ and $e^+e^- \to \mu^+\mu^-$ events which fake $\tau \to \pi\nu$ decays. Cosmic muons which pass the detector and interact in the HCAL are suppressed by the $|DCA|$ requirement. The cuts on transverse momenta and acolinearity suppress background from two photon interactions. The selection efficiency in the fiducial volume is 66.2%. The remaining background contributions are given in table 6.1.

Channel	Background [%]
$\tau \to e\bar{\nu}\nu$	1.2
$\tau \to \mu\bar{\nu}\nu$	1.7
$\tau \to \rho\nu$	4.7
other τ decays	2.4
$e^+e^- \to e^+e^-$	1.4
$e^+e^- \to \mu^+\mu^-$	0.6
$e^+e^- \to e^+e^-f\bar{f}$	0.4
cosmics	0.3
total	12.7

Table 6.1: The background contributions in the final state πX.

$\tau\tau \to e\mu$

The acolinearity has to be in the range $0.5° \le \epsilon \le 15°$. The energy of the muon must be less than 45 GeV and the scintillator hit assigned to the muon track has to be within 2 ns of the beam crossing time. The sum $|DCA_1| + |DCA_2|$ is less than 5 mm. At least one TEC track has transverse momentum greater than 3 GeV.

$\tau\tau \to e\pi$

The acolinearity has to be in the range $1.5° \le \epsilon \le 15°$. The total BGO energy is required to be less than 65% of the centre of mass energy. At least one TEC track has transverse momentum greater than 3 GeV. Since electrons can pass through the cracks in the BGO and shower in the HCAL faking pions events are rejected if the energy of the electron exceeds 40 GeV.

$\tau\tau \to e\rho$

The acolinearity has to be in the range $0.5° \le \epsilon \le 15.0°$. The energy of the electron does not exceed 40 GeV. At least one TEC track has transverse momentum greater than 3 GeV.

$\tau\tau \to \mu\pi$

The acolinearity has to be in the range $1.0° \le \epsilon \le 15.0°$. The scintillator hit assigned to the muon track must be within 2 ns of the beam crossing time. The sum $|DCA_1| + |DCA_2|$ is less than 2 mm. The total calorimetric energy is greater than 2 GeV. At least one TEC track has transverse momentum greater than 4 GeV.

Channel $\tau\tau \to$	Number of events	ε (%) in 4π	Background (%) $\tau\tau \not\to$	Background (%) non-τ
e μ	1181	32.3	2.2	0.2
e π	574	22.6	9.4	1.2
e ρ	1560	25.0	13.6	0.1
μ π	717	25.5	9.5	2.8
μ ρ	1319	22.5	13.1	0.2
π π	260	23.3	16.8	0.3
π ρ	1020	21.1	20.1	—
ρ ρ	793	17.8	22.6	—

Table 6.2: Number of selected events for the considered decay channels together with the average acceptance ε and the background contributions where $\tau\tau \not\to$ denotes misidentified other τ decays.

$\tau\tau \to \mu\rho$

The acolinearity has to be in the range $0.5° \le \epsilon \le 15.0°$. The scintillator hit assigned to the muon track must be within 2 ns of the beam crossing time. The sum $|DCA_1| + |DCA_2|$ is less than 3 mm. The muon energy has to be less than 36 GeV. At least one TEC track has transverse momentum greater than 3 GeV.

$\tau\tau \to \pi\pi$

The acolinearity has to be in the range $0.5° \le \epsilon \le 15.0°$. The sum $|DCA_1| + |DCA_2|$ is less than 2 mm. The total BGO energy has to be less than 35% of the centre of mass energy. At least one TEC track has transverse momentum greater than 4 GeV.

$\tau\tau \to \pi\rho$

The acolinearity has to be in the range of $0.5° \le \epsilon \le 15.0°$. The sum $|DCA_1| + |DCA_2|$ is less than 4 mm. At least one TEC track has transverse momentum greater than 4 GeV.

$\tau\tau \to \rho\rho$

The acolinearity has to be in the range of $0.5° \le \epsilon \le 10.0°$. The sum $|DCA_1| + |DCA_2|$ is less than 4 mm. The total BGO energy has to be less than 90% of the centre of mass energy.

The number of selected events together with the selection efficiencies and background contributions are summarised in table 6.2. For one-hadron final states the background from other τ decays is in the order of 10% rising to 20% for the hadron-hadron final states. Due to the fact that a π^0 has to be reconstructed for a ρ to be identified, the

non-τ background contribution is small. The normalised energy spectra of the selected particles are shown in figure 6.7.
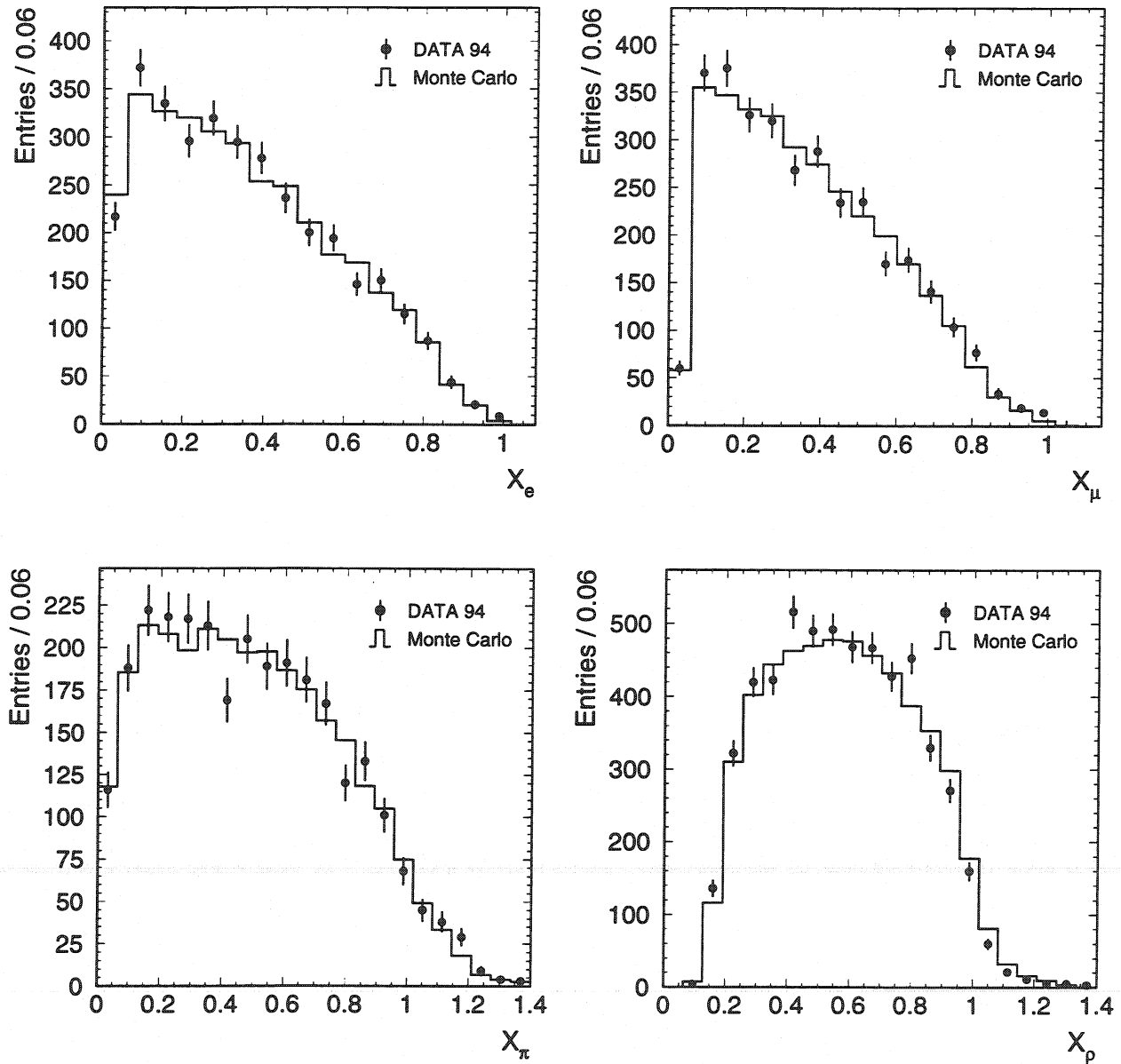
Figure 6.7: Comparison between the normalised particle energy spectra for data and Monte Carlo after the exclusive channel selection.

Chapter 7

The Measurement of $\mathcal{A}_\tau$ and $\mathcal{A}_e$

In this chapter the results of the τ polarisation measurements are presented. The aim is the determination of $\mathcal{A}_\tau$ and $\mathcal{A}_e$, the quantities directly related to the weak neutral current couplings. The result is obtained in two steps. First the polarisation $\mathcal{P}_\tau$ is determined for seven bins in $\cos\theta$ with $|\cos\theta| < 0.71$. In the next step the results are corrected for radiative effects and fitted with formula (1.58). For this analysis 4198 πX events have been selected.

Charge Determination

$\mathcal{P}_\tau(\cos\theta)$ is determined by measuring the polarisation in seven regions of $\cos\theta$ where θ is the angle of the τ^- which is approximated using the event thrust axis and the charge of the τ travelling into the $\cos\theta > 0$ hemisphere. In order to assign the correct $\cos\theta$ bin the charge of the τ decay product has to be determined using the track curvatures. The fraction of events where the sign of both curvatures are identical is 3.5%. This charge confusion value is well reproduced in the Monte Carlo.

If at least one hemisphere contains a muon the charge is unambiguously defined by the muon spectrometer. Otherwise the charge is calculated by the difference of the curvatures weighted by the errors of the two TEC tracks

$$Q_1 = \text{sign}\left[\frac{\mathcal{C}_1}{\delta\mathcal{C}_1} - \frac{\mathcal{C}_2}{\delta\mathcal{C}_2} \right] \tag{7.1}$$

where Q_1 is the charge in direction of the thrust axis, $\mathcal{C}_i = 1/P_{T_i}$ is the track curvature and $\delta\mathcal{C}_i$ its error. The charge confusion is reduced to 0.6% if both hemispheres are used to determine the charge corresponding to (7.1). Figure 7.1 shows the charge separation for the selected πX final states.

Fitting Procedure

The τ polarisation may be determined by fitting the τ decay spectra with analytical functions, where the analytical functions have to be corrected for detector resolution and acceptance effects. In this analysis the polarisation sensitive distribution is fitted
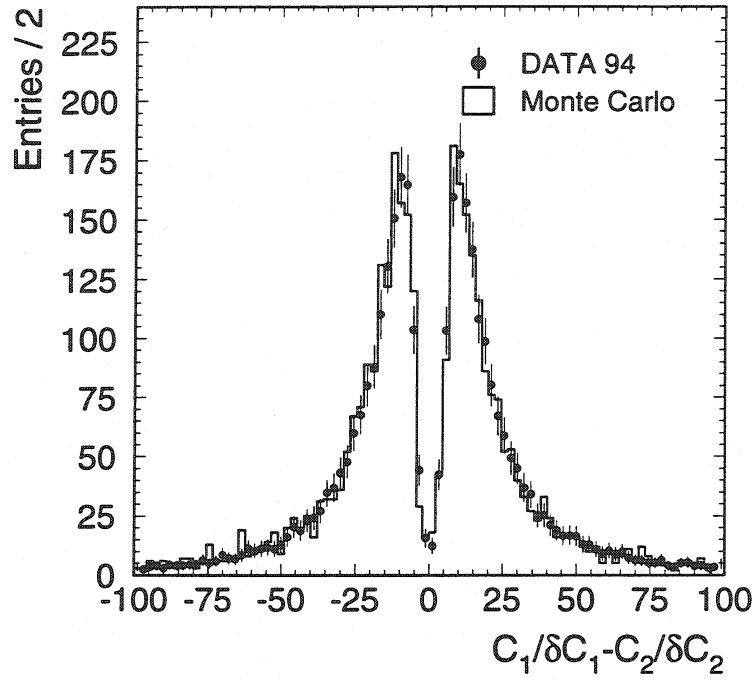
Figure 7.1: The charge separation for all selected πX final states. The average charge confusion was estimated to be 0.6%.

by a linear combination consisting of the two helicity states and the unpolarised non-τ background contribution.

$$N_D^i = R \ (\frac{1 + \mathcal{P}_\tau}{1 + \hat{\mathcal{P}}_\tau} \ N_+^i + \frac{1 - \mathcal{P}_\tau}{1 - \hat{\mathcal{P}}_\tau} \ N_-^i \ ) + \sum_j R_{BG_j} N_{BG_j}^i \qquad (7.2)$$

with:

N_D^i	=	Number of events in the data sample
N_+^i	=	Number of Monte Carlo events with helicity $h_\tau = +1$
N_-^i	=	Number of Monte Carlo events with helicity $h_\tau = -1$
$N_{BG_j}^i$	=	Number of background events from source j
$\mathcal{P}_\tau$	=	τ polarisation, free fit parameter
$\hat{\mathcal{P}}_\tau$	=	τ polarisation generated in the Monte Carlo
R	=	normalisation factors
i	=	bin number

The normalisation factor is given by :

$$R = \frac{\sum_i N_+^i + N_-^i}{\sum_i N_D^i} \tag{7.3}$$

Since background from misidentified τ decay channels depends on polarisation it is included in the Monte Carlo distributions N_+^i and N_-^i. Although the Monte Carlo sample is approximately 8 times larger than the data sample, statistical fluctuations are not negligible and must be taken into account. The probability to observe n_i data events in the i'th bin is:

$$P_i^{Data} = \frac{e^{-\nu_i} \nu_i^{n_i}}{n_i!} \qquad \nu_i = \sum_{j=1}^{K} \mu_{ij} \, r_j \tag{7.4}$$

where the mean value ν_i is expressed by the Monte Carlo prediction. The index j labels the different Monte Carlo contributions and background sources. The factor r_j normalises each contribution independently. Since the number of Monte Carlo events is finite it follows also a Poisson distribution, where the underlying mean value μ_{ij} is unknown. The probability to observe m_{ij} Monte Carlo events in bin i from source j is given by:

$$P_i^{MC} = \frac{e^{-\mu_{ij}} (\mu_{ij})^{m_{ij}}}{m_i^{ij}!} \tag{7.5}$$

The combined probability reads

$$P_i = \frac{e^{-\nu_i} \nu_i^{n_i}}{n_i!} \prod_{j=1}^{K} \frac{e^{-\mu_{ij}} (\mu_{ij})^{m_{ij}}}{m_{ij}!} \tag{7.6}$$

In order to construct the likelihood function the unknown underlying mean values μ_{ij} are integrated out assuming all values of μ are equally likely [58].

$$b_i = \int \ldots \int P_i \, d\mu_{i1} \ldots d\mu_{iK} \tag{7.7}$$

The likelihood to be maximised is:

$$\mathcal{L} = \prod_{i=1}^{\sharp \, bins} b_i \tag{7.8}$$

The minimisation of $-\ln\mathcal{L}$ as a function of the τ polarisation was performed with the software package MINUIT [59].
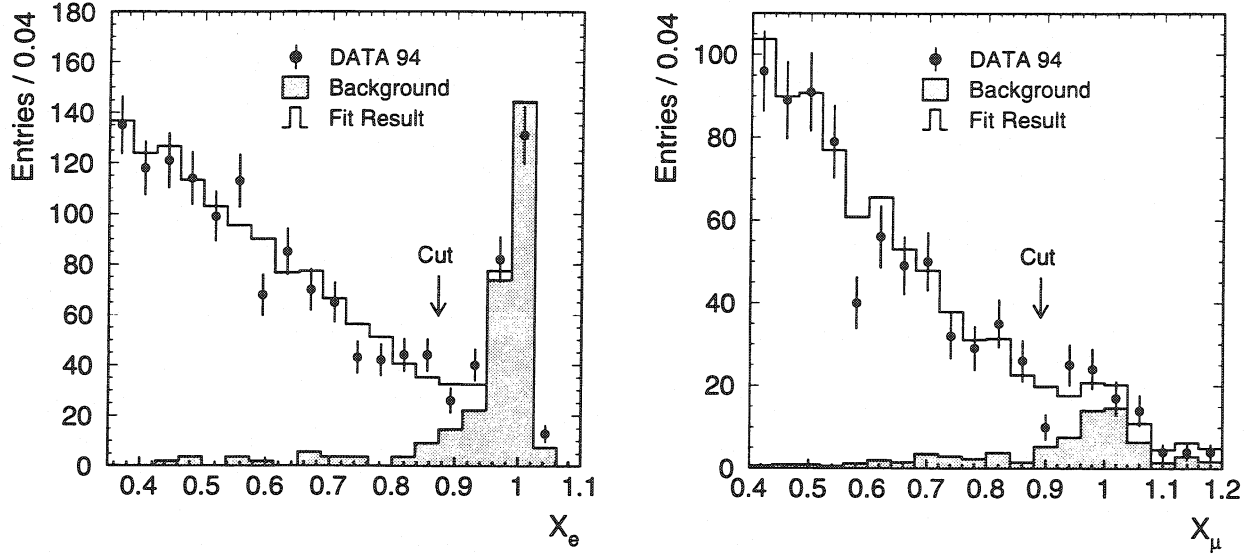
Figure 7.2: The contributions of non-τ background sources in the πX event sample. Each figure shows the data together with the fit result and the background contribution. The normalised energy X is measured in the hemisphere opposite to the selected $\tau \rightarrow \pi \nu$ decay, where X_e is the normalised BGO energy and X_μ the normalised muon energy. The arrow indicates the cut value which was used in $\tau\tau \rightarrow \pi X$ selection.

7.1 Systematic Errors

The non-τ Background

The background contributions from $e^+e^- \rightarrow e^+e^-$, $e^+e^- \rightarrow \mu^+\mu^-$ and two-photon interactions were estimated normalising the Monte Carlo expectation to data. The Bhabha background was determined by selecting hemispheres which pass the $\tau\tau \rightarrow \pi X$ selection criteria where the cut which rejects events with electrons in the opposite hemisphere whose energy exceeds 40 GeV was removed. In order to obtain the background normalisation the obtained data distribution was fitted with the selected Bhabha and τ Monte Carlo sample. The error of the fit reflects the statistical uncertainty on the normalisation. The background contribution from $e^+e^- \rightarrow \mu^+\mu^-$ events was estimated analogously removing the cut on the muon energy on the opposite hemisphere. The fit results together with the cut values are presented in figure 7.2.

The two photon background was estimated by selecting hemispheres which pass all the $\tau\tau \rightarrow \pi X$ selection cuts where the acolinearity cut was replaced by $30° < \epsilon < 60°$. Events within this interval belong mainly to the two photon interactions. From a fit of the distributions the two photon background normalisation is obtained. The background

Source	$\Delta \mathcal{A}_\tau$	$\Delta \mathcal{A}_e$	$\Delta \mathcal{A}_{e-\tau}$
Selection	0.006	0.005	0.004
Branching fractions	0.008	0.001	0.006
Angular resolution	0.010	0.009	0.005
Background	0.006	0.001	0.004
Charge Confusion	0.001	0.003	0.001
total	0.015	0.011	0.010

Table 7.1: Summary of systematic errors on $\mathcal{A}_\tau$, $\mathcal{A}_e$ and $\mathcal{A}_{e-\tau}$ measured in the πX channel.

uncertainties are 6% for the Bhabha background, 18% for the dimuon background and 15% for the two photon background. The systematic error due to the background contribution is given in table 7.1.

Uncertainty in the angular resolution

The angular resolution together with the uncertainty has been presented in figure 4.4. In order to estimate the effect of uncertainty in angular resolution, the resolutions have been varied within their errors. The bias is given in table 7.1.

Uncertainty of the Branching fractions

The background from other τ decays which are misidentified as pions is sensitive to the polarisation and was included in the Monte Carlo helicity distributions. The contribution from this background depends on the τ branching fractions. To estimate the systematic error the branching fractions were changed within their errors as given in table 2.1. To get the maximal bias all background fractions have been increased or decreased simultaneously, where the sum of all contributions was normalised to 1.

Bias in the $\tau \to \pi\nu$ selection

The number of events with positive and negative helicity can be calculated from the fitted polarisation $\mathcal{P}_\tau$ and the total number of events N.

$$N^+ = \frac{1}{2}(\mathcal{P}_\tau + 1)N \qquad N^- = \frac{1}{2}(1 - \mathcal{P}_\tau)N \qquad (7.9)$$

In order to estimate the bias due to the selection criteria, the selection cuts were changed within reasonable limits. It was assumed that the variation in the number of events, ΔN, belongs to one helicity state only. The new polarisation $\tilde{\mathcal{P}}_\tau$ was calculated using:

$$\tilde{\mathcal{P}}_\tau = \frac{N^- - \tilde{N}^+}{N^- + \tilde{N}^+} \qquad \tilde{N}^+ = N^+ + \Delta N \qquad (7.10)$$

$\cos\theta$	$\mathcal{P}_\tau$	$\delta\mathcal{P}_\tau^{QED}$	$\Delta\mathcal{P}_\tau^{stat}$	$\Delta\mathcal{P}_\tau^{back}$	$\Delta\mathcal{P}_\tau^{brfr}$	$\Delta\mathcal{P}_\tau^{sele}$	$\Delta\mathcal{P}_\tau^{charge}$	$\Delta\mathcal{P}_\tau^{reso}$
$[-0.71, -0.51]$	0.050	0.000	0.155	0.008	0.007	0.004	0.004	0.008
$[-0.51, -0.30]$	-0.022	-0.001	0.160	0.003	0.005	0.003	0.002	0.006
$[-0.30, -0.10]$	-0.168	-0.003	0.171	0.007	0.009	0.005	0.004	0.070
$[-0.10, +0.10]$	0.135	-0.004	0.190	0.004	0.010	0.004	0.000	0.027
$[+0.10, +0.30]$	-0.254	-0.005	0.173	0.007	0.012	0.006	0.000	0.021
$[+0.30, +0.51]$	-0.249	-0.005	0.148	0.006	0.005	0.007	0.002	0.005
$[+0.51, +0.71]$	-0.189	-0.004	0.162	0.007	0.009	0.003	0.004	0.014

Table 7.2: The values for $\mathcal{P}_\tau$ together with the systematic error are given. In order to fit $\mathcal{A}_\tau$ and $\mathcal{A}_e$ the radiative corrections $\delta\mathcal{P}_\tau^{QED}$ are added to $\mathcal{P}_\tau$ for each bin.

This procedure leads to a maximal bias which is assigned as systematic error. The variation of several selection cuts leads to independent error contributions which were added in quadrature. The total systematic error can be found in table 7.1.

Charge Confusion

A systematic error in $\mathcal{P}_\tau(\cos\theta)$ can be produced if the charge confusion in data is not well reproduced in Monte Carlo. In this case the number of events migrating from the negative signed $\cos\theta$ bin to the positive signed $\cos\theta$ bin and vice versa in data and Monte Carlo are different. The systematic error was estimated by fitting the acolinearity distributions using on one hand the true charge as given by the Monte Carlo and on the other hand the reconstructed charge as given by equation 7.1. This procedure leads to a conservative systematic error, because the full effect of charge confusion is considered instead of the effect of disagreement between Monte Carlo and data. The observed variation of the mean values is given as systematic error.

7.2 Results

In order to fit the polarisation as a function of $\cos\theta$ with equation (1.58) the results have to be corrected for QED radiative effects. The corrections $\delta\mathcal{P}_\tau^{QED}$ were obtained using the analytical program ZFITTER [60], which takes into account initial and final state radiation, γ exchange and γ-Z interference. The result for each bin together with the statistical and systematic uncertainties are summarised in table 7.2. The results of the fits are shown in figure 7.3 where the dashed and solid line corresponds to the fit without and with lepton universality ($\mathcal{A}_{e-\tau}$), respectively. The results of the fits are:

$$\begin{aligned}
\mathcal{A}_\tau &= 0.110 \pm 0.063 \ (\text{stat.}) \pm 0.015 \ (\text{sys.}) \\
\mathcal{A}_e &= 0.149 \pm 0.095 \ (\text{stat.}) \pm 0.011 \ (\text{sys.}) \\
\mathcal{A}_{e-\tau} &= 0.122 \pm 0.053 \ (\text{stat.}) \pm 0.010 \ (\text{sys.})
\end{aligned}$$
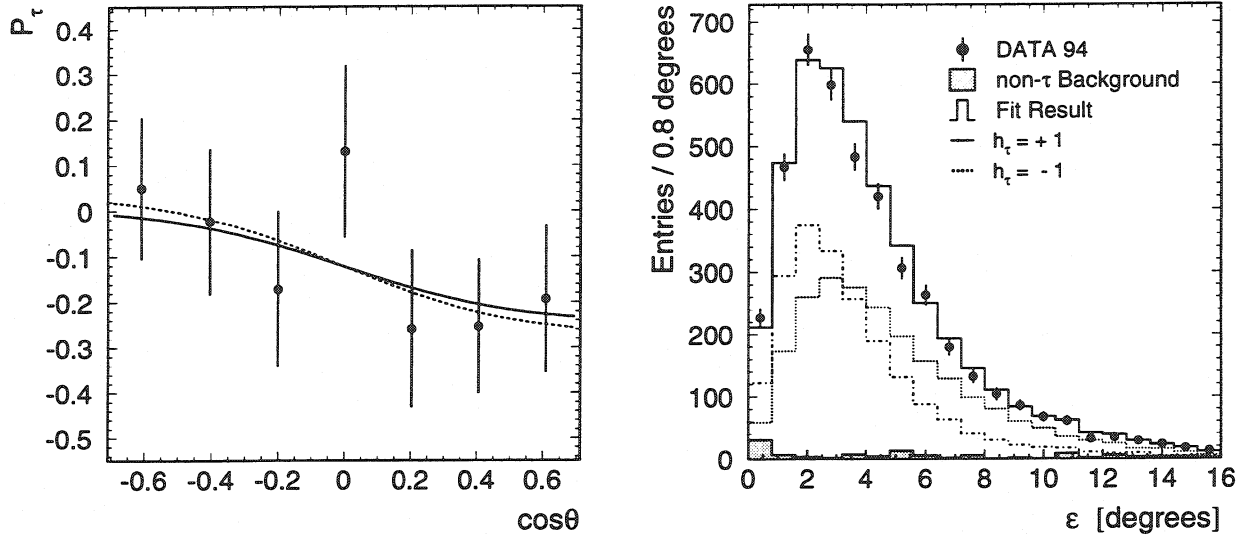
Figure 7.3: The τ polarisation as a function of $\cos\theta$ is shown in the left picture. The error is statistical only. The solid and dashed line indicates the fit result with and without lepton universality. The right figure shows the acolinearity distribution together with the fit result, the fitted helicity states and the unpolarised background contribution.

Assuming lepton universality the effective weak mixing angle is calculated to be:

$$\sin^2\bar\theta_W = 0.235 \pm 0.007$$

where the systematic and statistical errors are added in quadrature.

A measurement of $\mathcal{A}_\tau$ has also been performed using the normalised particle energy as polarisation sensitive variable. The fit result for the $\tau \to \pi\nu$ channel is [56, 58]:

$$\mathcal{A}_\tau = 0.163 \pm 0.034 \text{ (stat.)} \pm 0.028 \text{ (sys.)}$$

Since both measurements are based on the 1994 data sample they are statistically correlated. The larger sensitivity of the energy spectra to the τ polarisation is reflected by a smaller statistical error. In addition, events with selected pions in one hemisphere and 3-prong τ decays in the opposite hemisphere enter this analysis. But the systematic error using the acolinearity method is approximately two times smaller. In case of the energy method the uncertainty of the energy calibration ($\Delta\mathcal{A}_\tau^{cal.} = 0.26$) dominates the systematic error. This contribution alone is larger than the systematic error using the acolinearity method.

All LEP experiments have performed a measurement of the polarisation asymmetries. The results together with the LEP average are shown in table 7.3. The values for $\mathcal{A}_\tau$ and $\mathcal{A}_e$ are in good agreement, confirming the hypothesis of lepton universality in the neutral current.

Experiment	Year	$\mathcal{A}_\tau$	$\mathcal{A}_e$
ALEPH	(90 - 92), final	$0.136 \pm 0.012 \pm 0.009$	$0.129 \pm 0.016 \pm 0.005$
DELPHI	(90 - 94), prel.	$0.138 \pm 0.009 \pm 0.008$	$0.140 \pm 0.013 \pm 0.003$
L3	(90 - 94), prel.	$0.152 \pm 0.010 \pm 0.009$	$0.156 \pm 0.016 \pm 0.005$
OPAL	(90 - 94), final	$0.134 \pm 0.009 \pm 0.010$	$0.129 \pm 0.014 \pm 0.005$
LEP Average		0.1401 ± 0.0067	0.1382 ± 0.0076

Table 7.3: The combined LEP results for $\mathcal{A}_\tau$ and $\mathcal{A}_e$. The first error is statistical and the second systematic. In the LEP average, statistical and systematic errors are combined in quadrature [7].

Chapter 8

The Measurement of A_{TT} and A_{TN}

Within the coordinate system defined in chapter 5.2 the electron beam has preferred directions if spin correlations exist. The distribution in the azimuthal angle ω is not flat and is used to define the observables A_c and A_s which are proportional to C_2 and D_2. In order to determine the spin correlations a detailed understanding of detector acceptance and resolution effects is necessary. These effects are discussed in the first part of the following sections.

After the ω distribution is measured, the expected background contribution is subtracted and an efficiency correction applied. The observables A_c and A_s are calculated taking into account the radiative corrections. Finally the normalised spin correlations are obtained from the equations (5.22) and (5.23) for each final state independently. The numbers are averaged to obtain the final result.

The Reconstruction of the ρ Direction

In order to have maximal sensitivity to the spin correlations it is necessary to reconstruct the ρ direction. This can be seen from figure 8.1 where the ω distribution for the final state $\pi\rho$ is presented. The sensitivity to the transverse spin correlations is lost if the direction of the charged decay product is used instead of the ρ direction. The direction of the ρ is reconstructed from the measured angles and energies of the charged and neutral pion.

Before installation of the SMD the polar angles of the charged and neutral pions were reconstructed using the fill vertex position. The application of the SMD improves the reconstruction of the polar angles of charged particles and allows the determination of the track intercept with the beam axis event by event. The intercept defines a new reference point for the reconstruction of the π^0 polar angle. This improves the resolution of the π^0 - and ρ direction as shown in figure 8.2.

Figure 8.3 shows the $\Delta\phi$ versus the $\Delta\theta$ distribution.

$$\Delta\phi = \phi_{\pi^\pm} - \phi_{\pi^0}$$
$$\Delta\theta = \theta_{\pi^\pm} - \theta_{\pi^0}$$
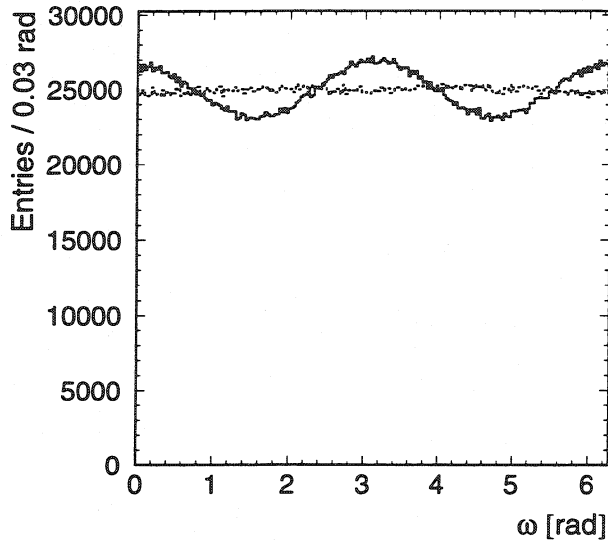
Figure 8.1: The KORALB Monte Carlo distribution for the final state $\pi\rho$. The sensitivity to the spin correlation is lost if the direction of the charged ρ decay product is used (dashed line) instead of the ρ direction itself (solid line).

The opening angle between the track and the neutral pion is approximately 50 mrad in θ and ϕ and well described by Monte Carlo.

The Determination of the Angle ω

The angle ω is calculated from the measured polar and azimuthal angles of the charged τ decay products (ϕ_1, θ_1) and (ϕ_2, θ_2).

$$\cos\omega = \frac{\cos\theta_2 - \cos\theta_1 \cos\theta_{12}}{\sin\theta_{12} \sin\theta_1} \qquad (8.1)$$

$$\cos\theta_{12} = \sin\theta_1 \sin\theta_2 \cos(\phi_1 - \phi_2) + \cos\theta_1 \cos\theta_2 \qquad (8.2)$$

Figure 8.4 shows the ω resolution. The distribution has non-Gaussian character. The root mean square is in the order of 1.6° if no π^0 occurs in the final state, 2.7° if one π^0 occurs and 5.4° if two π^0 are present in the final state. It has been found that the resolution is independent of ω.

For each event the generated and reconstructed sector number was computed. The sectors have been defined in figure 5.8. The fraction of events as a function of the generated and reconstructed sector number is shown figure 8.4. As a consequence of the good ω-resolution the number of events reconstructed in a wrong sector is at the 1 to 3% level. This varies with the number of reconstructed π^0's in the final state. From the diagonal elements it can be seen that the number of events which are assigned to a wrong sector nearly cancels.

The detector effects were studied using the KORALZ Monte Carlo. All results are confirmed by an independent sample generated with the KORALB generator.
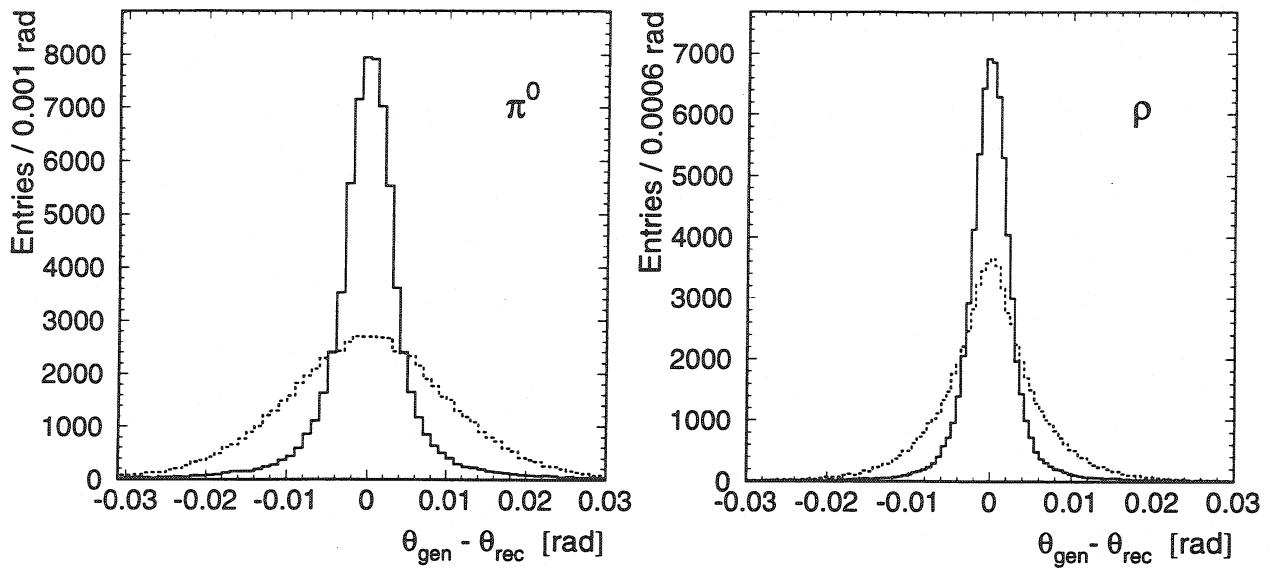
Figure 8.2: The polar angle resolution for the π^0 (left figure) and ρ (right figure). The method where the intercept is used as new reference point is illustrated by a solid line. The dashed line shows the resolution without the usage of the SMD intercept.
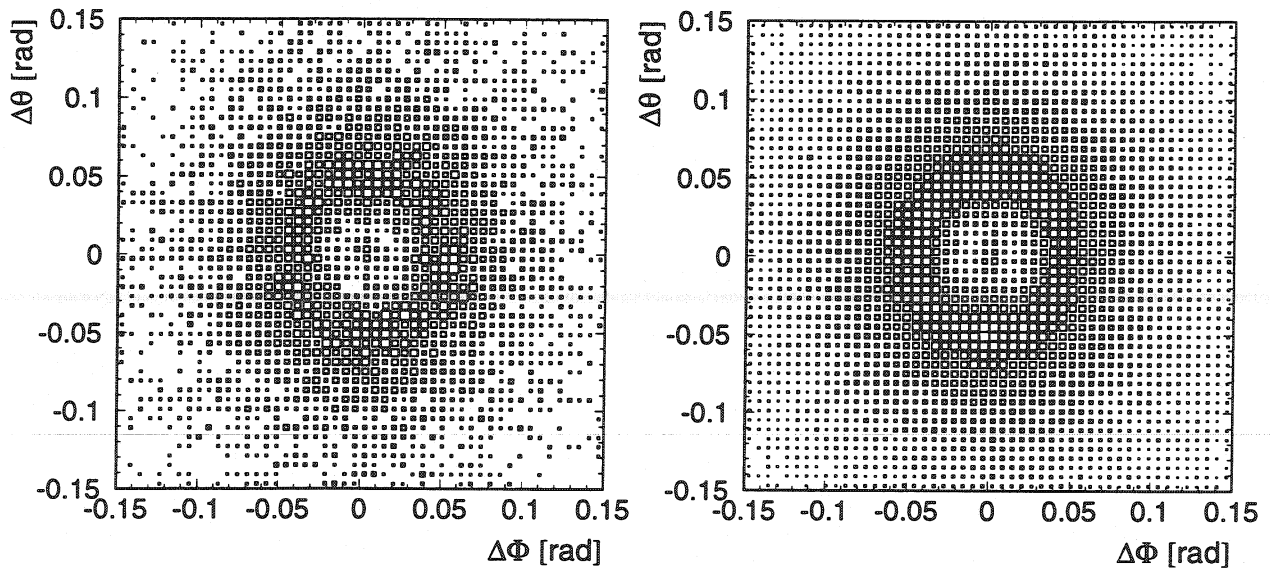
Figure 8.3: Comparison of the $\Delta\phi$ versus $\Delta\theta$ distributions for data(left) and Monte Carlo(right) for all selected $\tau \to \rho\nu$ decays.
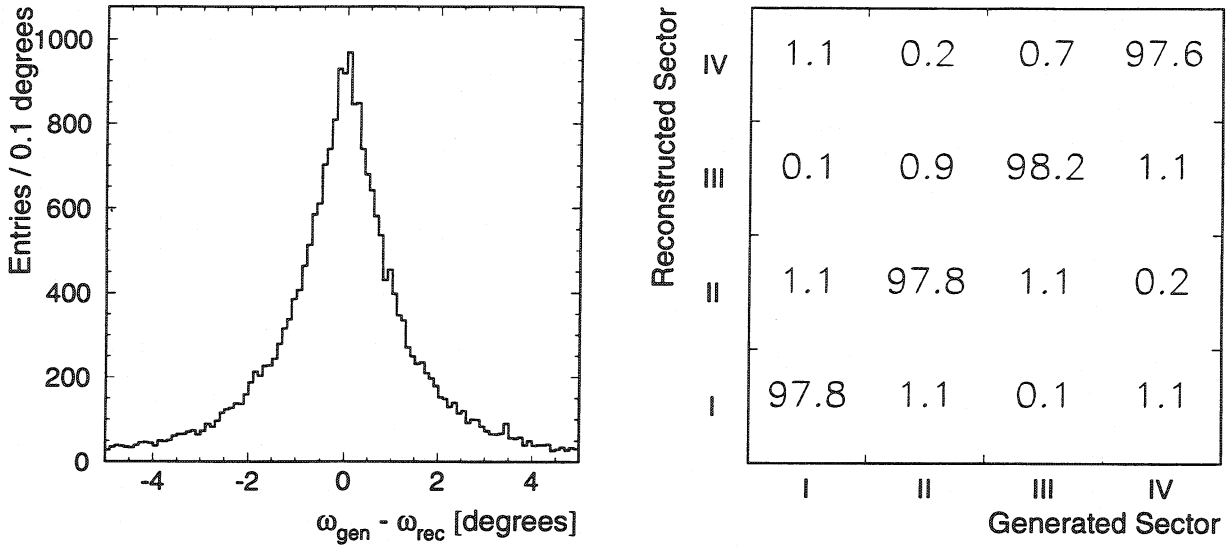
Figure 8.4: The left figure shows the ω_{gen}-ω_{rec} Monte Carlo distribution where no π^0 occurs in the final state. The root mean square of the distribution is 1.6°. The right figure represents the migration matrix for the same sample. A migration occurs if the generated sector number differs from the reconstructed sector number. The sectors are defined in figure 5.8. Approximately 98% of the events are reconstructed with the correct sector number.

The Selection Efficiency as a Function of ω

The selection efficiency is defined as the ratio of the number of selected events to the number of generated events. The efficiencies for the considered τ decay channels are shown in Appendix C. The values are given for the fiducial volume. The distributions were fitted by a straight line. The slope is consistent with zero for all distributions. SMD inefficiencies, gaps in the muon spectrometer and dead crystals in the BGO can introduce a non uniform efficiency in ω. Therefore a correction is applied bin by bin in the final analysis. The efficiencies were determined from the KORALZ Monte Carlo sample and confirmed using a KORALB Monte Carlo sample.

Check of the Analysis Method

The analysis procedure was checked with two independent Monte Carlo samples generated with KORALB and KORALZ respectively. The complete analysis chain was applied to the full detector simulated and reconstructed sample. The spin correlations A_{TN} are consistent with zero. The result for A_{TT} is one for the KORALB and zero for the KORALZ sample. These values are consistent with expectations from the implementation of the spin components in the generators. The results are shown in Appendix D.
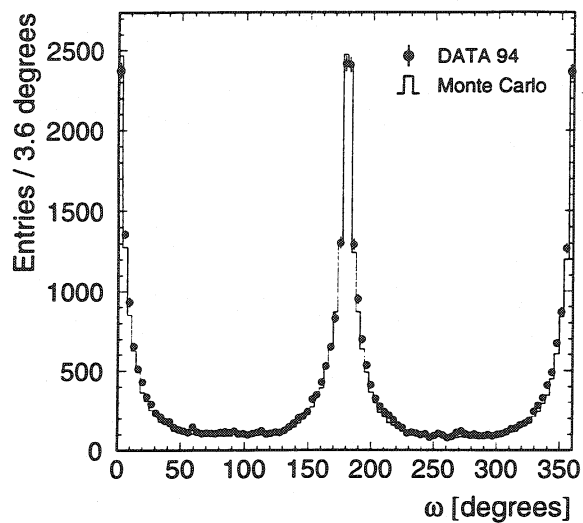
Figure 8.5: Comparison between data and Monte Carlo for $e^+e^- \to e^+e^-$ and $e^+e^- \to \mu^+\mu^-$ events.
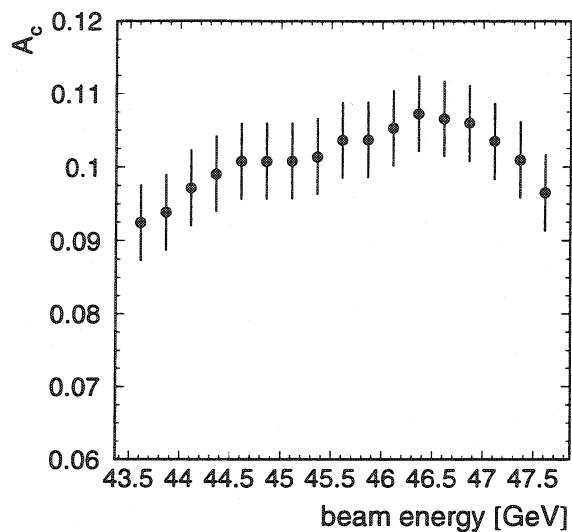
Figure 8.6: The energy dependence of A_c. Each point was calculated using $100\ 000\ \tau\tau \to \pi\pi\nu\nu$ events generated by the KORALB generator.
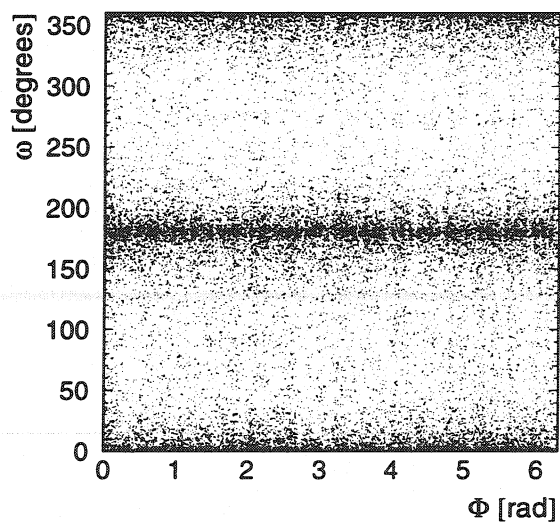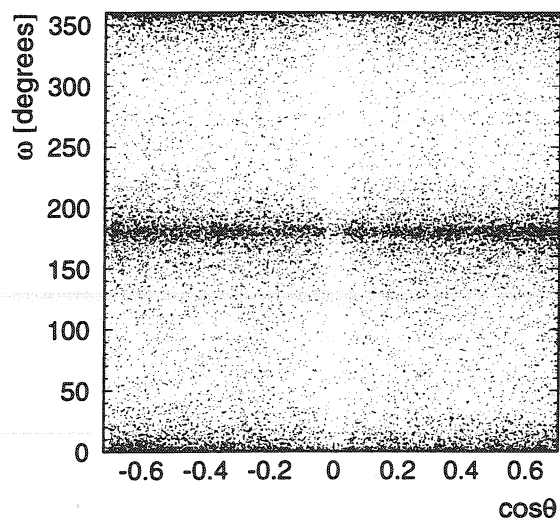
Figure 8.7: The angle ω as a function of $\cos\theta$ (left figure) and ϕ (right figure) for a selected $e^+e^- \to \mu^+\mu^-$ and $e^+e^- \to e^+e^-$ sample. The gap in the central $\cos\theta$ range corresponds to the central gap in the muon spectrometer.

In order to study systematic effects in the ω distributions $e^+e^- \rightarrow \mu^+\mu^-$ and $e^+e^- \rightarrow e^+e^-$ samples were selected The ω distributions are shown in figure 8.5. In the case of initial state radiation the centre of mass system is not at rest and a non-zero acolinearity angle is produced between the final state leptons. The tracks are almost back-to-back in the the r-ϕ plane. Since the electron beam lies within the plane defined by the two tracks the ω distribution peaks at $0/360°$ or $180°$. It can be seen that:

1. the widths of the peaks in data and Monte Carlo are in perfect agreement.

2. no offset between the data and Monte Carlo distribution is observed. This fact gives confidence in the alignment of the tracking system.

3. the peaks have the same height, because the photon radiation for electrons and positrons is identical.

The peak at $180°$ defines a sharp reference line which is used for further systematic studies. Figure 8.7 shows the ω distribution as a function of $\cos\theta$ and ϕ. No systematic deviation from the expected behaviour is found.

The energy dependence of the asymmetry A_c is shown in figure 8.6 for the final state $\pi\pi$ over a large energy range. Around the Z resonance the asymmetry is almost independent of the centre of mass energy. The data of this analysis has been collected on the Z resonance only.

8.1   Systematic Errors

The measurement of A_{TT} and A_{TN} relies on the knowledge of some numerical constants, e.g. the integrated $\hat{Q}_i$-functions and the understanding of the detector response. The following systematic errors have been considered. The values are summarised in table 8.1.

The τ polarisation uncertainty

Since only a certain acolinearity range was considered, the measurement of A_{TT} and A_{TN} depends on the τ polarisation. The value of the polarisation was varied within the errors. The systematic error is negligible.

The radiative corrections

The radiative corrections δA_c^{rad} and δA_s^{rad} were varied by 50%. The effect on A_{TN} is negligible.

The $\hat{Q}_i$-functions

The shape of the $\hat{Q}_i$-functions depends on the angular resolutions. In order to estimate the systematic error due to the angular resolution uncertainty the generated $\hat{Q}_i$-functions

Source	$\Delta\ A_{TT}$	$\Delta\ A_{TN}$
Radiative corrections	0.02	—
Q_i-functions	0.01	—
Selection efficiency	0.02	0.02
Sector reconstruction	0.04	0.03
τ background	—	0.01
Non-τ background	0.02	0.02
Selection	0.02	0.02
total	0.06	0.05

Table 8.1: Summary of systematic errors on A_{TT} and A_{TN}.

were used to calculate the spin correlations instead of the convoluted $\hat{Q}_i$-functions. The deviation of the mean value is given as systematic error.

The selection efficiency

The ω distribution was corrected for the selection efficiency bin by bin. In order to estimate the systematic error a flat efficiency distribution was assumed as suggested by the figures C.1 – C.2.

The non-τ background

The understanding of the non-τ background contribution is crucial, because it peaks at 0/360° and 180°. The non-τ background contribution was estimated for the hadron-lepton final states with the same procedure as described in section 7.1. For all other final states the Monte Carlo estimation was used. The background contribution was varied by 50%.

The τ background

The expected background contribution from misidentified other τ decays was subtracted from the selected data sample using the KORALB Monte Carlo sample. The uncertainty in the τ background contribution was investigated in two ways. First the total normalisation was changed by 2%. The effect on A_{TT} and A_{TN} is negligible. Second the background composition was changed. A variation of 10% was applied resulting in a modification of the background shape. The systematic effect was found to be small.
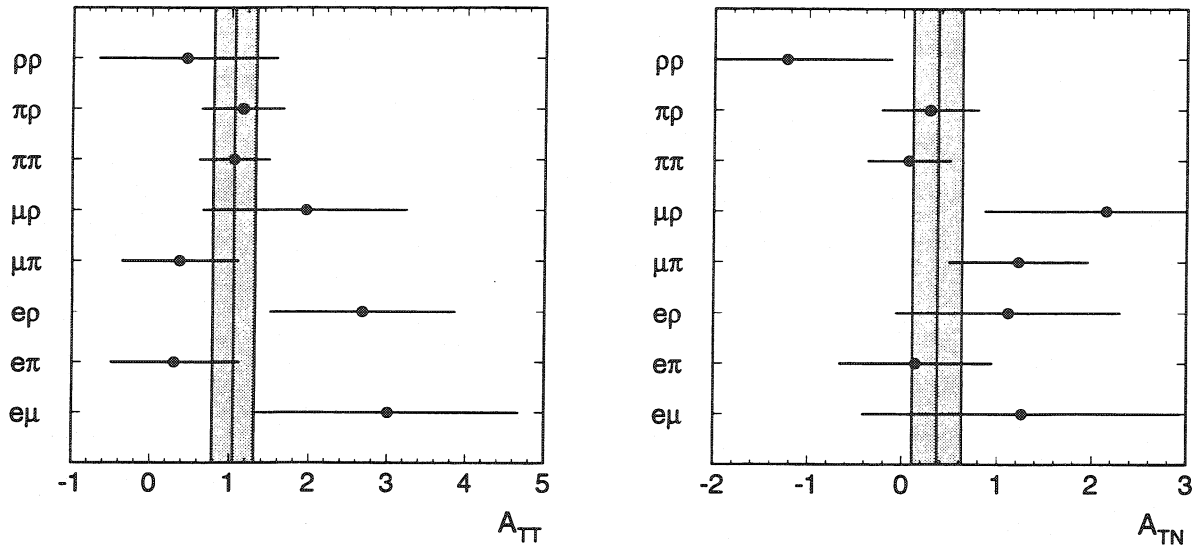
Figure 8.8: The fit results for A_{TT} and A_{TN}. The result for all individual channels are shown. The solid line represents the fit result. The statistical error is indicated by the shaded region. The χ^2/ndf of the fit is 5.8 / 7 for A_{TT} and 6.6 / 7 for A_{TN} respectively.

The event selection

The selection cuts were changed within reasonable limits. The systematic error contribution is shown in table 8.1.

The sector reconstruction

The reconstruction of the sectors to calculate A_c and A_s was investigated as shown by the migration matrix. A possible bias due to wrongly reconstructed sectors is at the 1 to 3% level. The number of events per sector was changed by 2% and added to the adjacent sector.

8.2 Results

Applying the procedure described above, a value for A_{TT} and A_{TN} is measured for each final state. The values together with the average over all final states are presented in figure 8.8. The average results of the normalised spin correlations are:

$$A_{TT} = 1.04 \pm 0.26 \text{ (stat.)} \pm 0.06 \text{ (sys.)} \tag{8.3}$$
$$A_{TN} = 0.36 \pm 0.26 \text{ (stat.)} \pm 0.05 \text{ (sys.)} \tag{8.4}$$
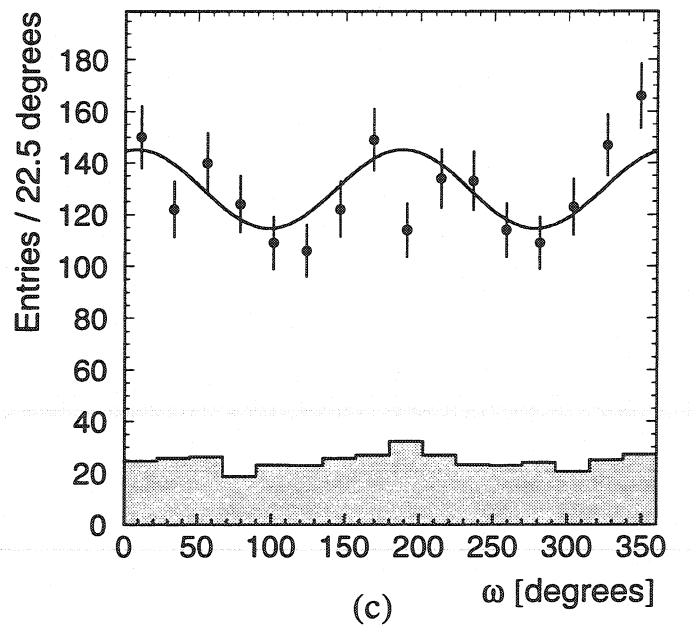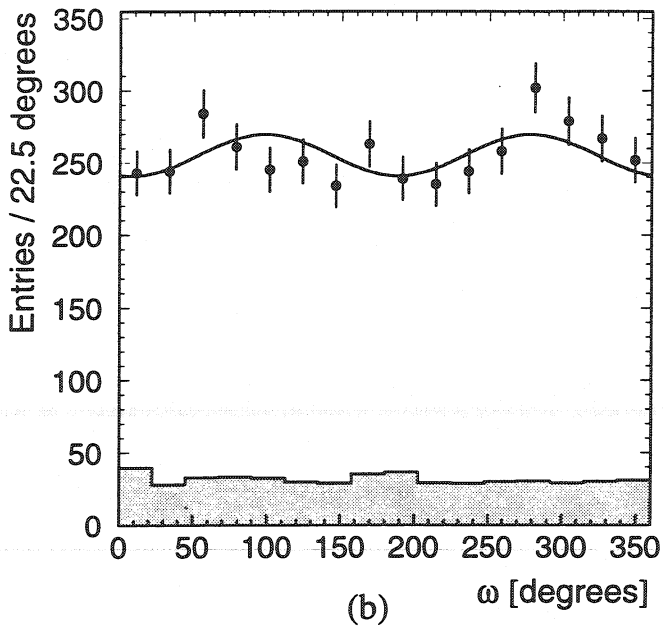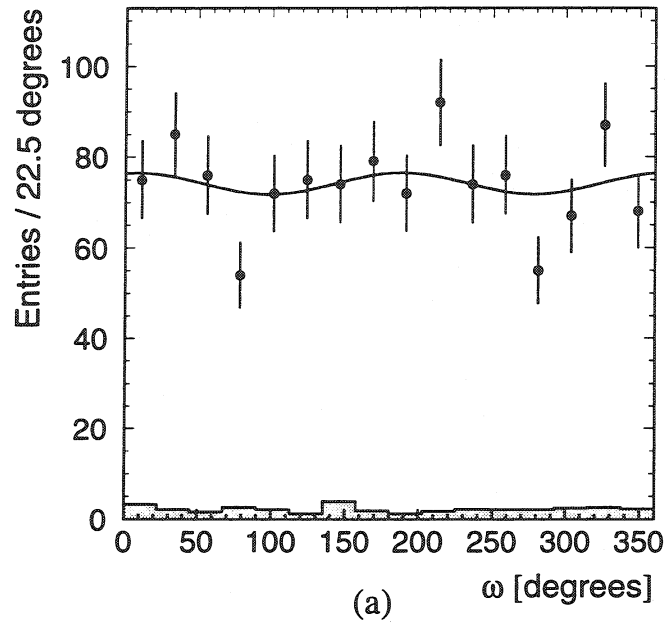
Figure 8.9: The ω distribution for the lepton-lepton (a), the lepton-hadron (b) and hadron-hadron (c) final states. The dots are data. The solid line represents the result of this analysis. The histograms are normalised to the total number of events. The total background contribution is shown in the shaded histogram.
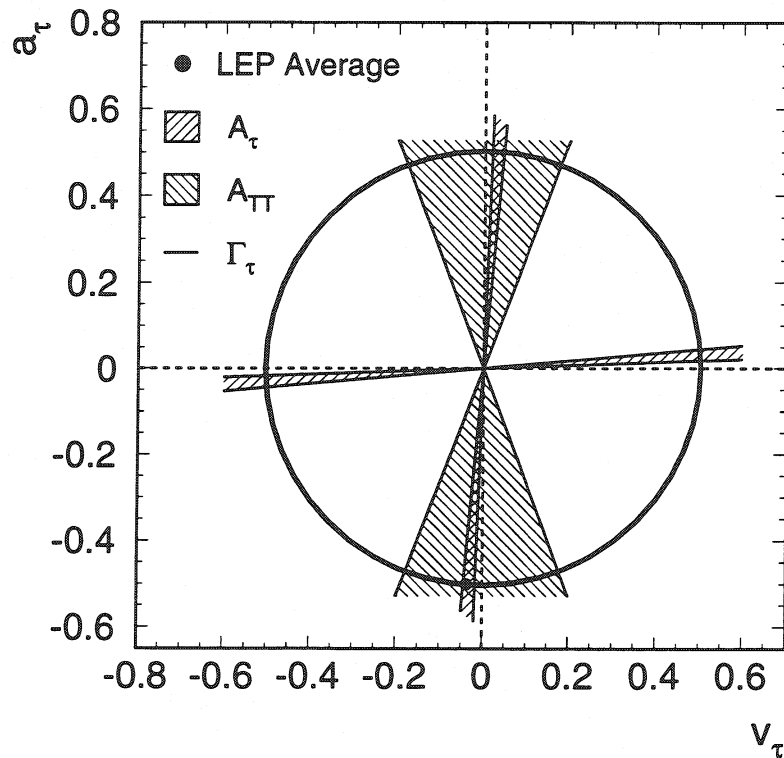
Figure 8.10: The hatched regions show the allowed values for a_τ and v_τ with 68% confidence level from this analysis. The measurement of the partial decay width of the Z into τ pairs (Γ_τ) is illustrated by the circle [61]. The error on Γ_τ is smaller than the line width of the circle. The dot represents the LEP average for a_τ and v_τ [7].

The spectra for the lepton-lepton, containing only the selected $e\mu$ sample, lepton-hadron and hadron-hadron final states are shown in figure 8.9. The superimposed function represents the result of this analysis. The shape of the distribution is described by the $\cos(2\omega)$ dependence as given in equation (5.11). From a comparison of the spectra it can be seen that the maxima are located at different positions (around 0/180/360° for the hadron-hadron and 90/270° for the lepton-hadron final state respectively). This behaviour is predicted by the Standard Model, because the polarisation analyser α_i has the opposite sign for purely leptonic and semileptonic τ decays. Since the selection efficiencies are flat and the measured angles are independent of the type of the particle, this behaviour provides a consistency check of the measurement.

The measurements of A_{TT} and A_{TN} are consistent with the Standard Model prediction. The transverse-transverse spin correlations A_{TT} differ by four sigma from zero. A_{TT} is the only on peak observable which is not symmetric in v_τ and a_τ. Interchanging v_τ and a_τ would lead to a Standard Model prediction of $A_{TT} = -0.99$ which is excluded

by approximately eight sigma. The relation between the weak mixing angle $\sin^2 \bar{\theta}_W$ and A_{TT} is discussed in Appendix E.

Figure 8.10 illustrates the polarisation and spin correlation measurements in the a_τ-v_τ-plane. The polarisation analysis shows that the couplings a_τ and v_τ must have equal signs. Nevertheless a fourfold ambiguity exists and the absolute values of the neutral current couplings are not constrained. The measurement of A_{TT} reduces the fourfold ambiguity, because the combinations with $|a_\tau| < |v_\tau|$ are excluded. Since measurements of asymmetries are not appropriate to determine the absolute values of the coupling constants a measurement of the partial decay width or the total cross section is necessary to constrain the magnitude of the couplings. The constraint from the partial decay width (Γ_τ) analysis is also shown in figure 8.10.

The observable A_{TN} can be used in combination with the τ polarisation measurement to determine the phase difference of the neutral current couplings. The measured value has to be corrected for the small γ-Z interference ($\Delta^{inf.} = 0.012$). Using $\mathcal{A}_{e-\tau}$ this analysis yields:

$$\tan(\Phi_{v_\tau} - \Phi_{a_\tau}) = -3.0 \pm 2.5 \tag{8.5}$$

$$\Phi_{v_\tau} - \Phi_{a_\tau} = -1.2 \, {}^{-0.2}_{+0.8} \quad \text{rad} \tag{8.6}$$

The result is consistent with the Standard Model prediction of $\tan(\Phi_{v_\tau} - \Phi_{a_\tau}) = -0.17$.

Chapter 9

Summary and Conclusions

Using a data sample collected by the L3 detector at LEP in 1994 corresponding to $50\ pb^{-1}$ of integrated luminosity, a full spin analysis of the process $e^+e^- \rightarrow \tau^+\tau^-$ has been performed. The sensitive variables for the polarisation and the spin correlation measurement have been computed from the measured azimuthal and polar angles of the τ decay products. The analysis exploits the precise information of the central tracking system based on the Silicon Microvertex Detector, which became fully operational in 1994.

The quantities $\mathcal{A}_\tau$, $\mathcal{A}_e$ and $\mathcal{A}_{e-\tau}$ which contain the neutral current couplings of the electron and the τ lepton have been determined using a sample of 4198 events with the final state πX where X can be any one prong τ decay product. The obtained values are:

$$
\begin{aligned}
\mathcal{A}_\tau &= 0.110 \pm 0.063\ (\text{stat.})\ \pm 0.015\ (\text{sys.}) \\
\mathcal{A}_e &= 0.149 \pm 0.095\ (\text{stat.})\ \pm 0.011\ (\text{sys.}) \\
\mathcal{A}_{e-\tau} &= 0.122 \pm 0.053\ (\text{stat.})\ \pm 0.010\ (\text{sys.})
\end{aligned}
$$

These results support the hypothesis of lepton universality in neutral current interactions. Assuming lepton universality the effective weak mixing angle is found to be:

$$
\sin^2 \bar{\theta}_W = 0.235 \pm 0.007
$$

where the systematic and statistical errors have been added in quadrature.

The effective weak mixing angle has been measured by several experiments. Some results are given in table 9.1. The values of the mixing angle given for $\mathcal{A}_\tau$ and $\mathcal{A}_e$ are calculated from the LEP average in table 7.3. The measurement of the forward-backard asymmetry for b-quarks (A^b_{fb}) provides a precise determination of the weak mixing angle. As can be seen the two most precise measurements differ by approximately three sigma. The result of this analysis is in good agreement with other determinations of the weak mixing angle.

Up to 1996 the existence of spin correlations in fermion pair production around the Z resonance was not established. Within this analysis the transverse-transverse and transverse-normal spin correlations have been investigated based on the following τ pair decay channels: $Z \rightarrow \tau\tau \rightarrow e\mu,\ e\pi,\ e\rho,\ \mu\pi,\ \mu\rho,\ \pi\pi,\ \pi\rho,\ \rho\rho$.
Using 7424 events the normalised spin correlations have been determined. The result

Asymmetry		$\sin^2 \bar{\theta}_W$
A_{fb}^b	(LEP)	0.23246 ± 0.00041
A_{LR}	(SLD)	0.23061 ± 0.00047
$\mathcal{A}_\tau$	(LEP)	0.23240 ± 0.00085
$\mathcal{A}_e$	(LEP)	0.23264 ± 0.00096

Table 9.1: Comparison of several determinations of the weak mixing angle from asymmetries [7].

$$A_{TT} = 1.04 \pm 0.26 \text{ (stat.)} \pm 0.06 \text{ (sys.)}$$

is in good agreement with the Standard Model prediction of $A_{TT} = 0.99$. This measurement establishes the existence of transverse-transverse spin correlations at the four sigma level. The measured spin correlation differs by eight sigma from -1., i.e. purely vector coupling. A_{TT} is the only on peak observable which is not symmetric in the vector and axial vector couplings. Therefore the measurement reduces the fourfold ambiguity in the a_τ-v_τ-plane as shown in figure 8.10. The positive value of A_{TT} indicates that the absolute value of the axial vector coupling of the $Z\tau\tau$ vertex is larger than the vector coupling. Traditionally this ambiguity was resolved analysing forward-backward asymmetries in the energy range around 40 GeV where the γ-Z interference introduce the dependence $A_{fb}(s \ll M_Z^2) \sim Q_e Q_f a_e a_f$ [62]. This analysis measures the dominance of the axial vector coupling from an on peak observable which is independent of QED effects. The effective weak mixing angle derived from the A_{TT} measurement

$$\sin^2 \bar{\theta}_W > 0.11 \quad \text{at 95\% C.L.}$$

is consistent with the value obtained from the τ polarisation measurement.

The observable A_{TN} carries information about the imaginary part of the coupling constants. The Standard Model prediction is zero at Born level and approximately 0.013 in the improved Born approximation. The result of this measurement is:

$$A_{TN} = 0.36 \pm 0.26 \text{ (stat.)} \pm 0.05 \text{ (sys.)}$$

The phase difference between the axial and vector coupling was deduced from the combination of the τ polarisation and the transverse-normal spin correlation measurement to

$$\tan(\Phi_{v_\tau} - \Phi_{a_\tau}) = -3.0 \pm 2.5$$
$$\Phi_{v_\tau} - \Phi_{a_\tau} = -1.2 \, {}^{-\,0.2}_{+\,0.8} \quad \text{rad}$$

which has to be compared with the prediction $\tan(\Phi_{v_\tau} - \Phi_{a_\tau}) = -0.17$. The precision needed to measure the small non-zero Standard Model or non Standard Model contributions will unfortunately never be reached at the LEP collider.
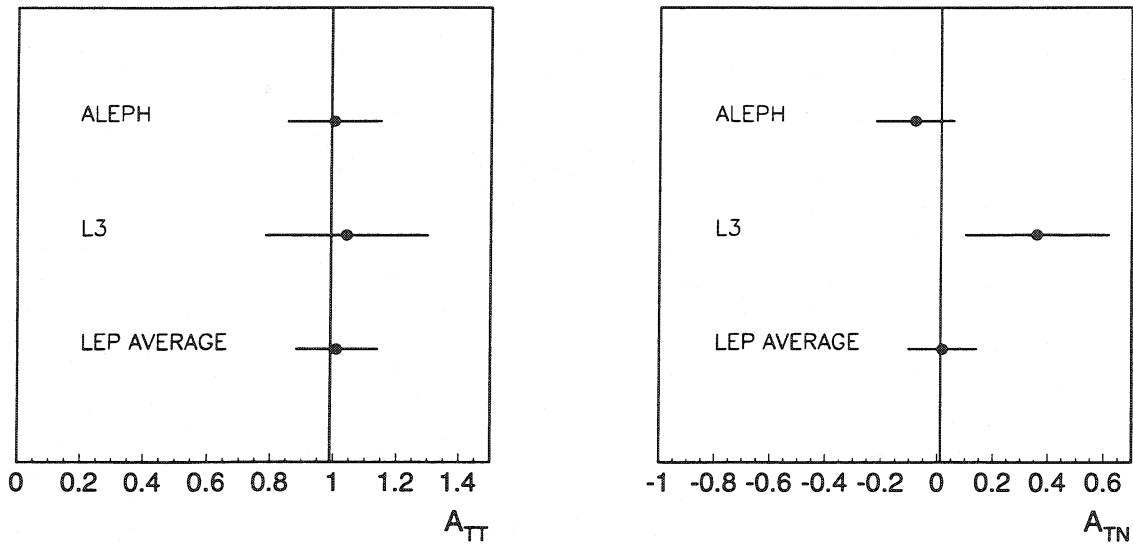
Figure 9.1: The combined LEP result for A_{TT} and A_{TN}. The statistical and systematic errors are added in quadrature. The Standard Model prediction is represented by a solid line. Both measurements are in agreement.

The spin correlation analysis provides an independent test of the coupling structure of the Standard Model. Experimentally this test can only be performed using $Z \rightarrow \tau\tau$ decays. Furthermore this analysis completes the measurement of observables related to the spin configuration in $Z \rightarrow \tau\tau$ processes.

The first preliminary evidence for transverse-transverse spin correlations was presented by the DELPHI collaboration [63]. The ALEPH collaboration has also reported on a preliminary measurement of A_{TT} and A_{TN} [64]. The combined results are shown in figure 9.1. The results are in agreement with each other and with the Standard Model predictions.

Within the experimental method presented here the inclusion of the one-prong $\tau \rightarrow a_1 \nu$ decay will not improve the results, because the sensitivity of this channel is suppressed by $\alpha \approx 0.12$. Furthermore it might be difficult to reconstruct the a_1 direction out of one charged track and two neutral pions. The final states $\tau\tau \rightarrow ee, \mu\mu$ are not very sensitive and contain large background fractions from $e^+e^- \rightarrow e^+e^-$, $e^+e^- \rightarrow \mu^+\mu^-$ and two photon processes. Therefore no improvement is expected. The analysis of the 1995 data sample will reduce the statistical error on A_{TT} and A_{TN} to approximately 0.22.

As known from the polarisation measurement the sensitivity loss (as described by α) can be recovered analysing the decay distributions of the ρ or a_1 decay. Unfortunately similar calculations don't exist for the spin correlation analysis. The introduction of an optimal variable in the spin correlation measurement could lead to a large improvement in the statistical error.

Appendix A

The Q_i–Functions

The Q_i-functions ($i = 1...4$) are kinematic functions depending on $x \equiv (\gamma \cdot \chi_1)^2$, where the dilation factor $\gamma = E/m_\tau$ controls the range of opening angle χ_1 of the decay product X_1^- with respect to the τ^-. Since the τ direction is not observable the Q_i-functions are defined by the following integrals.

$$Q_1(\epsilon) = \int dx \, \frac{1 + x + \gamma^2 \epsilon^2}{(1+x)^2 \cdot R^{3/2}} \tag{A.1}$$

$$Q_2(\epsilon) = \int dx \, \frac{1}{(1+x)^2 \cdot R^{3/2}} \cdot \left\{ \left(1 - \frac{2}{1+x}\right) H(\epsilon, x) \right\} \tag{A.2}$$

$$Q_3(\epsilon) = \int dx \, \frac{(1 + x + \gamma^2 \epsilon^2) \cdot (x - 1)}{(1+x)^3 \cdot R^{3/2}} \tag{A.3}$$

$$Q_4(\epsilon) = \int dx \, 12 \gamma^2 \epsilon^2 \, \frac{x \cdot (x - 1 - \gamma^2 \epsilon^2)}{(1+x)^3 \cdot R^{5/2}} \tag{A.4}$$

with:

$$R = x^2 + 2(1 - \gamma^2 \epsilon^2) x + (1 + \gamma^2 \epsilon^2)^2 \tag{A.5}$$

$$H(\epsilon, x) = \frac{2}{R}[(1 + x + \gamma^2 \epsilon^2)^2 + 2 \gamma^2 \epsilon^2 \, x] - (1 + x + \gamma^2 \epsilon^2) \tag{A.6}$$

The functions were calculated in the vanishing final mass approximation, i.e. the masses of the τ decay products are neglected with respect to the τ mass. If the masses are taken into consideration each Q_i-function becomes mass dependent leading to different Q_i-functions for different final states

$$Q_i(\epsilon) \quad \rightarrow \quad Q_i^{kl}(\epsilon) \tag{A.7}$$

where k, l labels the τ decay product e, μ, π, ρ.

Appendix B

The Mass Dependent Q_i – Functions

The masses of the τ decay products affect the shape of the Q_i-functions. The mass dependent functions have been computed from $2 \cdot 10^8$ generated τ pair decays using the TAUOLA program [45]. The parametrisation of the cross section as given in 5.8 can be rewritten in terms of mass dependent $\hat{Q}_i^{kl}$-functions, where the constant factors $\alpha_{k,l}$ are absorbed. The $\hat{Q}_i^{kl}$-functions used here are expressed in terms of Q_i-functions used in reference [12, 53] as:

$$
\begin{aligned}
\hat{Q}_1^{kl} &= Q_1 + \alpha_k \alpha_l Q_2 \\
\hat{Q}_2^{kl} &= (\alpha_k - \alpha_l) Q_3 \\
\hat{Q}_3^{kl} &= \alpha_k \alpha_l Q_4
\end{aligned}
$$

In order to investigate the influence of the finite detector resolution the $\hat{Q}_i$-functions were convoluted according to the resolution functions for the polar and azimuthal angles. The sign of $\hat{Q}_3(\epsilon)$ depends on the considered final state. The analytical and mass dependent Q_i-functions of the final state $\tau\tau \to \pi\pi$ are compared in figure B.1. The mass dependent functions are shown in figures B.2 - B.9.
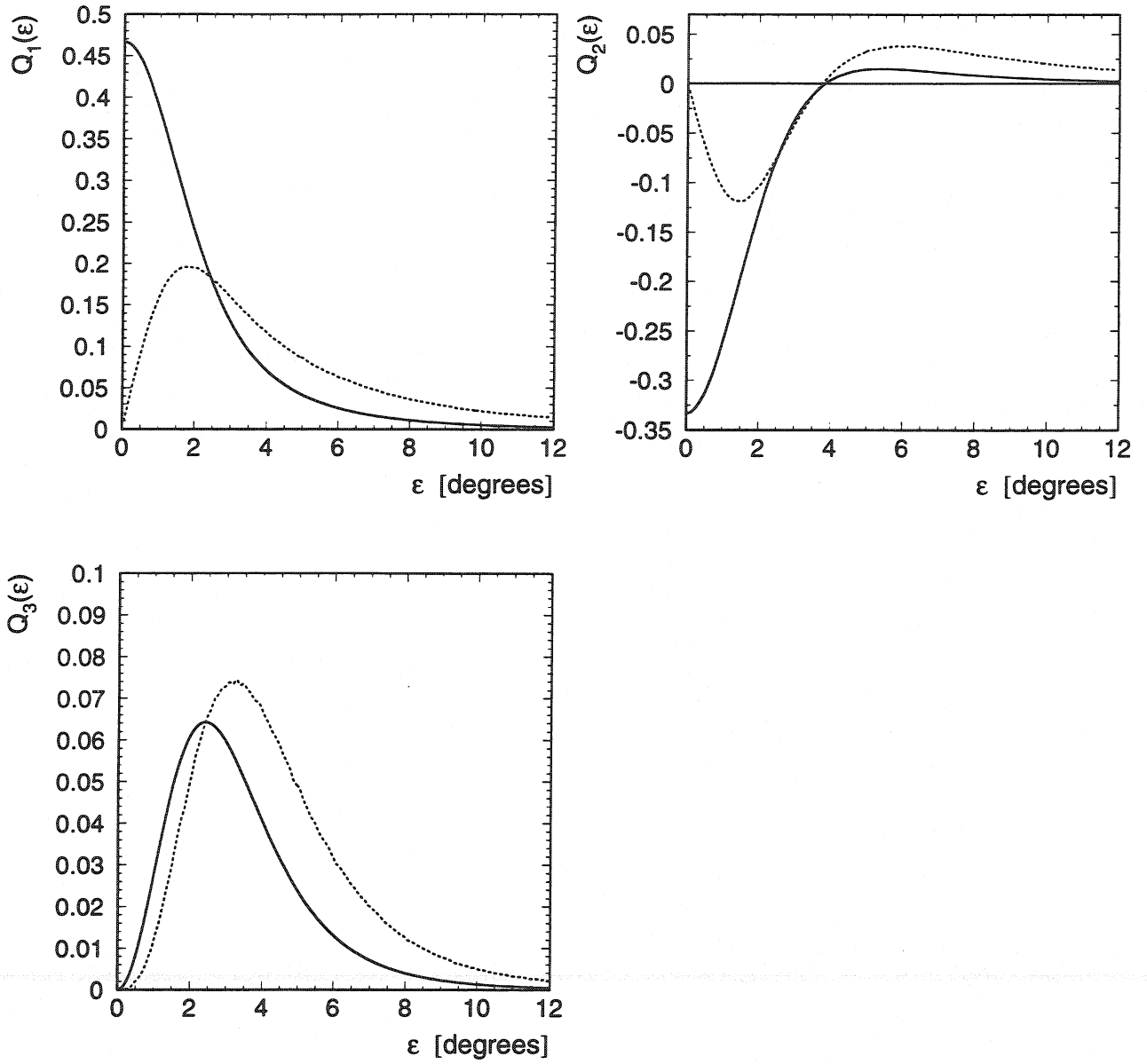
Figure B.1: The Q_i-functions for the final state $\tau\tau \to \pi\pi$ are shown. The solid line represents the analytical calculation in the vanishing mass approximation. The dashed line corresponds to the mass dependent functions.
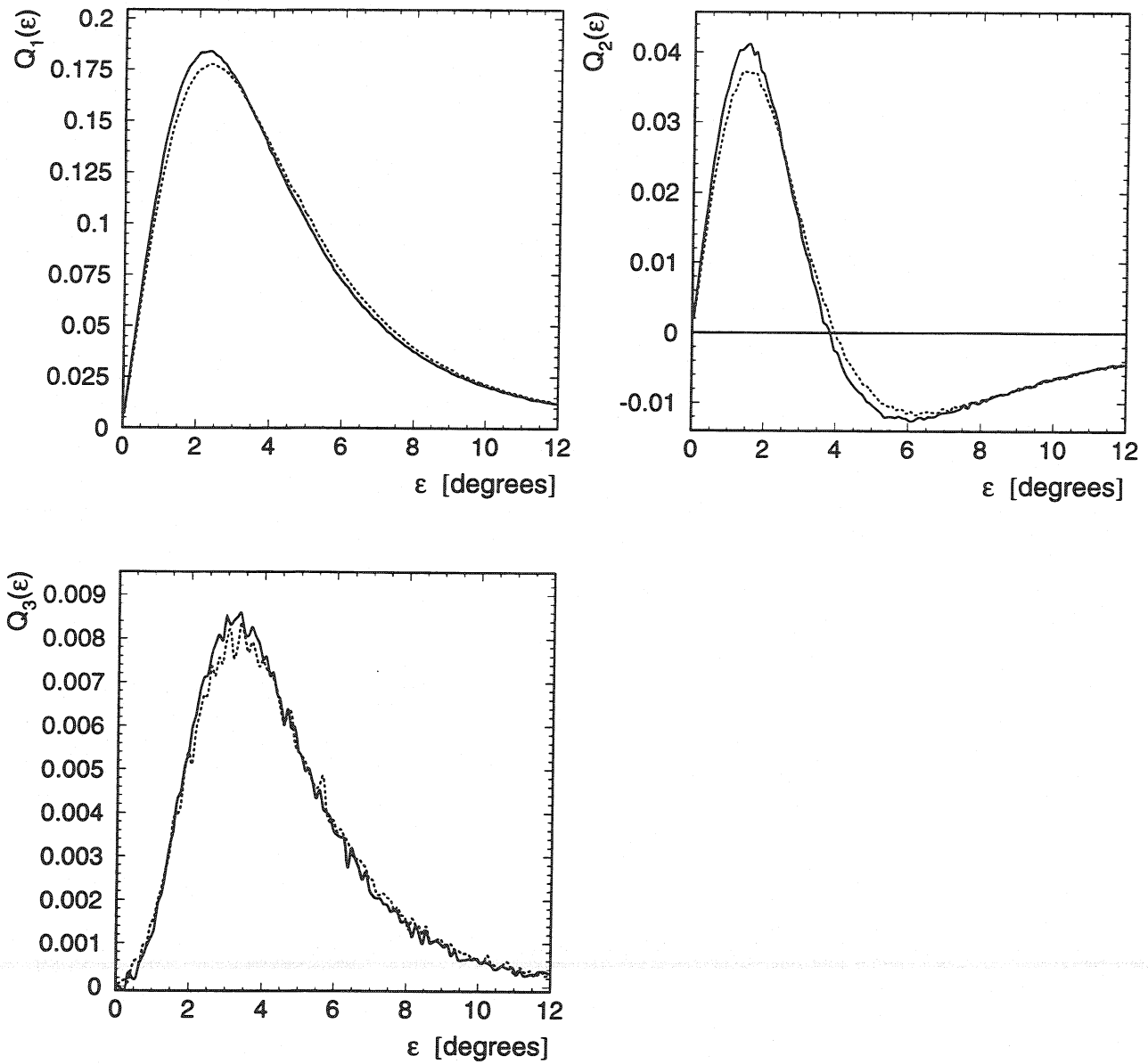
Figure B.2: The $\hat{Q}_i^{kl}$-functions for the final state $\tau\tau \to e\mu$. The dashed line includes the finite detector resolution.
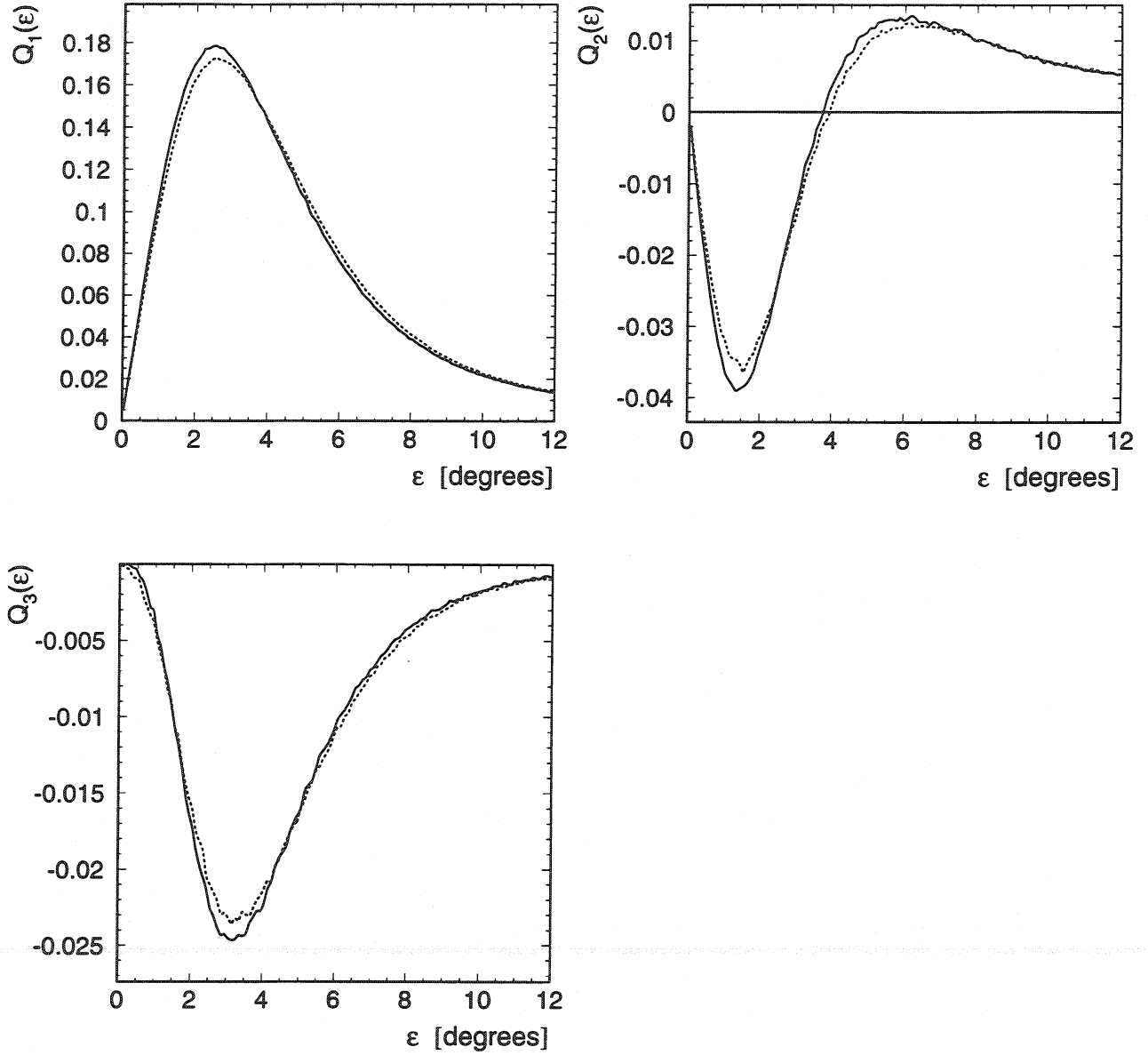
Figure B.3: The $\hat{Q}_i^{kl}$-functions for the final state $\tau\tau \to e\pi$. The dashed line includes the finite detector resolution.
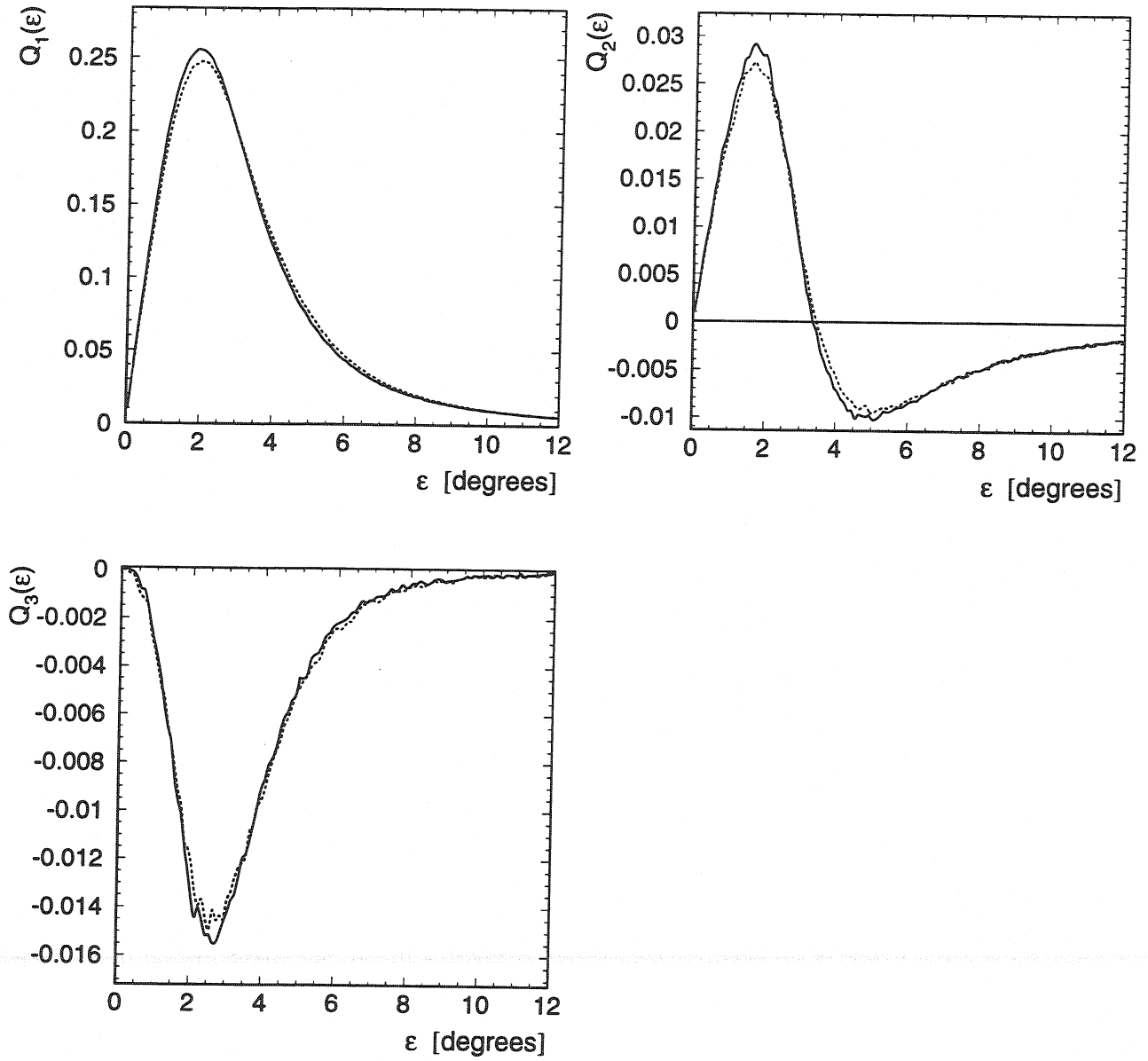
Figure B.4: The $\hat{Q}_i^{kl}$-functions for the final state $\tau\tau \to e\rho$. The dashed line includes the finite detector resolution.
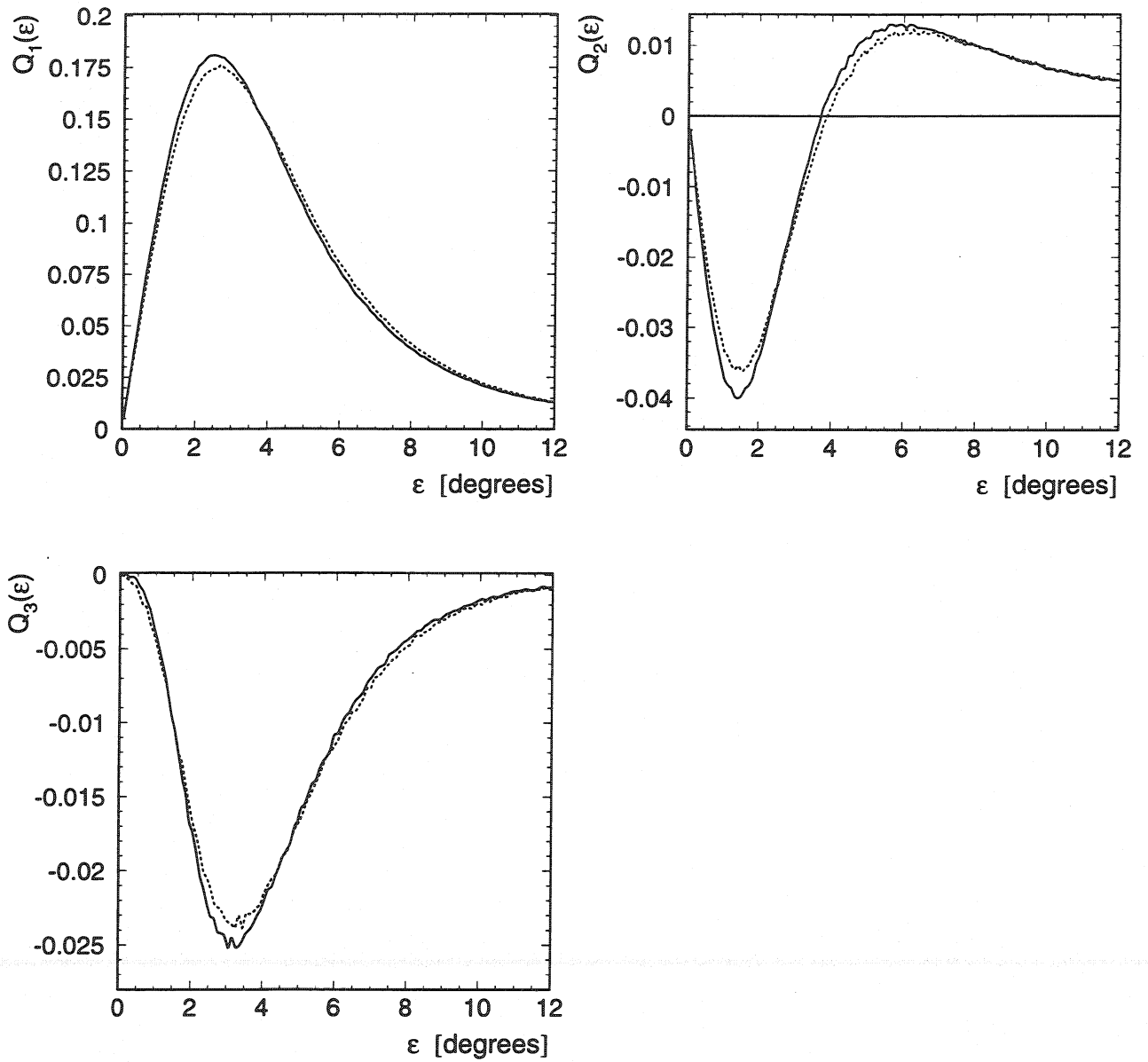
Figure B.5: The $\hat{Q}_i^{kl}$-functions for the final state $\tau\tau \to \mu\pi$. The dashed line includes the finite detector resolution.
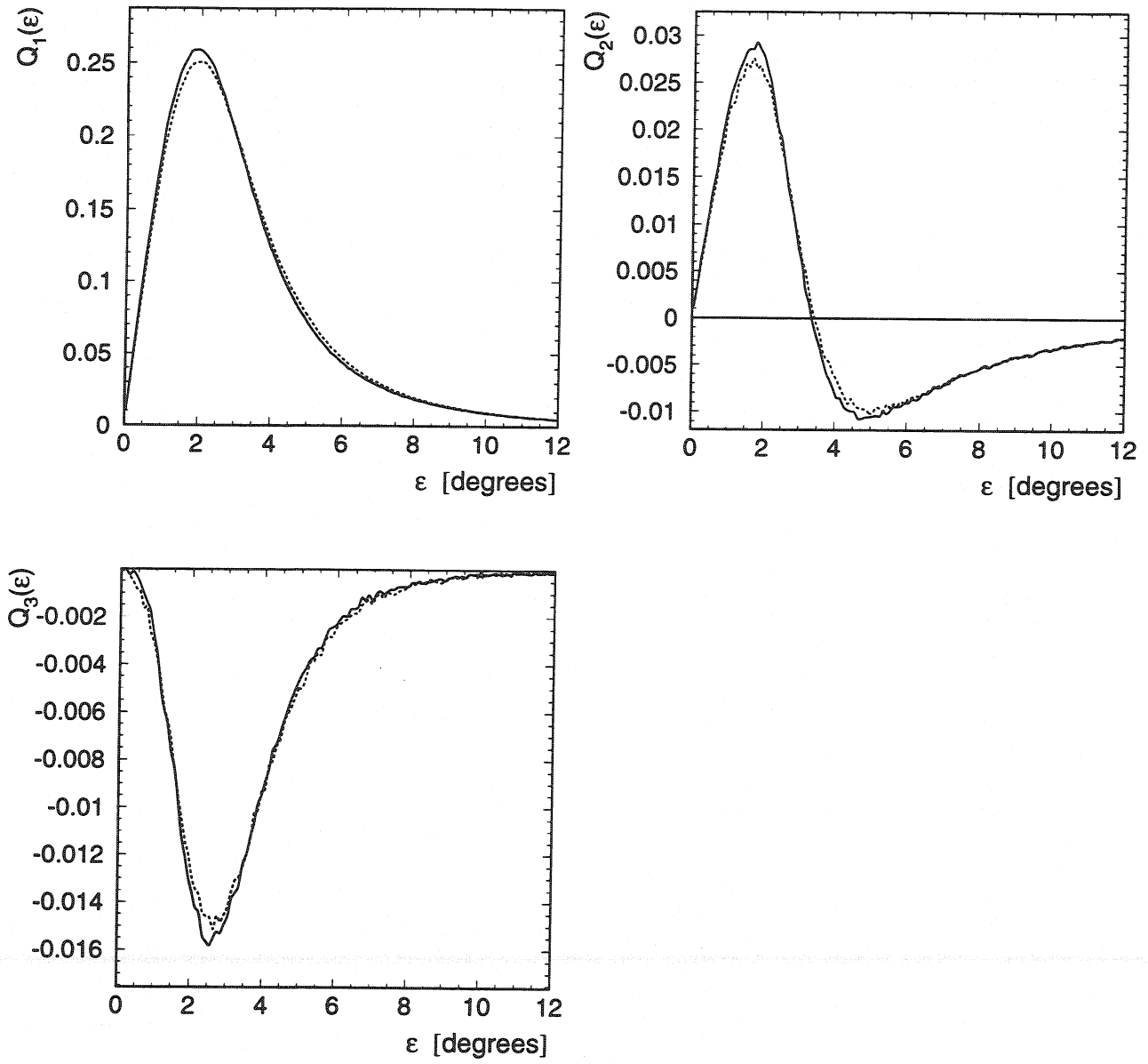
Figure B.6: The $\hat{Q}_i^{kl}$-functions for the final state $\tau\tau \to \mu\rho$. The dashed line includes the finite detector resolution.
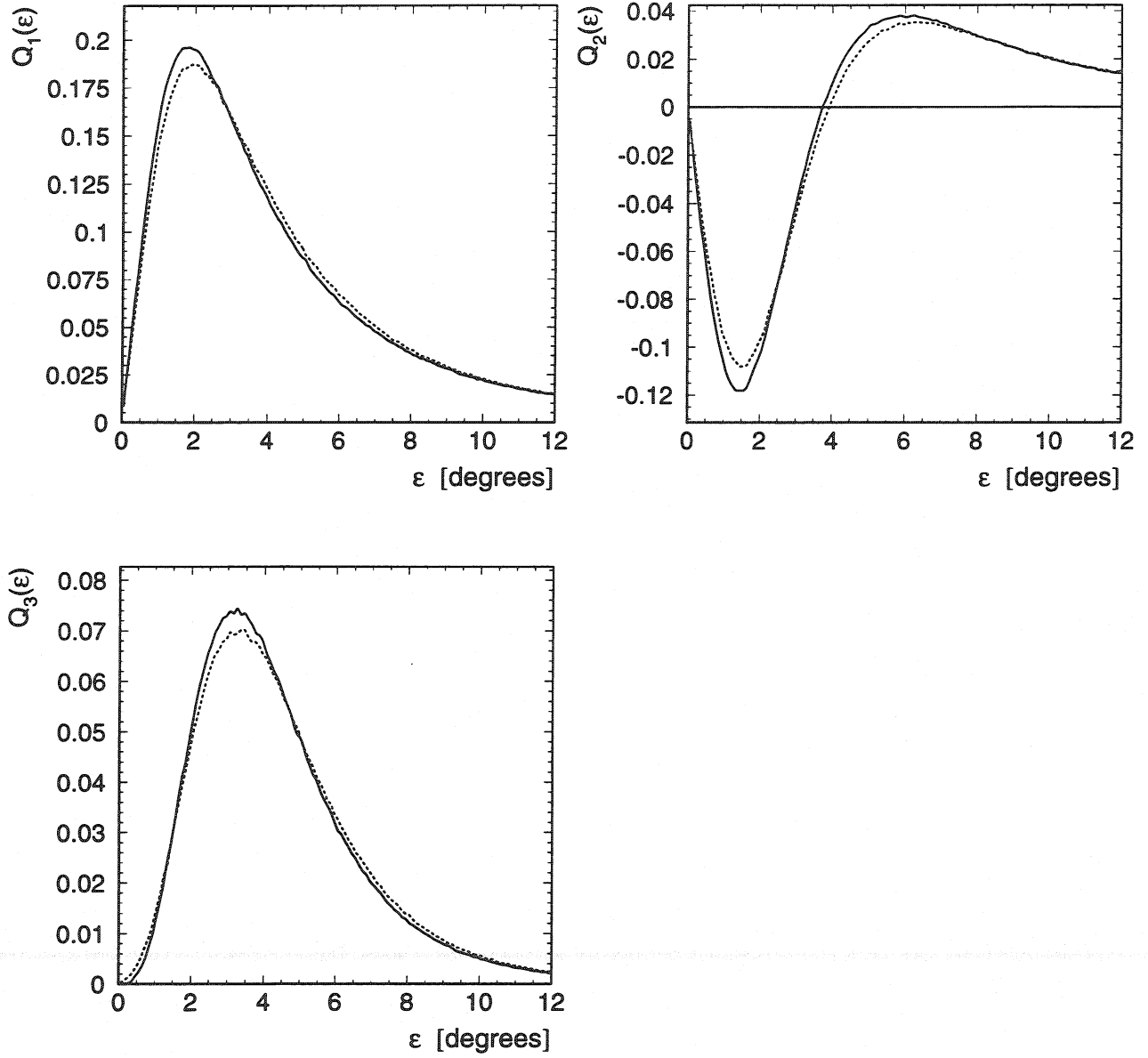
Figure B.7: The $\hat{Q}_i^{kl}$-functions for the final state $\tau\tau \to \pi\pi$. The dashed line includes the finite detector resolution.
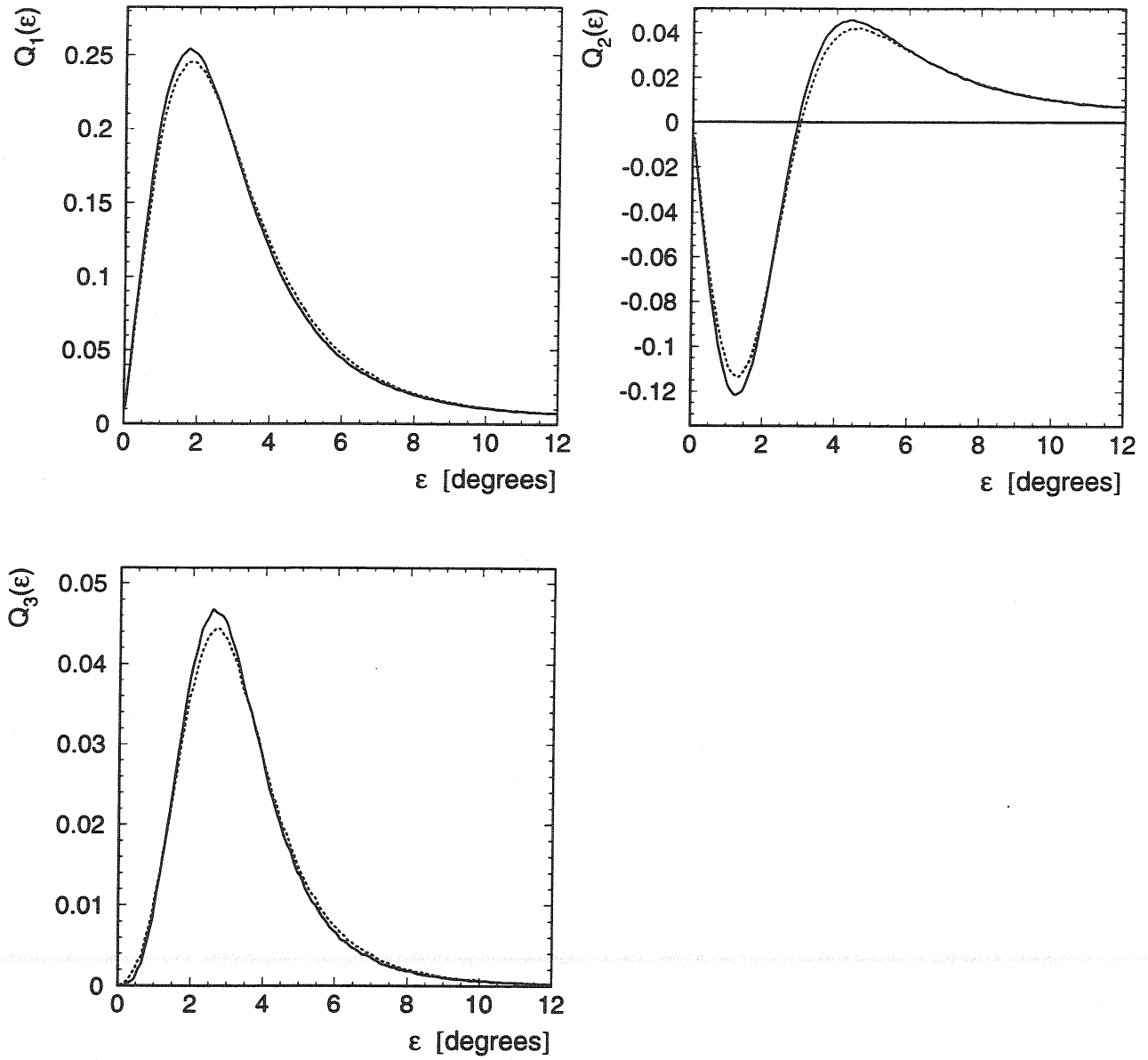
Figure B.8: The $\hat{Q}_i^{kl}$-functions for the final state $\tau\tau \to \pi\rho$. The dashed line includes the finite detector resolution.
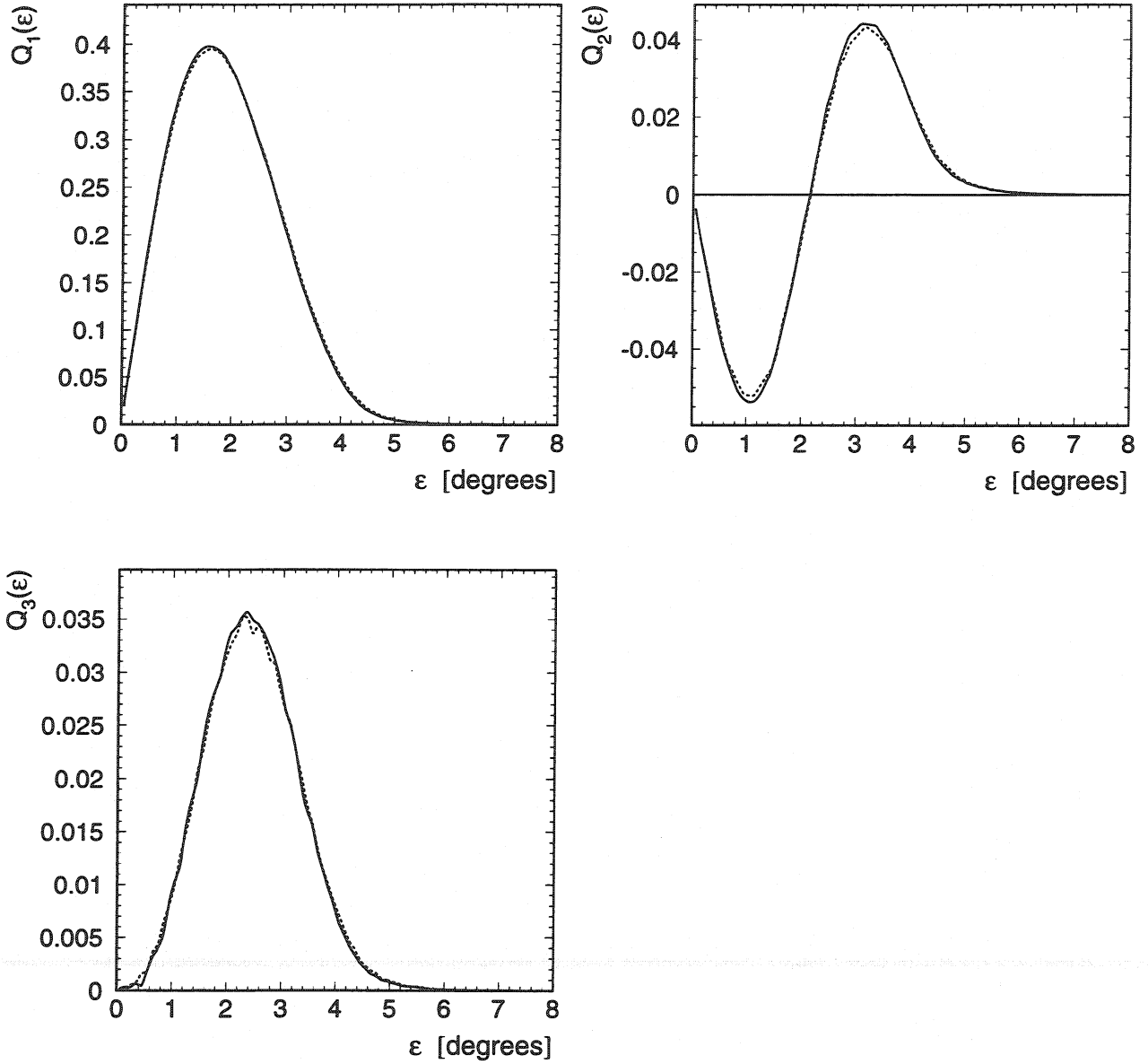
Figure B.9: The $\hat{Q}_i^{kl}$-functions for the final state $\tau\tau \rightarrow \rho\rho$. The dashed line includes the finite detector resolution.

Appendix C

The Selection Efficiencies

The selection efficiencies for the exclusive final states as a function of the angle ω are presented in the figures C.1 - C.2. The efficiencies are independent of ω as expected.
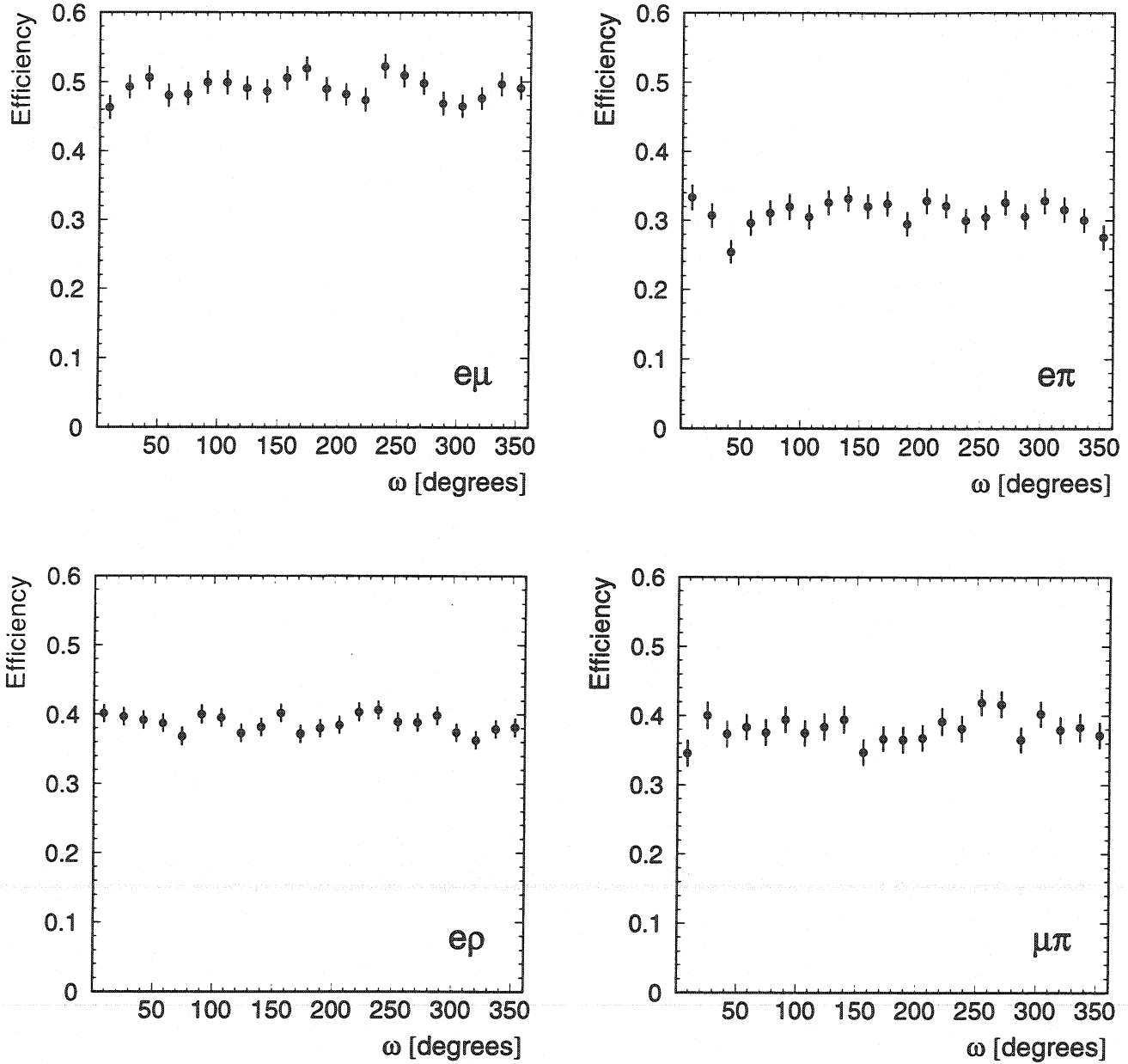
Figure C.1: The selection efficiency as a function of ω in the fiducial volume for different final states as indicated. The error corresponds to the limited Monte Carlo statistic.
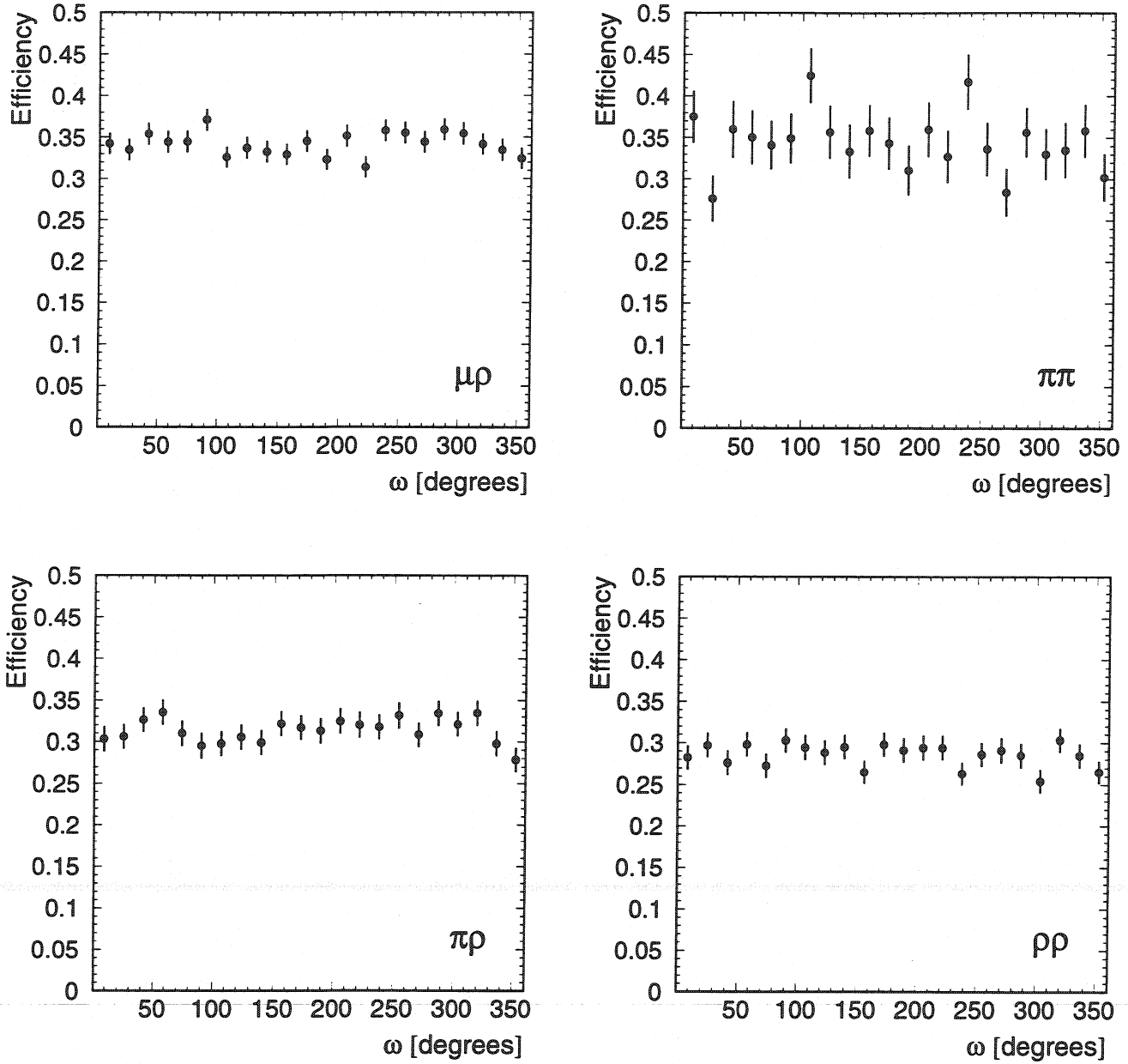
Figure C.2: The selection efficiency as a function of ω in the fiducial volume for different final states as indicated. The error corresponds to the limited Monte Carlo statistic.

Appendix D

Test of the Method

The experimental method to measure the spin correlations has been checked using two different Monte Carlo samples. The transverse and normal spin components are only implemented in the KORALB Monte Carlo. The results for the Monte Carlo samples are in agreement with the spin implementation as shown in figure D.1.
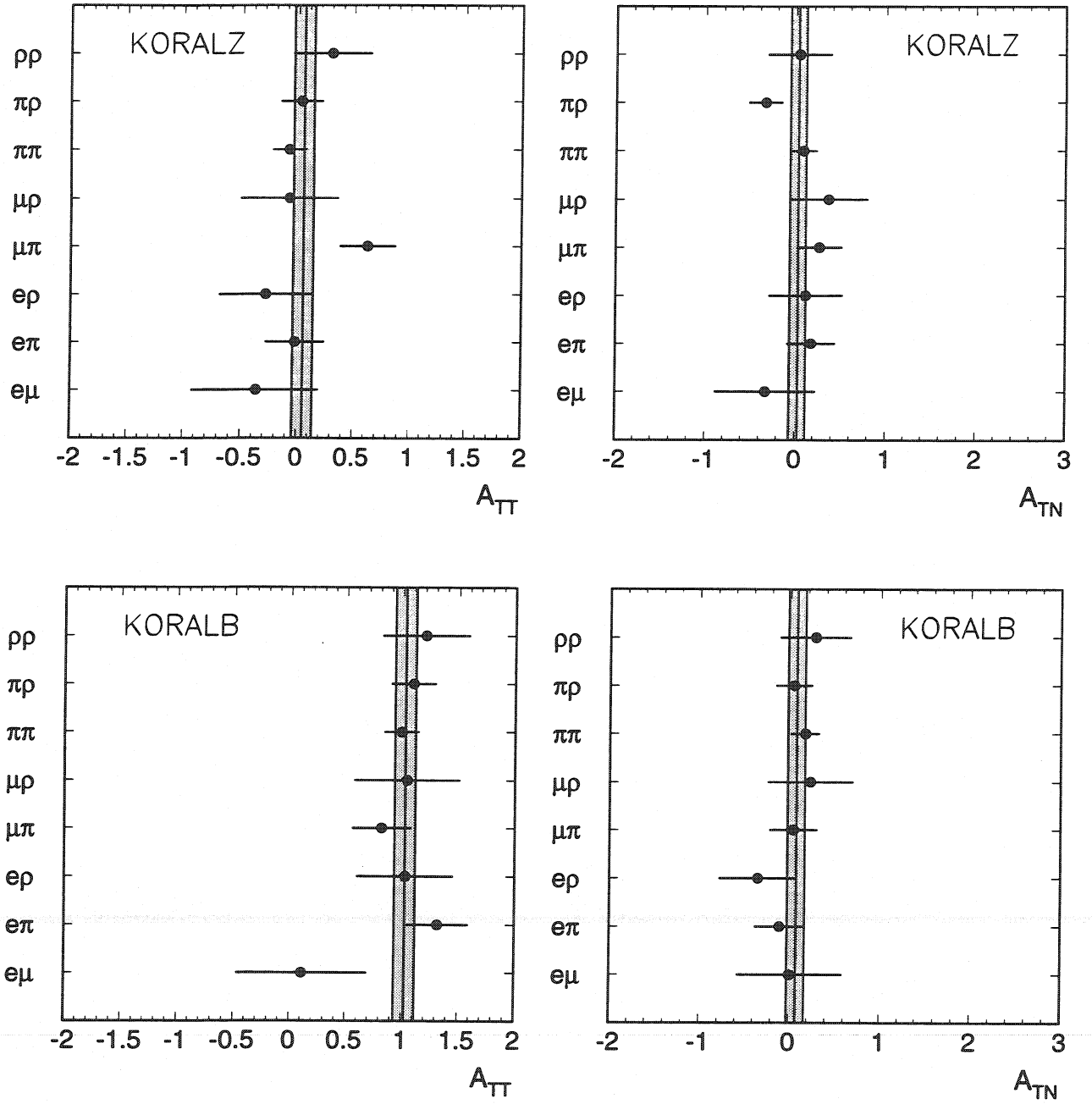
Figure D.1: The results for A_{TT} and A_{TN} obtained from a full detector simulated and reconstructed KORALZ and KORALB Monte Carlo sample. The result for each channel is shown. The solid line represents the fit result where the shaded area corresponds to the error of the fit.

Appendix E

The Weak Mixing Angle $\bar{\theta}_W$ and A_{TT}

The transverse-transverse spin correlations depend on the weak mixing angle:

$$A_{TT} = \frac{|a_\tau|^2 - |v_\tau|^2}{|a_\tau|^2 + |v_\tau|^2}$$

$$A_{TT} = \frac{T_3^2 - (T_3 + 2\sin^2\bar{\theta}_W)^2}{T_3^2 + (T_3 + 2\sin^2\bar{\theta}_W)^2} \tag{E.1}$$

Since the vector coupling enters in quadrature the sensitivity to measure the weak mixing angle is reduced and not competitive with values obtained from other measurements, e.g. τ polarisation. The sensitivity S to measure the weak mixing angle

$$\Delta \sin^2\bar{\theta}_W = S\,\Delta\mathcal{A}_\tau \tag{E.2}$$

$$\Delta \sin^2\bar{\theta}_W = S\,\Delta A_{TT} \tag{E.3}$$

is shown in figure E.1. The relation between $\sin^2\bar{\theta}_W$ and A_{TT} has a sign ambiguity and is given by:

$$\sin^2\bar{\theta}_W = \frac{1}{2}\left(\pm\left[T_3^2\,\frac{1 - A_{TT}}{1 + A_{TT}}\right]^{1/2} - T_3\right) \tag{E.4}$$

By definition $|A_{TT}|$ is less or equal 1. The result of this analysis is outside the boundary of the physical allowed region. Nevertheless a lower limit on $\sin^2\bar{\theta}_W$ can be inferred using Bayesian approach [23]. The limit is

$$\sin^2\bar{\theta}_W > 0.11 \quad \text{at 95\% C.L.} \tag{E.5}$$

which is in agreement with the precise measured world average [23]:

$$\sin^2\bar{\theta}_W = 0.2315 \pm 0.0004 \tag{E.6}$$
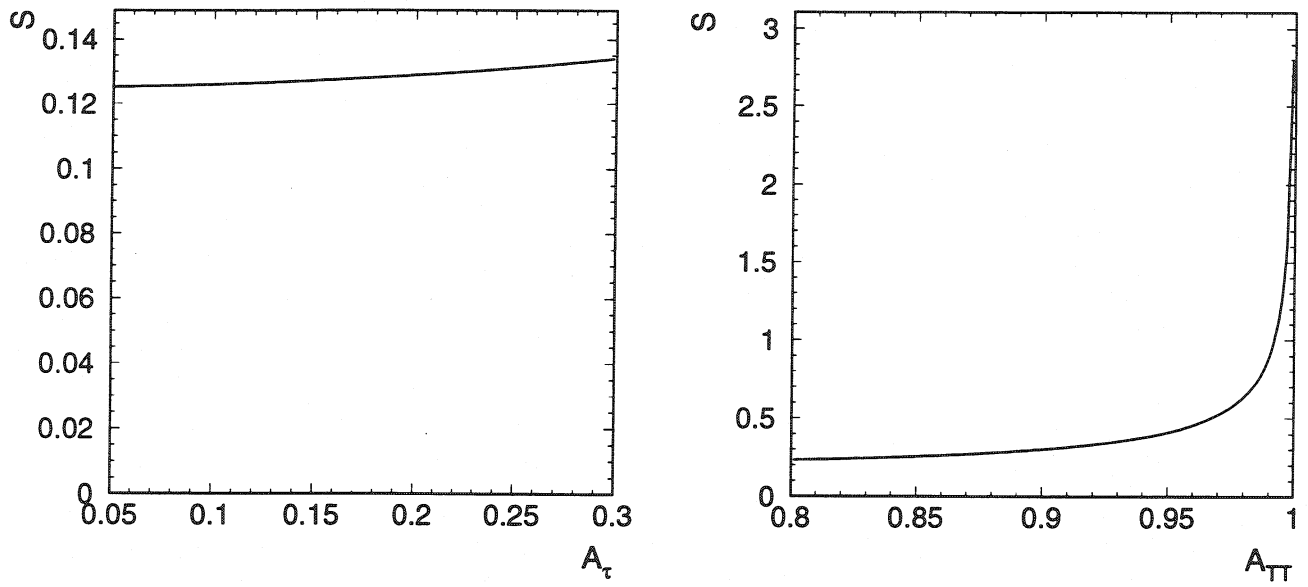
Figure E.1: Comparison between the sensitivities to measure the weak mixing angle from τ polarisation and spin correlations. The error for $\sin^2 \bar{\theta}_W$ is approximately eight times smaller than the error of the τ polarisation and polarisation independent (left figure). The sensitivity as a function of A_{TT} shows divergent behaviour for values close to one (right figure).

List of Figures

List of Tables

Bibliography

[1] J. Kepler, Mysterium Cosmographicum (1596), Das Weltgeheimnis, dt. v. M. Caspar, 1923

[2] S. Glashow, Nucl. Phys. **22** (1961) 579

[3] S. Weinberg, Phys. Rev. Lett. **19** (1967) 1264

[4] A. Salam, Elementary Particle Theory, Ed. N. Svartholm, Stockholm, Almquits and Wiksell (1968) 367

[5] P. Higgs, Phys. Lett. **12** (1964) 132
P. Higgs, Phys. Rev. Lett. **13** (1964) 508
P. Higgs, Phys. Rev. **145** (1966) 1156

[6] M. Kobayashi and T. Maskawa, Progr. Theor. Phys. **49** (1973) 562

[7] The LEP Collaborations ALEPH, DELPHI, L3, OPAL, the LEP Electroweak Working Group, CERN-PPE/96-183, Dec.6, 1996

[8] L. Passalacqua, Workshop on Tau Lepton Physics, Colorado, USA, September 16-19, 1996, proceedings to be published

[9] P. Mättig, "Searches for New Particles", Proc. 28 International Conference on High Energy Physics, Warsaw, 1996

[10] R. Alemany *et al.*, Nucl. Phys. **B379** (1992) 3

[11] S. Jadach and Z. Was, Z Physics at LEP, Vol. 1, CERN 89-08

[12] N. Rius, *Análisis de la polarización del tau y carrelaciones de espín a las energías de LEP*, PhD Thesis, University of Valencia (1991)

[13] Y.-S. Tsai, Phys. Rev. **D4** (1971) 2821
Errata Phys. Rev. **D13** (1976) 771

[14] S. Kirsch, DESY 93-157 (1993)

[15] N. Rius, Workshop on Tau Lepton Physics, Orsay, France, September 24-27, 1990, Ed. M. Davier, B. Jean-Marie, p. 313

[16] J. Bernabéu and N. Rius, Phys. Lett. **B232** (1989) 127

[17] F. del Aguila *et al.*, "Spin correlations at the Z-peak: a probe to the Z' mass", FTUV/91-39, UG-FT-19/91

[18] D. Bardin *et al.*, Z. Phys. **C44** (1989) 493

[19] M.L. Perl, Proceedings of the International Conference on the History of Original Ideas and Basic Discoveries in Particle Physics, Ettore Majorana Centre for Scientific Culture, Erice, Sicily July 29 – August 4, 1994

[20] M.L. Perl *et al.*, Phys. Rev. Lett. **35** (1975) 1489

[21] M.L. Perl, Proceedings of the International Neutrino Conference Aachen 1976, p.147

[22] BES Collaboration, J.Z. Bai *et al.*, Phys. Rev. **D53** (1996) 20

[23] Particle Data Group, R.M. Barnett *et al.*, Phys. Rev. **D54** (1996)

[24] N. Cabibbo, Phys. Rev. Lett. **10** (1963) 531

[25] E. Braaten, Phys. Rev. Lett. **60** (1988) 1606

[26] S. Narison, CERN-TH.7188/94 PM 94/08

[27] P. Kapinos, A Measurement of the Michel Parameter and ν_τ Helicity in τ-Lepton Decays with the L3 Detector at LEP, PhD Thesis, Humboldt University of Berlin (1996)
L3 Collaboration, M. Acciarri *et al.*, Phys. Lett. **B377** (1996) 313

[28] W. Lohmann, J. Raab, Charged Current Couplings in τ Decay, DESY 95-188 (1995)

[29] ARGUS Collaboration, H. Albrecht *et al.*, Phys. Lett. **B250** (1990) 164

[30] M. Grünewald, Physica Scripta, Vol **53** (1996) 257

[31] S. Gentile and M. Pohl, Phys. Rep. **274** (1996) 287

[32] LEP Design report vol. I, The LEP injector chain, CERN-LEP/TH/83-29 (1983)
LEP Design report vol. II, The LEP main ring, CERN-LEP/TH/84-01 (1984)

[33] L3 Collaboration, B. Abeva *et al.*, Nucl. Inst. Meth. **A289** (1990) 35

[34] J. Alcaraz, Heliciodal tracks, L3 Note 1666 (1995)

[35] M. Acciarri *et al.*, Nucl. Inst. Meth. **A351** (1994) 300

[36] A. Adam *et al.*, Nucl. Inst. Meth. **A344** (1994) 521

[37] H. Akbari *et al.*, Nucl. Inst. Meth. **A332** (1993) 33

[38] K. Deiters *et al.*, Nucl. Inst. Meth. **A323** (1992) 162

[39] E. Lieb and R. Völkert, Performance of the Z-Chamber during LEP Data Taking from 1992 to 1995, L3 Note 2028 (1996)

[40] L3 Collaboration, Phys. Rep. **236** (1993)

[41] I. Brock *et al.*, Nucl. Inst. Meth. **A381** (1996) 236

[42] R. Brun *et al.*, GEANT 3 Users Guide, CERN DD/EE84-1

[43] S. Jadach, Z. Was, Comput. Phys. Commun. **64** (1992) 267

[44] S. Jadach, B.F.L. Ward and Z. Was, Comp. Phys. Comm. **79** (1994) 503

[45] S. Jadach, R. Decker, J.H. Kühn and Z. Was, Comput. Phys. Commun. **76** (1993) 361

[46] S. Jadach, Z. Was, KORALB - An upgrade to version 2.4, CERN-TH-7272/94

[47] S. Kirsch, Neutral Current Physics with τ-Leptons using the L3 Detector at LEP, internal report, DESY-Zeuthen 94-04

[48] T. Hebbeker, W. Lohmann, "The Tau-W Coupling", HUB-EP-96/60, Nov.25, 1996

[49] A. Rougé, Z. Phys. **C48** (1990) 75

[50] K. Hagiwara, A.D. Martin, D. Zeppenfeld, Phys. Lett. **B235** (1990) 198

[51] M. Davier *et al.*, Phys. Lett. **B306** (1992) 411

[52] F. Sánchez, Z. Was, Phys. Lett. **B351** (1995) 562

[53] J. Bernabéu *et al.*, Phys. Lett. **B257** (1991) 219

[54] F. Sánchez, Phys. Lett. **B384** (1996) 277

[55] L3 Collaboration, M. Acciarri *et al.*, Phys. Lett. **B341** (1994) 245

[56] J. Gerald *et al.*, A Preliminary Measurement of $\mathcal{A}_\tau$ and $\mathcal{A}_e$ Using 1994 Data, L3 Note 1793 (1995)

[57] L. Jezequel, S.Karyotakis, L3 Note 1272 (1992)

[58] O. Adriani *et al.*, L3 Note 1637 (1994)

[59] F. James, "MINUIT Function minimization and error Analysis", CERN Program Library Long Writeup D506

[60] D. Bardin *et al.*, FORTRAN package ZFITTER; CERN-TH6443/92
     D. Bardin *et al.*, Z.Phys **C44** (1989) 493
     D. Bardin *et al.*, Nucl. Phys. **B351** (1991) 1
     D. Bardin *et al.*, Phys. Lett. **B255** (1991) 290

[61] L3 Collaboration, M. Acciarri *et al.*, Z. Phys. **C62** (1994) 551

[62] S.L. Wu *et al.*, Phys. Rep. **107** (1984) 59

[63] DELPHI Collaboration, "First Evidence of transverse spin correlations in Z^0 Decays", DELPHI 95-111 PHYS 546

[64] ALEPH Collaboration, "Measurement of the transverse spin correlations in the $\tau^+\tau^-$ production", contributed paper to Warsaw Conference, July 1996, PA07-075
     F. Sánchez, Workshop on Tau Lepton Physics, Colorado, USA, September 16-19, 1996, proceedings to be published

Acknowledgements